Novel Methods in Retinal Vessel Calibre Feature Extraction for Systemic Disease Assessment

A thesis submitted in fulfillment of the requirements for the degree of

Doctor of Philosophy

Behzad Aliahmad

M.Eng

School of Electrical and Computer Engineering
College of Science, Engineering and Health
RMIT University
March 2014

Declaration

I certify that except where due acknowledgements has been made, the work is that of the author alone; the work has not been submitted previously, in whole or in part, to qualify for any other academic award; the content of the thesis is the result of work which has been carried out since the official commencement date of the approved research program; and, any editorial work, paid or unpaid, conducted by a third party is acknowledged; and, ethics procedures and guidelines have been followed.

Behzad Aliahmad

Acknowledgements

There are many people, who have supported me by any means necessary throughout my research study that I would like to take this opportunity to thank them all.

My sincerest thanks and appreciation goes to my senior supervisor, Professor Dinesh K. Kumar for his constant professional support, encouragements and valuable comments. I was truly inspired by his ideas and guidance on how to pursue my research carrier.

I sincerely thank Dr. Ryo Kawasaki, Dr. Marc Sarossy for their strong ongoing technical supports, and all the staff team member of Center for Eye Research Australia (CERA) for providing materials and retina image databases.

I am grateful to all my friends and colleagues in the Biosignal Lab, Dr. Shridhar P. Arjunan, Mr. Hao Hao and Mr. Premith Unikrishnan, for their valuable helps and providing inspiring research environment. Also many special thanks to Mr. Hao Hao for providing me the chance to experiment with his own developed ECG-synchronized fundus camera.

My heartfelt thanks and deepest gratitude to my father Mr. M. Aliahmad, my mother Mrs. Z. A. Tehrani and my grandparents for their moral and financial supports. I was truly grateful for their unconditional love, understanding and encouragement

Finally, I would like to thank the staff member of the School of Electrical and Computer Engineering, RMIT University, Australia for their unsparing dedication and continuous support.

.

Abstract

Retina and its vascular network have unique branching characteristics morphology of which will change as a result of some systemic diseases, including hypertension, stroke and diabetes. Therefore, retinal image has been used as non-invasive screening window for risk assessment and prediction of such disease condition especially at the baseline. The assessment is based on a number of features among which vessel diameter (both individual and summary) and fractal dimension (FD) are the ones mostly associated with diabetes and risk of stroke. The association is linked to the higher risk of diabetes and stroke in people with narrower retinal arteriole diameter or change in overall fractal dimension independent of any risk factor (i.e. blood pressure, cardiovascular risk factors and …).

Diameter measurement requires vessel edges to be located and tracked however; accurate edge perception is subject to image contrast, shadows, lighting condition and even presence of retinopathy legions close to vessel boundaries. This will lead to imprecision and inconsistencies between different automatic measurement techniques and may affect the significance of its association with disease condition in risk-assessment studies. As accuracy and success of diameter measurement is subject to large variations due to image artifacts it may not be suitable for fully automatic applications. In order to compensate for such error, at first two novel automatic vessel diameter measurement techniques were proposed and validated which were more robust in the presence of such image artifacts compared to similar methods. However, sometimes the exact edge location and actual diameter value is not of interest. In most case-control studies, it is of importance to comparatively evaluate the variations in retinal vessel diameter as a sign of retinopathy such as arteriolar nicking as an example of hypertensive retinopathy. Vessel diameter is often required to be compared with a reference value in many analytical assessments for diagnostic purpose. This includes monitoring the diameter variations of a specific vessel segment within single subject overtime or across multiple subjects. This helps ophthalmologists to understand whether it has undergone any significant change and perhaps associate it with a disease abnormality. A technique that can effectively quantify that change without being impaired by image artifacts is of more importance and one of the rationales

of this study. This research hypothesized an edge independent solution for quantifying diameter variations when the actual diameter value is not required and proposed a new feature based on fractal analysis of vessel cross-section profile as a time series signal. This feature provides a link between FD as a global measure of the complexity and diameter variation as local property of a specific vessel segment. The validity of this work has been confirmed on i) synthetic vessels with known diameter ii) an expert annotated retinal image set and also iii) the images synchronized with Electrocardiogram (ECG). The clinical application of this feature has been validated on two population studies which showed promising result for assessment of mild non-proliferative diabetic retinopathy and 10-year stroke. The advantage of this new feature is that it is highly correlated to vessel diameter variations without requiring edge localization or image segmentation, ability for region based analysis and suitable for automatic assessment in the clinical settings.

This research work has also investigated whether the FD of retinal microvasculature would be affected by cyclic pulsations of retinal vessels and whether ECG synchronization is required prior to taking fundus images to compensate for this potential source of variations. To investigate, a new technique has been developed for automatic visualization and quantification of vessel pulsations and validated on a number of ECG synchronized fundus images.

Publications Arising From This Thesis

Fully Refereed International Journals

Published:

1. Kumar, D. K., **B. Aliahmad**, et al. (2012). "Retinal Vessel Diameter Measurement Using Unsupervised Linear Discriminant Analysis." ISRN Ophthalmology **2012**: 7.

2. Kumar, D. K., **B. Aliahmad**, et al. (2013). "A Method for Visualization of Fine Retinal Vascular Pulsation Using Nonmydriatic Fundus Camera Synchronized with Electrocardiogram." ISRN Ophthalmology **2013**: 9.

3. Hao, H., M. B., Sasongko, T. Y., Wong, M. Z., Che Azemin, **B. Aliahmad**, et al. (2012). "Does Retinal Vascular Geometry Vary with Cardiac Cycle?" Investigative Ophthalmology & Visual Science.

Internationally Refereed Conference Proceedings

1. **Aliahmad, B**., D. K. Kumar, et al. (2011). "Automatic retinal vessel profiling using multi-step regression method." Conf Proc IEEE Eng Med Biol Soc **2011**: 2606-2609.

2. **Aliahmad, B.**, D. K. Kumar, et al. (2012). Retinal vessel diameter measurement using multi-step regression method. Biosignals and Biorobotics Conference (BRC), 2012 ISSNIP.

3. **Aliahmad, B.,** D. K. Kumar, et al. (2013). Does fractal properties of retinal vasculature vary with cardiac cycle? Biosignals and Biorobotics Conference (BRC), 2013 ISSNIP.

4. Che Azemin, M. Z., D. K. Kumar, **B., Aliahmad**, (2012). Loss of calibre information during vessel segmentation. Biomedical Engineering and Sciences (IECBES), 2012 IEEE EMBS Conference on.

5. Hao, H., D. K. Kumar, **B., Aliahmad** (2013). "Measure the change of vessel edges across time series retinal images." AIP Conference Proceedings **1559**(1): 80-89.

6. Hao, H., D. K. Kumar, **B., Aliahmad**. (2011). Improved retinal photography method and visualization of multiple retinal images. Computer Applications and Industrial Electronics (ICCAIE), 2011 IEEE International Conference on.

7. Hao, H., D. K. Kumar, **B., Aliahmad**. (2013). Mathematical verification of summary formula in retinal vessel diameter measurement. Biosignals and Biorobotics Conference (BRC), 2013 ISSNIP.

8. Hao, H., D. K. Kumar, **B., Aliahmad**. (2013). Using color histogram as the trait of retina biometric. Biosignals and Biorobotics Conference (BRC), 2013 ISSNIP.

9. Hao, H., D. K. Kumar, M. Z. C., Azemin, **B., Aliahmad**. (2011). The measurement of multiple retinal images. Medical Measurements and Applications Proceedings (MeMeA), 2011 IEEE International Workshop on.

10. Hao, H., D. K. Kumar,R. Kawasaki, M. Z. C., Azemin, **B., Aliahmad** (2012). Normal distribution of cardiac variation in retinal image measurement. Biosignals and Biorobotics Conference (BRC), 2012 ISSNIP.

11. Unnikrishnan, P., **B. Aliahmad**, et al. (2013). "Adaptive colour transformation of retinal images for stroke prediction." Conf Proc IEEE Eng Med Biol Soc **2013**: 7384-7387.

Contents

List of Figures

List of Tables

Chapter 1

Introduction

1.1 Introduction

Retinal micro-vasculatures share similar physiological and anatomic characteristics with other vasculatures inside the human body (Patton, Aslam et al. 2005; Liew, Wang et al. 2008). Therefore retina has been used as noninvasive screening window for systemic disease assessment and risk stratification (Doubal, MacGillivray et al. 2010; Kawasaki, Che Azemin et al. 2011; Lim, Cheung et al. 2013) by medical section. Retinal features associated with disease condition can be classified as either local or global features according to their properties whether they correspond to a local entity (e.g. a vessel segment or cross-section) or summarize the entire image. Some of the local features, include arteriolar and venular diameter as indicator of hypertension (Wong, Klein et al. 2004), stroke (Wang, Mitchell et al. 2002), diabetes mellitus (Wong, Klein et al. 2002) and Coronary Heart Disease (CHD); vessel tortuosity and branching angle as indicator of cardiovascular diseases (Cheung, Zheng et al. 2011) and type-1 diabetes (Sasongko, Wang et al. 2010) respectively. Global feature includes Fractal Dimension (FD) as measure of the complexity of the entire retinal vasculature. The alteration in this parameter has been shown to be associated with early diabetic retinopathy (Cheung, Donaghue et al. 2009) and stroke (Baker, Hand et al. 2008; Kawasaki, Che Azemin et al. 2011).

1.2 Problem Statement

Diameter measurement as an important disease biomarker requires vessel edges to be located; however, perception of edge is subject to image contrast, shadows, lighting condition and even retinopathy legions. Grader's manual intervention may also be required to compensate for the impairing effect of such image artifacts and therefore they may not be suitable for automation

purpose. One common limitation of the mentioned diameter measurement methods in section 1.1 is that they perform pixel classification to find vessel edge or non-edge pixels based on different algorithms and criteria. As the vessel contrast varies greatly across retinal images (Xiayu, Niemeijer et al. 2011), this will lead to large variations among different measurement techniques and manual ground truth (Chandler, Gangaputra et al. 2011) and may significantly affect the association of measured values with a disease condition in the assessment studies. Therefore, due to these large variations, most of the available techniques have not been accepted by clinicians for real world application. Also there is need for automation of eye fundus imaging analysis, for the purpose of increased accuracy, reliability, performance and processing speed. The research has identified "*errors in accurate edge pixel localization*" as the main reason of large variances among different measurement techniques and the most important limitation of accurate diameter quantification. However, in most cases, the diameter is measured to study the variations among case and control groups after several years follow up. In other words, in such analyses the actual value of diameter is less important than the variation itself. Current methods rely on edge detection and measure diameter before and after the disease incidence to identify the corresponding variations. Moreover, diameter is a local feature of a specific cross-section which needs to be generalized and transformed into a global feature associating with the entire image. Introduction of vessel summary formula (Central Retinal Vein Equivalent (CRVE) and Central Retinal Artery Equivalent (CRAE) is a justification of the need for such global feature. This work has tested a range of novel image analysis techniques on real clinical data to validate the proposed solutions.

1.3 Hypotheses

This research has been conducted based on the following hypotheses:

Hypothesis 1: It has been hypothesized that direct analysis of gray scale retinal vessel cross-section profile and accurate profile modeling would substantially improve vessel diameter measurement in terms of accuracy and reliability.

Hypothesis 2: It has also been hypothesized that when the actual diameter is not required, edge independent quantification of diameter variations can overcome the problem of accurate edge point localization and can be achieved through analysis of vessel cross-section intensity profile as a time series signal based on fractal concept. This would combine the advantage of fractal as a global feature with diameter variation as local entity as well as making it suitable for fully automatic processing without dependency on image segmentation or binarization. Therefore, the rationale behind this hypothesis is to provide an improved technique for quantification of retinal vessel diameter variations to find applications in clinical settings and study its performance on subjects with history of systemic diseases including CHD, stroke and type 2 diabetes.

Hypothesis 3: Following the work performed by Hao et al. (Hao, Sasongko et al. 2012) which proposed an ECG-synchronized retinal photography method and studied the variation of retinal vessel geometry (e.g individual and summary vessel diameter, branching angle, tortuosity and ...) due to cardiac cyclic pulsatile movements; this work has hypothesized that cardiac cyclic vessel pulsation may also affect other measurement such as FD and any newly developed technique and therefore further investigation is required to examine whether ECG-synchronized retinal photography would affect the previously hypothesized "*edge independent caliber-variation quantification technique*" in this thesis and help reducing erroneous measurement variations.

1.4 Research Aim and Objectives

The aim of this research is to develop novel methods for retinal vessel caliber measurement using fundus images and provide a technique for quantification of disease associated vessel diameter variations as a feature to be applicable in clinical setting for diabetes and stroke disease assessment. The objectives of this research are to:

- Develop an improved retinal vessel profile model and using it for automatic vessel diameter measurement considering aforementioned limitations for the studies in which actual vessel caliber is of interest.
- Develop a novel feature independent of vessel edge location to quantify vessel diameter variations for the cases when the alteration in diameter is more important than actual vessel diameter.

- Apply the proposed feature for automatic assessment of Coronary Heart Disease (CHD), stroke and diabetes assessment.
- Study the effect of retinal vessel cardiac cyclic pulsations and ECG-synchronized photography on FD of retinal images and the hypothesized edge independent technique.

This research reports accurate modeling of vessel cross-section profile for diameter estimation and the use of one dimensional (1D) fractal analysis of the gray scale profile as a time series signal and investigates the relationship of change in the complexity with vessel diameter variations after disease incidence. This research has combined the fractal concept as a global measurement and vessel diameter as a local property and identified a new feature suitable for automatic disease assessment independent. The main advantages of the new feature are:

i. While it provides an indication of vessel diameter, the measurement process does not require the vessel boundaries to be tracked or localized.
ii. Ability for quantification of fine vessels with diameter as small as one pixel.
iii. Less sensitive to background noise and image artifacts compared to other measurement techniques.
iv. Providing a summary value significantly associated with CHD, stroke and diabetes pathological changes in the statistical sense.

1.5 Outline of the Thesis

The thesis on this research work is organized into nine chapters. Chapter 1 presents an introduction to the research work and introduces the limitation of the previously reported techniques in automatic quantification of retinal vessel diameter.

Chapter 2 provides a brief description of human eye structures including retina and an overview of the related works and literatures on automatic retinal vessel diameter measurement and fractal feature extraction methods used for retinal image analyses.

Chapter 3 explains a novel multi-step regression method for automatic retinal cross-section profile modeling and its application for vessel diameter measurement. A comparative study of the state of the art algorithms and the proposed technique has been provided.

Chapter 4 covers a novel unsupervised automatic diameter measurement technique based on linear discriminant analysis and a comparative analysis with existing measurement techniques.

Chapter 5 introduces an edge independent technique for quantification of vessel diameter alterations based on fractal theory and a new disease biomarker (feature) suitable for automation purpose.

Chapter 6 covers clinical and real world application of the proposed biomarker for automatic and grader independent assessment of Coronary Heart Disease (CHD) and stroke.

Chapter 7 reports the clinical and real world application of the proposed biomarker for automatic and grader independent assessment of type 2 diabetes among cohort population study of individuals with mild non-proliferative diabetic retinopathy (NPDR).

Chapter 8 reports a new methodology for visualization of retinal vessel pulsatile motions and diameter trend estimation at the grayscale level using ECG synchronized still fundus images. It also covers variation of the proposed biomarker in the presence of vessel pulsations and its association with different cardiac cycle points. Its correlation to vessel diameter change across the cardiac cycle has also been presented. Statistical significance of FD variations due to vessel pulsatile motion has also been reported and compared with estimated diameter trend.

Chapter 9 presents the conclusion of this work and discusses the main contributions of this research work.

Chapter 2

Literature review

2.1 Introduction

This chapter provides a brief description of human eye anatomy with more emphasis on the retina structure and disease manifestation in retina. The disease related abnormalities in retinal vessel diameter and morphological structure are introduced. The overall review of the works related to quantification of retinal vessel diameter and FD estimation as the two features frequently measured in real-world applications for automatic risk assessment of disease incidence, is provided. Therefore, the review in this section covers two major research areas in human retinal image analysis:

- Automatic retinal vessel diameter quantification techniques
- Fractal theory based analysis of retinal vasculature pattern

2.2 Human eye anatomy

A cross-sectional view of the human eye is shown in Figure 2.1.a. It consists of three major layers including external, intermediate and internal layers. The external layer includes sclera (white of the eye) and cornea which forms the supporting wall of the eyeball. The cornea is a transparent layer covering both iris and pupil. Iris is the colored circular muscle which controls the size of the pupil (a dark circular opening in the iris) and the amount of light entering the eye ball based on the environmental lighting conditions. The second layer is the intermediate layer which is subdivided into two anterior (iris and ciliary body) and posterior (choroid) parts. The internal layer is the retina (Figure 2.1.b), a thin (thickness: 0.5 mm approx.) multi-layer photon sensitive circular disc of diameter between 30 and 40 mm (Kolb H, Fernandez E et al. 1995). In

the center of retina there is a circular to oval shape like area of about 2×1.5 mm called the optic nerve. The blood vessels nourishing the retina enter/exit the eyeball through the center of the optic nerve. Optic nerve also carries the electrical impulses to the visual cortex of the brain which are generated by the light-sensing cells on the retina. There is small extra sensitive area located in the center of the retina and is responsible for central vision. This area is called Macula and contains fovea in the middle that provides clearest vision.

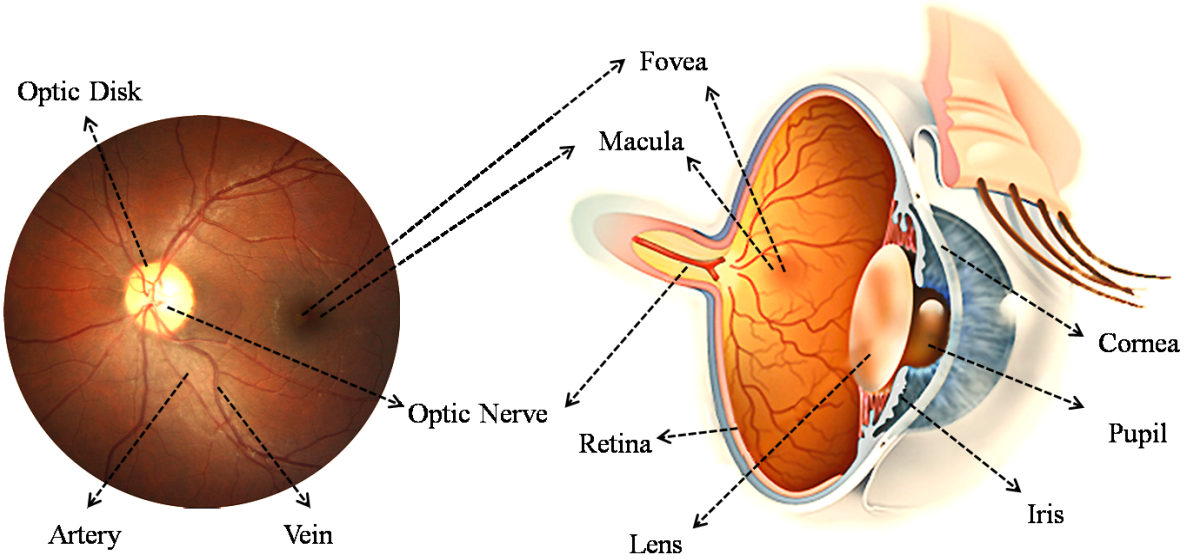

Figure 2.1: Major structures in human retina. (a) Cross-sectional illustration of human eye [Source: WebMD LLC.(WebMD 2009)]. (b) Human retina photograph taken by fundus camera (Cannon CR-1)

There are two sources of blood supply nourishing retina. The choroidal blood vessels that carry about 65 to 85% (Henkind P, Hansen RI et al. 1979) of blood flow to the outer retina, particularly to the photoreceptor cells and the central retinal artery that supply inner retinal layers from the optic nerve head. Within the optic nerve head the artery subdivides in to four main branches to supply the four quadrants of the retina. The large arteries in each quadrant extend within the retina toward the periphery areas and are progressively subdivided to form arteries with smaller diameters. When they reach ora serrata (a junction between retina and ciliary body),

they return as a continuous venous drainage system with distribution pattern similar to the arteries. In general these vessels emerge in radial direction from the optic nerve and curve towards and around the fovea.

2.3 Disease manifestation in retina

Retina is a place to manifest many important diseases and provides a unique opportunity for disease investigation and screening the conditions. This uniqueness is mostly due to retinal microcirculation characteristics which share similar anatomical, physiological, and embryological characteristics to cerebral small vessels (Yin Wong 2004) and also the ability of retina to be viewed non-invasively and in vivo with the help of fundus photography. Examples of the ocular or eye-related diseases include Macular Degeneration (MD) and glaucoma. MD, often referred to as Age-related Macular Degeneration (AMD), is a type of degenerative disease that causes progressive loss of central vision. Vision loss occurs because of breakdown or thinning of a layer of cells underneath the retina (Retinal Pigment Epithelium (RPE)) building up fatty deposits (drusens) in the macular region (dry AMD) or due to abnormal growth of choroidal vascular structure into the macula (wet AMD) (Abramoff, Garvin et al. 2010). Glaucoma is characterized by gradual damage to the optic nerve which leads to permanent vision loss and blindness if it is not detected and treated early. Glaucoma manifests in retina by cupping of the optic nerve head. Therefore the ratio of the optic disc cup and the neuroretinal rim surface area (area of optic disk containing neural elements) as well as its color and uniformity, can be indicative of the presence and progression of glaucoma.

Except the ocular diseases, retina can also be affected by a number of systemic diseases which manifest themselves in retina with particular retinopathy signs. Diabetes mellitus and cardiovascular diseases are two examples of the most prevalent systemic diseases. Their ocular manifestation can be viewed and studied via eye funduscopy and retinal image analysis as follow:

2.3.1 Diabetes mellitus

"Diabetes mellitus", simply known as "diabetes" is chronic abnormality of blood glucose metabolism resulting from either altered (type 1) or insufficient and ineffective insulin production (type 2) by the pancreas. This will lead to presence of elevated blood glucose (Hyperglycemia) and damage to the vessel walls in retina known as diabetic retinopathy. The corresponding retinopathy signs include exudates, haemorrhages, microaneurysms, re-growth of new blood vessels (Neovascularisation) and cotton-wool patches (retinal infarcts) some of which have been shown in Figure 2.2.

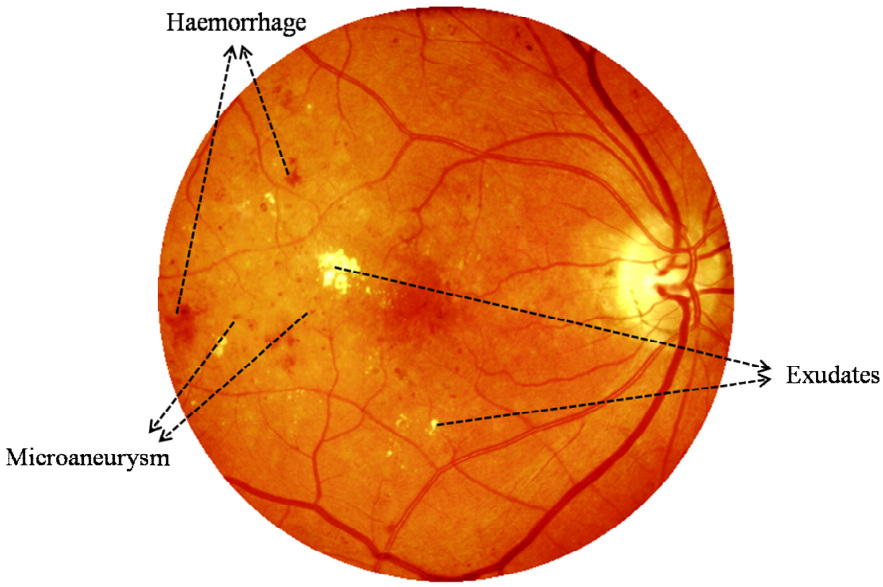

Figure 2.2: Example of a fundus image with severe diabetic retinopathies [Source: (Kolb H, Fernandez E et al. 1995) with slight modifications]

Studies have assessed association between a number of biomarkers in retina and risk of diabetes. This includes retinal vascular diameter (Ikram, Cheung et al. 2013) and the resulting early pathological alterations associated with disease incidence. It has also been used as a predicting factor for retinopathy risk assessment in terms of whether the patients may develop retinopathy and other complications in future (Ikram, Cheung et al. 2013). For middle-aged persons (45 to 64), retinal arteriolar narrowing is associated with incidence of diabetes independent of the known risk factors (Wong, Klein et al. 2002). Elsewhere, significantly wider summary retinal

arteriolar and venular caliber has been reported in patients aged 45 to 84 with mild and no diabetic retinopathy (Wong, Islam et al. 2006; Kifley, Wang et al. 2007) and used for analysis of the progression of retinopathy in type 1 cases (Klein, Klein et al. 2004; Wong, Shankar et al. 2004). However, vessel diameter is one of the many structural parameters of retinal vasculature which conveys a very specific aspect of the retinal vascular network. Other structural changes including larger arteriolar branching angle and increased tortuosity have also been reported as indicator of longer duration of diabetes and higher A1C respectively (Sasongko, Wang et al. 2010). Diversity of such parameters and a lack of method to summarize geometrical variations of branching pattern have led to consideration of FD for quantifying early diabetic microvascular damage. Such measure has shown promising outcome in microvascular disease assessment and is highly correlated with a number of biological parameters (Cheung, Donaghue et al. 2009). The study of early diabetic retinopathy shows that increasing retinal vascular FD was significantly associated with increasing odds of retinopathy (Ning Cheung, Kim C. Donaghue et al. 2009). In the type 1 diabetes patients, the study found that persons with FD were more likely to have proliferative retinopathy (Grauslund, Green et al. 2010). No association between FD dimensions and any retinal circulatory parameters of the retinal arterioles was found in patients with type 2 diabetes mellitus (Nagaoka and Yoshida 2013).

2.3.2 Cardiovascular disease

In addition to diabetes, fundus photography allows for risk assessment of cardiovascular diseases and its subsequent complications. This includes hypertensive retinopathy which is referred to retina damage due to hypertension (high blood pressure). It is associated with long term risk of stroke (Gorelick 2002; Ong, Wong et al. 2013) as the second commonest cause of death worldwide (Toronto and Ontario 2001). Some of the first observable signs are flame hemorrhages and cotton wool spots. As the disease progresses, hard exudates may appear around the macula along with swelling of the macula and the optic nerve resulting into vision impairment. Another, associated clinical biomarker is reduction in arteriolar diameter which is assessed by measuring the reduction in arteriolar diameter to venous diameter ratio (AVR) (Wong, Knudtson et al. 2004; Wong, Islam et al. 2006). However, reduced AVR does not

necessarily indicate constant venular diameter and therefore reflecting generalized arteriolar narrowing. Venular diameters may also change (usually increase) due to different pathologic conditions including atherosclerosis, inflammation, cholesterol levels and stroke event (Ikram, de Jong et al. 2004). For instance, this ratio for the stroke incidence corresponds to both arteriolar narrowing and venular widening (McGeechan, Liew et al. 2009; Abramoff, Garvin et al. 2010). Therefore using AVR, the exact contribution of individual arteriolar and venular diameters to disease event may remain unknown. For more effective translation of retinopathy signs into clinical application and assessment purpose, hypertensive retinopathy, in a relatively new classification, is classified into four levels of none, mild, moderate and severe (Liew and Wang 2011) based on the observable retinopathy signs. Generalized and focal arteriolar narrowing and arteriovenous nicking are referred to as mild hypertensive retinopathy signs. The presence of lesions such as microaneurysms and hemorrhages, hard and soft exudates (cotton wool spots) indicate the moderate level while optic disc edema is referred to as a sign for severe stage (Liew and Wang 2011). Example of retinal images with some retinopathy signs are shown in Figure 2.3. Summary of the previous findings on different retinal features and their association with systemic diseases are presented in Table 2.1.

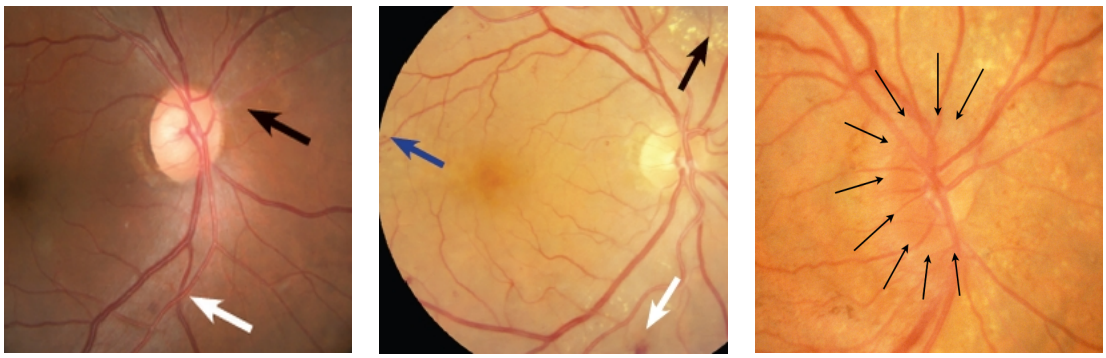

(a) (b) (c)

Figure 2.3: Hypertensive retinopathy signs. (a) Mild: generalized and focal arteriolar narrowing (black arrow), arteriovenous nicking (white arrow) [Source: (Mayuri Bhargava and Wong 2013)] (b) Moderate: arteriolar narrowing with arteriovenous nicking, flame-shaped hemorrhages (white arrow), hemorrhages (blue arrow), and hard exudates (black arrow) [Source: (Mayuri Bhargava and Wong 2013)] (c) Severe: Optic disc edema [Source: (The University of Iowa 2006)]

Table 2.1 Summary of retinal features and their association with systemic diseases.

Retinal Features	Diagnostic Application
Individual vessel diameter (Arteries & Veins)	Hypertension, Stroke, Diabetes, Coronary Heart Disease
Fractal Dimension	Diabetes, stroke
Tortuosity	Cardio Vascular Disease, Type 1 diabetes
Branching Angle	Diabetes
Length–Diameter Ratio (LDR)	Diabetes

2.4 Fundus image acquisition techniques

Retina photography, also known as funduscopy, is a technique for 2D projection of 3D retinal tissues onto an imaging plane by using reflected light rays. The amount of reflected rays appears as intensity values on the image plane. Depending on the type of image, emitted light and acquisition procedure, the funduscopy techniques are classified into several categories (Abramoff, Garvin et al. 2010).

- Monochromic fundus photography (Timothy J. Bennett 2011): In this technique which is also known as Red-free funduscopy the retina image is taken by using colored or monochromatic illumination a at specific wavelengths in order to enhance the visual contrast of some anatomical details. The basic principal behind this technique is based on the fact that, a color will seem lighter through a filter of the same color and darker through a filter of its opposite color. For instance if an object is red, it will appear lighter through a red filter and darker through a cyan filter after being photographed. For retinal imaging visibility of the anterior retinal layers, which are almost transparent in white light, will increase by blue light. However, retinal pigmentation and blood vessels absorb the blue light and leave a dark background on the image. Blood vessels also absorb the green light but compared to blue light retinal pigmentation partially reflect the green light. Green light increases the visibility of the retinal vasculature and other disease related retinopathy signs such as hemorrhages, drusen and exudates and therefore is useful for automatic retinal image analysis and disease assessment applications. In red

light, the optic disk and retinal pigmentation appear very light and overall fundus contrast gets greatly reduced as most retinal structures are red in color.

- Color fundus photography: It is one of the most common techniques for retinal funduscopy in which the image intensities are represented by the amount of light reflected from three colors (spectral band) of Red, Green and Blue (RGB).

- Stereo fundus photography: stereo photography is a technique in which for each subject the images are taken from two or more different view angles for increased depth resolution and 3D representation of the retina in viewer's brain (Yang-Williams 2002). In other words, when a person views the left stereo image with the left eye and the right image with the right eye, the depth will be recreated inside the brain which can provide better diagnostic interpretation especially in follow-up studies.

- Hyperspectral imaging: In this method, the image is produced by reflection of multiple specific wavelength bands (Abramoff, Garvin et al. 2010). It allows wavelength-specific visualization of retinal lesions and allows simple localization of retinal and disc pathology for disease diagnosis and management application (Nourrit, Denniss et al. 2010).

- Scanning Laser Opthalmoscopy (SLO): In this technique a narrow low power (<100 μW) 1mm laser beam is used to scan the fundus and the image intensities correspond to the amount of reflected laser light. SLO using single wavelength laser light was first introduced by Webb et al. (Webb, Hughes et al. 1980) and later modified by combining red, green, and blue lasers using fiber optics (Manivannan, Van der Hoek et al. 2001). It offers all the advantages of monochromic devices as well as providing true color representation of the fundus.

- Fluorescein angiography: In this technique the images are obtained by the emitted photons from the Sodium fluorescein dye injected into circulatory system (Abramoff, Garvin et al. 2010; Kade Mahesh K and S 2013). The dye is injected into patient's veins through the arm before the image is taken. After about twelve seconds the dye reaches the

arteries of retina. After about two to five seconds the dye reaches the veins in retina by travelling through smaller vessels and capillaries. Retinal photography produces grayscale image in which the vessels appear lighter (in white) than the background. Two different filters are used in this process. A blue filter to produce blue light for illumination of inside the eye and a yellow filter to collect the reflected light. However, the blue light does not pass through the yellow filter. The dye in retinal and choroidal blood vessels absorbs the blue light and emits yellow light instead (Timothy J. Bennett 2011), which can be photographed after passing through the yellow filter. This method is suitable for analysis of flow characteristic in the blood vessels, detection of diabetic neovasculatization, retinal artery and vein occlusions optic disk edema and tumors (Kade Mahesh K and S 2013).

2.5 Retinal image analyses

Due to association of alteration in retinal vascular parameters with systemic diseases, different geometric measures are commonly analyzed with computerized-assisted methods for risk assessment and diagnostic purposes to quantify the retinopathies discussed in section 2.3. These measures include individual vessel diameter, tortuosity, branching angle and length–diameter ratio (LDR) as local features and vessel diameter summary and FD as global measures. The rest of this section specifically covers the available techniques in vessel diameter measurement and FD quantification as the main focus of this thesis due to the importance of these two features in providing early indication of disease manifestation, their frequent applications in clinical setting and being suitable for automatic assessments.

2.5.1 Previous vessel diameter measurement techniques

Several techniques have been published for retinal vessel diameter estimation and edge delineation. Most of the earlier ones are based on direct use of one dimensional (1D) vessel cross-section profile which is defined as “densitometry of the photographs on a line perpendicular to the vessel in a series of reflectance-readings versus location”(Hammer, Leistritz et al. 2001). Figure 2.4 shows an illustration of a vessel profile and some of its important

characteristics including darker intensity compared to the background (for Fundus images), having an overall shape of similar to an inverse second-order Gaussian function and potential for appearance of vessel central light reflex (specular reflections) in high resolution images.

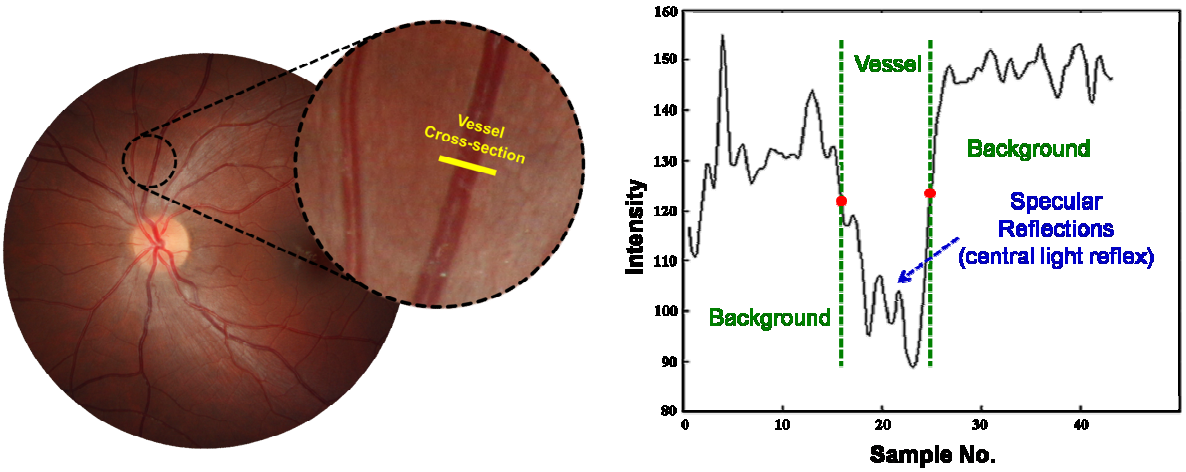

(a) (b)

Figure 2.4: Illustration of vessel cross-section profile. (a) A sample vessel segment and its cross-section line (yellow line) (b) Vessel cross-section profile showing central light reflex, uneven illumination and background noise.

In order to measure vessel diameter, Brinchmann et al. proposed the Full Width Half Maximum (FWHM) method in which the with was defined as the distance between the two points on the vessel intensity cross-section profile where the function reached 50% (Brinchmann-Hansen and Heier 1986) as shown in Figure 2.5.b. This method is easy to implement, however, it is basic, provides low fitting success rate and goodness of fit to the profiles with central light reflex. Similar to FWHM, Gregson et al. (Gregson, Shen et al. 1995) fitted a rectangle to the vessel profile and estimated the width by setting the area under the curve equal to the area under the rectangle. In this method the height of the rectangle was extended between the maximum and minimum intensity values of the vessel profile (Figure 2.5.b). This technique is suitable for application on low resolution images and vessels with diameter of at least 5 pixels.

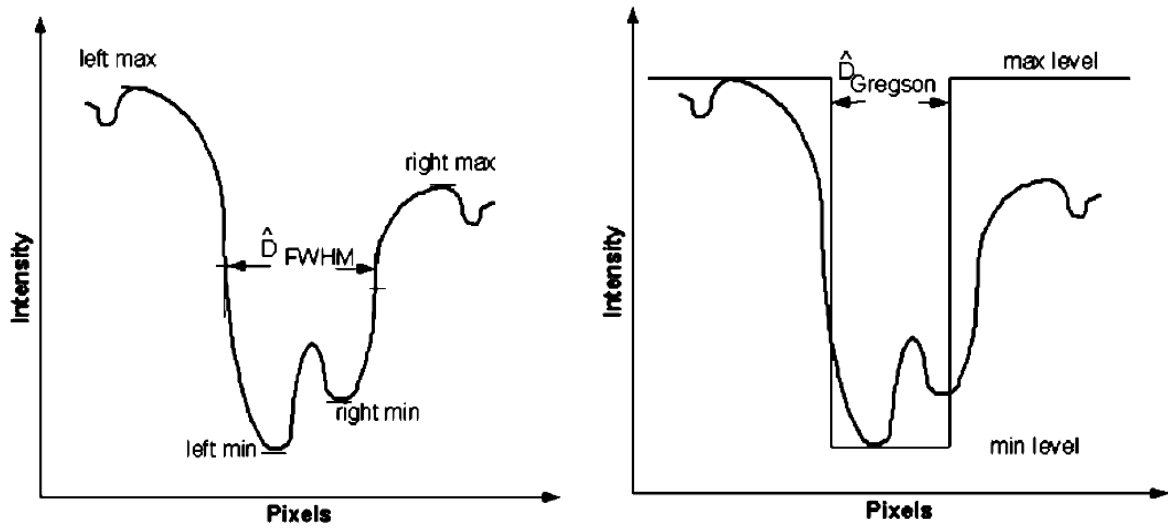

(a) (b)

Figure 2.5: Illustration of early diameter measurement techniques (Lowell, Hunter et al. 2004) (a) Full width at Half Maximum (b) Rectangular fitting method (© 2004 IEEE)

In another work, the profile was approximated by 1D Gaussian function based on the assumption that the intensity profile follows a symmetric Gaussian function (Zhou, Rzeszotarski et al. 1994). This method has the convenience of estimating diameter with a single parameter (Spreading factor of the fitted Gaussian function); however, the symmetry assumption is not always true as the profile may not sometimes look symmetric because of dissimilar illuminations between both sides of a vessel cross-section. Also this model does not represent vessel central light reflex. This model was further improved by Gao et al. (Gao, Bharath et al. 2000) with introduction of the twin-Gaussian model. In this model the inverted vessel profile was represented by difference of two 1D Gaussians to provide better representation of vessel central light reflection:

$$G(x) = a_1 e^{-(\frac{x-a_2}{a_3})^2} - a_4 e^{-(\frac{x-a_5}{a_6})^2} + a_7 \tag{2.1}$$

Where x is the pixel location, a_1, a_2 and a_3 are the amplitude, spatial displacement and spreading factor of the Gaussian function respectively, which correspond to the overall shape of vessel profile. a_4, a_5 and a_6 correspond to the negative Gaussian modelling the central light reflection and have definitions similar to a_1, a_2 and a_3 respectively. a_7 is just a DC bias to

compensate for the lighting conditions of the background. The values of the parameters were obtained through a curve fitting process using non-linear Levenberg-Marquardt method (Levenberg 1944) and the width was defined as $2.33 \times a_3$ assuming a linear relation-ship between the standard deviation (SD) of the main Gaussian and actual vessel diameter. This model was later extended to a 2D version by Lowell et al. (Lowell, Hunter et al. 2004) by using Gaussian or Difference of Gaussian functions, based on the absence or presence of the light reflex. In case of no central light reflex, Lowell et al. proposed application of the following equation for profile modelling and diameter measurement:

$$f_{x,y} = t - h_1 e^{-s_1 \alpha^2} \tag{2.2}$$

$$\alpha = x \sin(\theta) - y \cos(\theta) - \mu \tag{2.3}$$

where x and y are the cross-sectional range to map the data profile, t is the profile maximum, h_1 is the height (amplitude) of the Gaussian, $s_1 = \frac{1}{\sigma_1^2}$ is the width of the Gaussian, θ and μ correspond to the model orientation and displacement of the Gaussian centre respectively (Figure 2.6.a and Figure 2.6.b). Using this model the width was estimated by the sigma parameter of the Gaussian coinciding with the inflexion points on the vessel edge slopes. In the presence of central light reflex, Lowell et al included additional parameters (an inverse Gaussian) to model and control the shape and size of the central light reflex as in equation 2.4:

$$f_{x,y} = t - (h_1 e^{-s_1 \alpha^2} - h_2 e^{-s_2 \alpha^2}) \tag{2.4}$$

where h_2 and s_2 are the height and width of the inverse Gaussian function respectively (Figure 2.6.c and Figure 2.6.d).

In order to estimate the width using this updated model, the location of the inflexion points were obtained through a line search procedure and detecting zero of the second order derivative of the model.

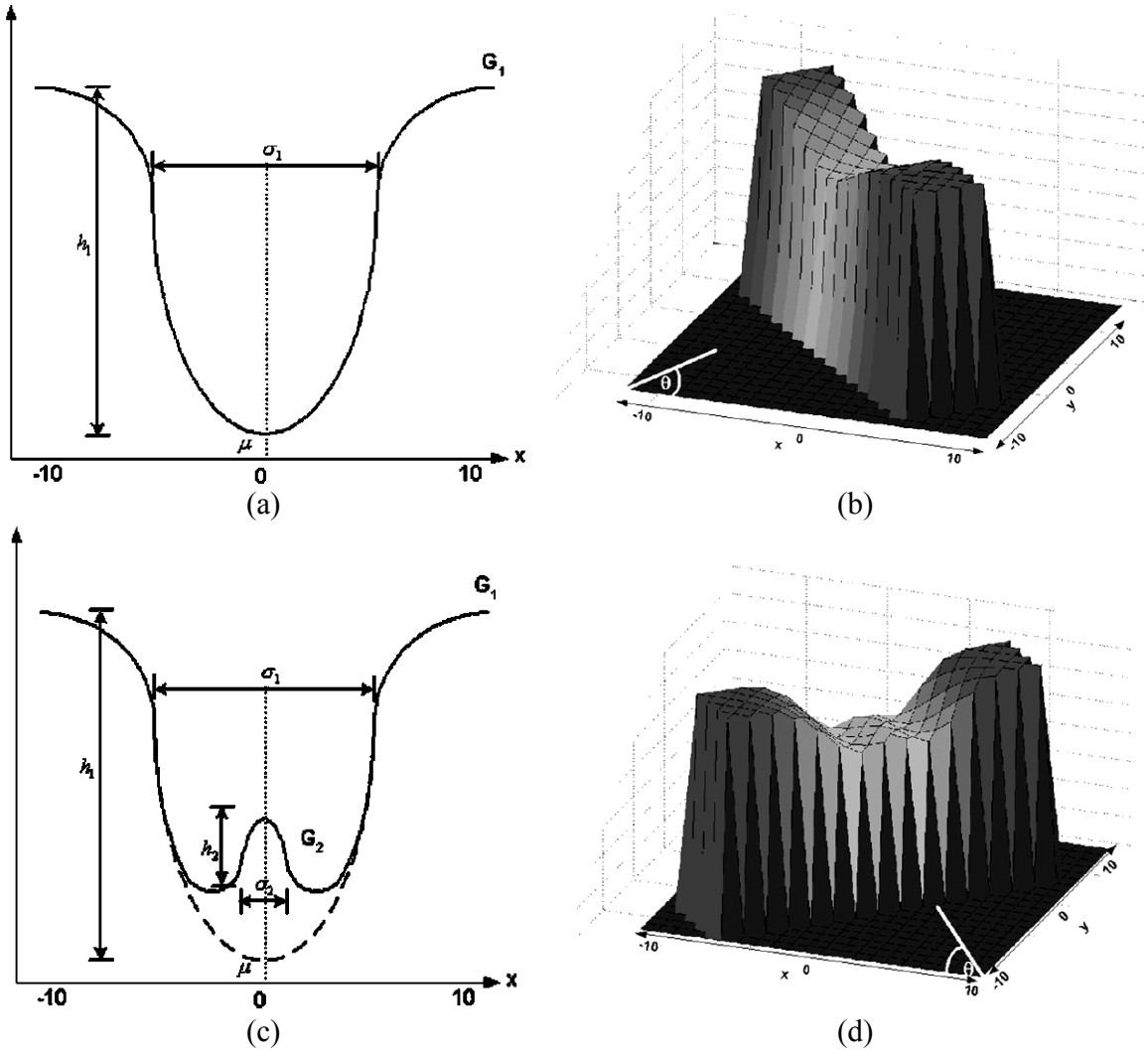

Figure 2.6: Models for vessel diameter measurement proposed by Lowell et al. (Lowell, Hunter et al. 2004) (a) 1D representation with no central light reflex (b) 2D representation with no central light reflex (c) 1D representation with central light reflex (d) 2D representation with central light reflex (© 2004 IEEE).

Chapman et al. (Chapman, Witt et al. 2001) proposed the sliding linear regression filter (SLRF). In this method a line was fitted on vessel cross-sectional profile to measure the gradient of intensity change within a window of size W progressively moved across the profile. The window shift was performed with one-pixel intervals and at each pixel n corresponding to the centre of the window, slope of the best least square fitting line was calculated (m_n) as shown in Figure 2.7. The actual edge position X_{edge} was mathematically presented by the following equation:

$$X_{edge} = \frac{\sum_i x_i m_i}{\sum_i m_i} \tag{2.5}$$

for all $i$such that $m_i > 0.5m_{\max}$and $m_i < 0.5m_{\min}$, where $m_{\max}$and $m_{\min}$ are the maximum and minimum values of the slopes respectively. However, the SLRF method relied on the spreading factor a_3 (equation 2.1) from the twin-Gaussian model to adjust the window size *W*.

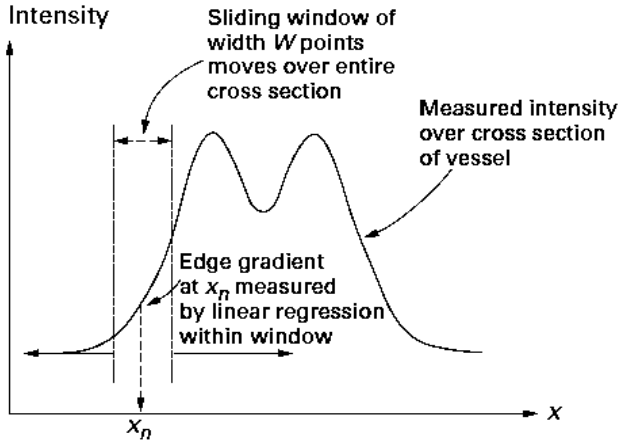

Figure 2.7: Illustration of Sliding Linear Regression Filter (SLRF) (Chapman, Witt et al. 2001) © 2001 BMJ

Al-Diri et al. (Al-Diri, Hunter et al. 2009) proposed the extraction of segment profiles (ESP) algorithms based on growing a Ribbon of Twins (ROT) and active contour model over segmented vessels. Two merging pairs of contours were used at each edge (one inside and one outside the vessel) to converge to the boundary and delineate the edges for diameter measurement. However, this method does not detect both boundaries across a vessel segment simultaneously. The importance of independent boundary extraction led to the work by Xiayu et al. (Xiayu, Niemeijer et al. 2011). They established a graph based method in which the vessel boundaries were segmented simultaneously using a two-sliced, 3D surface segmentation scheme. This was followed by computing a minimum closed set in a node-weighted directed vesselness map graph and determining the optimum surface. The Vessel width was estimated by taking the distance between the two nodes on the optimal surface from the two slices. However, the

accuracy of this technique relies heavily on quality of initial image segmentation. Table 2.2 summarizes the strength and limitations of previous diameter measurement techniques. It should be noted that, according to the retinal blood vessel model provided by Brinchmann et al. (Brinchmann-Hansen and Heier 1986), unless Fluorescein Angiogram is used, measurement of retinal vessel diameter using color fundus images is limited to erythrocyte column of the blood vessels and does not include surrounding plasma zone. Therefore the measured values are not true representation of vessel diameter.

Table 2.2 summary of the strengths and limitations of historical and latest diameter measurement techniques

Method	Strengths	Limitation
FWHM	simple, easy to implement	Basic, low accuracy, low success rate, does not consider vessel central light reflex
Rectangular	Simple, suitable for low resolution images	Suitable for vessels with diameter greater than or equal to 5 pixels, does not consider the central light reflex
1D Gaussian	Estimates the diameter with single parameter.	Does not model the central light reflex, assumption of symmetry for vessel profile.
Twin Gaussian	Models the central light reflex, has the convenience of diameter estimation with single parameter, compensates for different background lighting conditions. Estimates the diameter with single parameter.	Assumption of symmetry for vessel profile and following overall shape like inverse Gaussian function
2D Gaussian	Similar to twin Gaussian but with better fit Estimates the diameter with single parameter.	Assumption of symmetry for vessel profile and following overall shape like inverse Gaussian function
SLRF	Easy to implement, works on any profile shape. It is not based on curve fitting.	Relies on Spreading factor from Twin-Gaussian model
ESP Method	Independent boundary extraction, suitable for blurred or difficult edges	Does not detect boundaries simultaneously
Graph Based Method	detects both boundaries simultaneously	It relies largely on initial image segmentation (veselness map)

2.5.2 Fractal dimension

As stated earlier in section 2.3, FD has been employed by a number of studies for quantification of retinal vasculature complexity. For instance, Mainster (Mainster 1990) characterized retinal arterial and venous patterns using fluorescein angiogram images and reported different FD values of 1.63 ± 0.05 and 1.71 ± 0.07, for arterial and venular geometries respectively. Ying et al. (Huajun, Ming et al. 2007) suggested the use of FD for optic disc localization and differentiation from hard exudates and other artefacts.

FD was first introduced by Benoit Mandelbrot (Mandelbrot 1983) by drawing attentions to the length of the coastline of Great Britain. He has argued that the length of the coastline can have different interpretations depending on the estimation method. For instance, if one measures the length of the coastline by covering its perimeter by strips of length λ to create a polygon, the perimeter of this polygon will be an estimate of the coast line length. However, this can vary by changing the step size (λ). Using smaller and smaller steps can reach to the conclusion that the coastline of Great Britain is infinite. Therefore accuracy of estimation should always be linked to the statement of how it is deduced (Kaye 1989). Similar problem will exist for the measurement of area and volume. Curves, surfaces and volumes can sometime become so complex that ordinary measurement may not help.

Mandelbrot suggests measuring the degree of complexity by evaluating how fast the length would increase with respect to reduction in scale (Jürgens, Saupe et al. 1992). The idea is based on the assumption that scale and these quantities (length, area & volume) do not change arbitrary and the association relies on a power-law which allows for calculation of one factor from another. This law also explains the term “Dimension” which in the past, it was a major problem for mathematicians to define its exact properties. FD can be calculated by a number of methods which have been explained in the rest of this section:

2.5.2.1 Binary Box-Counting fractal dimension

There are many established versions of Box-counting algorithms available for FD quantification of the signals (Raghavendra BS and Narayana Dutt D. 2010). Binary Box-counting FD is a special form of Mandelbrot's fractal dimension which has been frequently used for analysis of any structure in the plane or space. Also it is generally accepted for retinal image analyses by earlier works for quantifying complexity of retinal vasculature (Family, Masters et al. 1989; Masters 2004; Liew, Wang et al. 2008). This method is applicable on binary images and involves superimposing the structure (vascular network in retinal images) with a grid of boxes with varying (either deceasing or increasing) side length of size (*R*) and counting the number of boxes (*N)* corresponding to each "*R"* containing at least one pixel of the structure. The slope of the best fitting line to the data points on a Log-Log plot of $Log(N)\,Vs\,Log(\frac{1}{R})$ corresponds to Box-Counting fractal dimension which is a number between 1 and 2 for a plane as in equation 2.6.

$$FD_{BC} = \frac{Log(N)}{Log(\frac{1}{R})} \tag{2.6}$$

An example of mesh grid superimposition on a binerized retinal image and the estimated Box-Counting dimension is shown in Figure 2.4. The boxes that contain pixels from the vessel structure are shown in red.

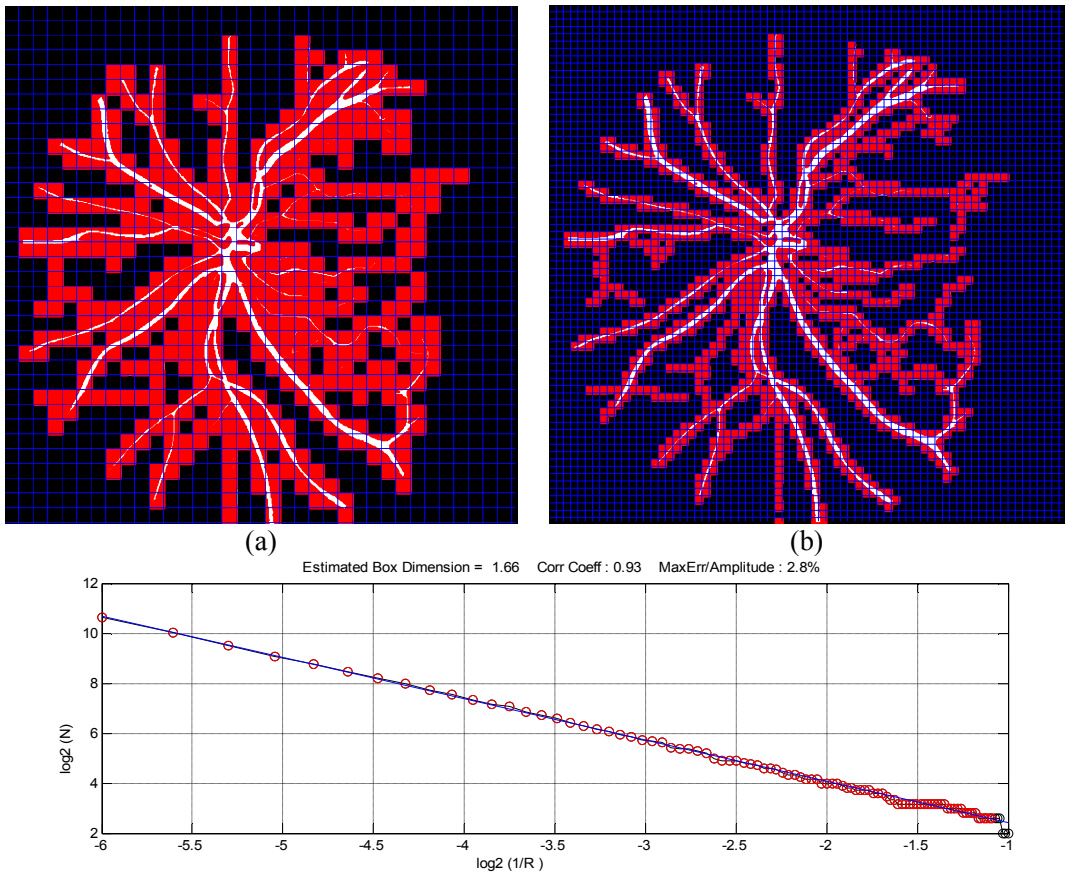

Figure 2.8: Mesh grid of varying box-sizes (scales) covering binerized retinal vasculature. (a) e.g. Box size of R=8 Pixels (b) e.g. Box size of R=16 Pixels (c) The slope of the straight line fitted on *Log (N)* Vs *Log (1/R)* is the box-counting fractal dimension (Here:1.66).

2.5.2.2 Differential Box-Counting Fractal Dimension

Differential Box-Counting (Sarkar and Chaudhuri 1994) is a modification of binary Box-Counting introduced in section 2.5.2.1, with the advantage of being applicable to gray scale images which does not require image segmentation or binarization making it suitable for automatic analyses. It is based on the basic binary Box-counting formula given by equation 2.6 but with different manner of counting the number of boxes (*N*). Assuming an image of size $S \times S$ is a scaled version of its original size $M \times M$ pixels with S being an integer between 1 and $\frac{M}{2}$

($1 < S \le \frac{M}{2}$). The side length of size R is then estimated as $R = \frac{M}{S}$. The image is considered in a 3D space with (x, y) denoting the 2D coordinates (positions) on a plane and the gray level intensity as the 3rd dimension. The 2D coordinate was covered with grids of size $S \times S$ each having a column of boxes of size $S \times S \times S'$ with S' being height of a single box. Considering total number of gray levels is G (i.e. for 8 bit gray scale image G=255), then $\left\lfloor \frac{G}{S'} \right\rfloor = \left\lfloor \frac{M}{S} \right\rfloor$ where $\lfloor x \rfloor = floor(x)$ denoting the largest integer not greater than x. The boxes are numbered sequentially as shown in Figure 2.9.

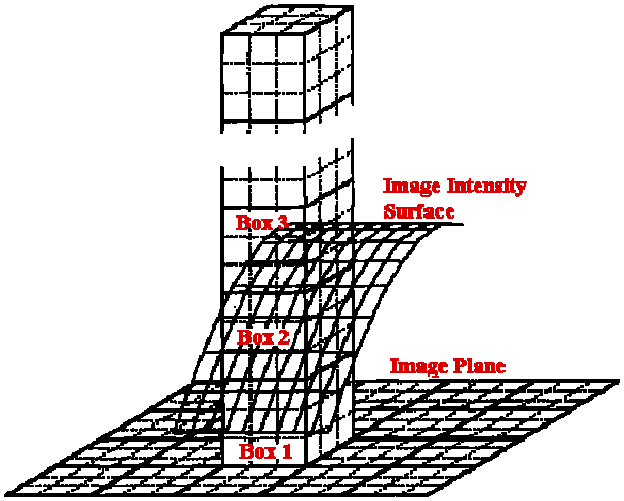

Figure 2.9: Illustration of Gray scale (differential) box counting (Sarkar and Chaudhuri 1994) © 1994 IEEE

For each grid (i, j) and using the numbers assigned to each box, the distance between the boxes containing minimum and maximum gray level of the image (n) is obtained as follow to find the contribution of N in the $(i, j)^{th}$ grid:

$$n(i, j) = l - k + 1 \tag{2.7}$$

where l and k are the numbers associated with the boxes containing maximum and minimum gray levels respectively. The overall N corresponding to each value of R(i.e. each value of S) can be obtained by summing all the individual contributions:

$$N = \sum_{i,j} n(i,j) \tag{2.8}$$

Likewise the Binary BC in equation 2.6, a Log-Log plot of $Log(N)\ Vs\ Log(\frac{1}{R})$ yields Gray-scale (differential) BC fractal dimension. This can be interpreted as the self-similarity within the image, and the value of the FD is between 2 and 3

2.5.2.3 Higuchi's fractal dimension

Higuchi (Higuchi 1988), measures the FD of a set of points in the form of 1D time series data sequence. When it comes to image processing, the 1D data sequence can be extracted by scanning the image along one of the possible directions (e.g. horizontal, vertical, radial or …) while recording the gray scale intensity values. (Ahammer 2011). Assuming $x(1), x(2), \ldots, x(N)$ a set of N discrete gray values extracted along a fixed direction at the points $x(1), x(2), \ldots, x(N)$ with regular intervals (fixed sampling frequency); k subsets of new data series S_k^1, S_k^2, … , S_k^k are defined as follow:

$$S_k^m: \quad x(m), x(m+k), x(m+2k), \ldots, x\left(m+\left\lfloor \frac{N-m}{k} \right\rfloor k\right) \qquad (m=1,2,\ldots,k) \tag{2.9}$$

Where $\lfloor\ \rfloor$ is the Gauss' notation representing the *floor* function (the largest previous integer). m and k are the integers denoting the initial and the intervals respectively. Parameter $L_m(k)$ is defined as in (2) for each S_k^m corresponding to the curve length of that subset.

$$L_m(k) = \frac{A}{k}\left(\sum_{i=1}^{\left\lfloor \frac{N-m}{k} \right\rfloor} \left| x(m+ik) - x(m+(i-1)k) \right|\right) \tag{2.10}$$

where $A = \frac{N-1}{k\left\lfloor \frac{N-m}{k} \right\rfloor}$ is the normalizing factor for the subset curve length. The total curve length is obtained by averaging the subset lengths over the whole interval (k sets of $L_m(k)$). The maximum value that k can obtain is equal or less than $\left\lfloor \frac{N}{2} \right\rfloor$. The change of this length as a function of k on the logarithmic scale is considered as measure of the Higuchi's Dimension (D_H) for that 1D signal (slope of a linear regression) (Higuchi 1988).

Selection of an appropriate scanning direction will depend on the purpose of study as whether it is to measure the FD corresponding to the entire image or cross-section profile of an object of interest on the image. Also It should be noted that, although Higuchi is a 1D method, D_H would be a fraction between 1 and 2 as in this method, the curves are embedded in a plane (Higuchi 1988).

2.6 Unresolved issues

Vessel diameter measurement techniques can be classified into parametric and non-parametric methods. The parametric ones include the curve fitting and profile modelling techniques which rely on a specific parameter (e.g. area under the curve and/or spreading factor of the best fitted Gaussian) to measure the diameter. Non-parametric techniques track and highlight the boundaries at both sides of the vessels using edge detection methods including Edge pixel Grouping (Bhuiyan, Kawasaki et al. 2010) multi-scale segmentation (E. Moghimirad, Seyed Hamid Rezatojighi et al. 2010; Vlachos and Dermatas 2010) extraction of Segment Profiles (Al-Diri, Hunter et al. 2009) and the Graph-based approach (Chapman, Witt et al. 2001) and take the minimum Euclidean distance between the two points on vessel edges as the diameter of that cross-section.

While a number of these techniques have provided a relative accuracy (Al-Diri, Hunter et al. 2009; Xiayu, Niemeijer et al. 2011), asymmetry of the vessels' cross-section profile due to uneven illumination (Zhou, Rzeszotarski et al. 1994), limitations of the imaging equipment and

blurred vessel boundaries can result into incorrect detection of real edge location and therefore imprecise diameter estimation (Xiayu, Niemeijer et al. 2011). These image artefacts may result into reduced correlation of the vessel profile to second order Gaussian curve especially around the residual points and even may fail to converge to the profile shape for edge localization.

Non-parametric tracking methods also require image segmentation and seed point specification prior to initiate the tracking (Bhuiyan, Kawasaki et al. 2010) or can track one edge at a time (Al-Diri, Hunter et al. 2009) which could be problematic when one of the boundaries is blurred or has poor quality. Also majority of the aforementioned techniques do not provide correlated and consistent measurement, which is more important than providing accurate measure, especially for automatic disease assessment in clinical setting (Lowell, Hunter et al. 2004).

2.7 Summary

This chapter has described the anatomy of human eye with focus on retina structure. Manifestation of systemic disease in retina, including diabetes mellitus, cardiovascular disease and stroke as its complication are discussed. Retinopathy signs associated with each disease incidence and their risk factors are explained. A review of the literatures on successful application of retinal image processing is provided, with specific focus on the extracted features and the significance of their relationship with each disease type. This chapter has also covered the techniques for retinal image acquisition and image properties. Using fundus images, the earlier techniques on retinal vessel diameter measurement and fractal dimension calculation as the two most frequent used features by medical section for disease assessment, are reviewed.

Further to the analysis of the current works in the literature, this research study proposes the followings:

- Application of multi-step curve fitting using sum of second order and generalized order Gaussians will provide better fit to a large variety of vessel cross-section profiles in the presence of image artifacts and therefore is a better model for more accurate diameter measurement compared to current models.

- Gray scale vessel profile pixel classification using Linear Discriminant Analysis, is an alternative to profile modeling for diameter measurement which can overcome the problems with image artifacts, profile distortions and asymmetry issue while providing accurate estimation with high success rate. To make it suitable for automatic processing, this method was converted into unsupervised classification scheme by obtaining the training samples for the LDA classifier with an unsupervised procedure which was given the term Unsupervised Linear Discriminant Analysis Method (ULDM).

- Application of Higuchi's fractal dimension on enhanced grayscale vessel profile as time series signal is highly correlated (inverse correlation) and can be used for edge independent identification of diameter variations as disease biomarker. This feature is suitable for automatic image processing in clinical setting when not the actual diameter but only the alteration in diameter is of importance.

This thesis identifies the methodologies to measure retinal vessel diameter at the grayscale level with direct application of cross-section profile (Chapters 3 and 4), proposes an edge independent caliber variation quantification (chapter 5) and its application for 10-year stroke prediction (chapter 6) and diabetes assessment(chapter 7). The effect of retinal vessel pulsations on the new caliber correlated feature is investigated by providing a novel method for visualization of fine microvasculature pulsation using ECG synchronized retinal images (chapter 8).

Chapter 3

Automatic retinal vessel profile modeling and diameter measurement

3.1 Introduction

This chapter will address the problems with accurate profile modeling of a tubular vessel structure and diameter measurement when the overall Gaussian-like shape of the vessel profile is degraded by image artifacts and central light reflex.

This research work has proposed a vessel profile model based on multi-step regression analysis and fitting of a series of additive second-order and generalized Gaussian functions. The advantage of this model is that it provides better representation of vessel profile compared to current state of the art techniques in the presence of aforementioned distortions while providing a parameter for simple and accurate diameter calculation.

In general, profile modeling requires image intensities to be recorded on a cross-sectional line normal to the vessel center line. However, automatic identification of the normal lines requires automatic image selection of the Region of Interest (ROI) and seed point (start point) specification as the main initial steps which have already been addressed in the literatures (Grisan, Pesce et al. 2004). Therefore, this work has assumed that the ROI is known and specified by the grader and the processing is limited to a local region of the retina and not to the entire image. The following sections explain the complete process and validations performed to test its robustness.

3.2 Obtaining vessel cross-section profile

3.2.1 Preprocessing

In the first step an ROI corresponding to a vessel segment was selected and cropped. Only the green channel of the RGB image was used due to providing better vessel to background contrast compared to other channels (Gao, Bharath et al. 2000). The ROI was filtered by second partial derivates of 2D second-order Gaussians along *x* and *y* directions to obtain the Hessian matrix *H(x, y)* corresponding to each Image intensity *I(x, y)* in the coordinates of (x, y) as in (3.1). This method discriminates vessels with tubular structure from the background image and provides local information regarding second-order structures around each pixel.

$$H(x,y)=\begin{bmatrix} f_{xx} & f_{xy} \\ f_{yx} & f_{yy} \end{bmatrix} \tag{3.1}$$

Where:

$$f_{xx}=f_{xx}(x,y)=I(x,y)*\frac{\partial^2}{\partial x^2}(\exp(-(\frac{x^2+y^2}{2\sigma^2})) \tag{3.2}$$

$$f_{yy}=f_{yy}(x,y)=I(x,y)*\frac{\partial^2}{\partial y^2}(\exp(-(\frac{x^2+y^2}{2\sigma^2})) \tag{3.3}$$

$$f_{yx}=f_{xy}=f_{xy}(x,y)=I(x,y)*\frac{\partial}{\partial x\partial y}(\exp(-(\frac{x^2+y^2}{2\sigma^2})) \tag{3.4}$$

and "*" represents the "convolution" operation. In this case, the spreading factor "σ" of the Gaussian kernel was set to 4 in order to match the maximum vessel size inside the selected ROI. The eigenvalues of Hessian matrix (λ_1, λ_2) and their corresponding eigenvectors (v_1, v_2) were calculated in each coordinate (x, y). Assuming $\lambda_1 \geq \lambda_2$, for a coordinate inside the vessel, the orientations of eigenvectors corresponding to small eigenvalues (v_2) show the direction along the vessels, while the orientation of the ones relating to large eigenvalues v_1 present the normal direction. However, for a pixel outside the vessel area this trend is opposite (Xiaofang, Wenwen et al. 2010) providing a good feature for differentiating vessels from non-vessel pixels near the

boundaries as shown in Figure 3.1. Considering the eigenvectors decomposed into x and y directions i.e.

$$\begin{aligned} v_1 &= v_{1x} + v_{1y} \\ v_2 &= v_{2x} + v_{2y} \end{aligned} \tag{3.5}$$

Sum of the two vectors was calculated and the direction of the resultant vector was obtained. The resultant vector v_T would be as in (3.6).

$$v_T = v_{Tx} + v_{Ty} \tag{3.6}$$

Where:

$$\begin{aligned} v_{Tx} &= v_{1x} + v_{2x} \\ v_{Ty} &= v_{1y} + v_{2y} \end{aligned} \tag{3.7}$$

The resultant vector direction was defined as:

$$\theta = \left| \tan^{-1} \frac{v_{Ty}}{v_{Tx}} \right| \tag{3.8}$$

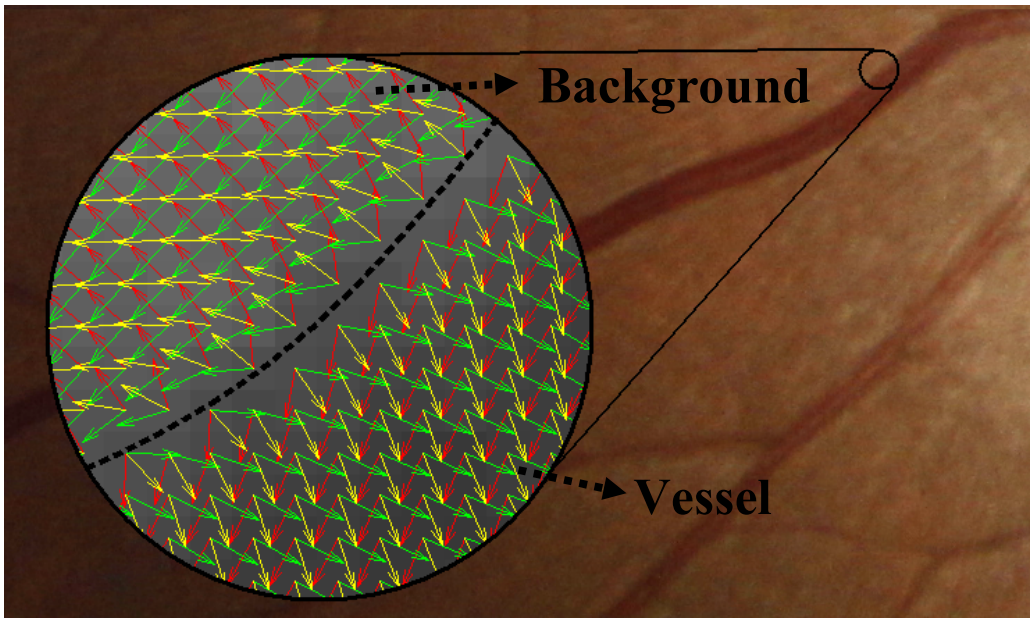

Figure 3.1: Example of vessel segment and eigenvectors of the image Hessian matrix. The resultant eigenvector (Yellow), eigenvectors corresponding to large eigenvalues (Green arrow) and small eigenvalues (Red arrow) at both sides of a vessel segment boundary are shown.

The coordinates between the points corresponding to maximum change in θ were considered as edge locations and used for tracking the vessel boundary.

3.2.2 Tracking vessel boundary

The maximum changes in θ was found by obtaining the magnitude of the gradient vectors at each point as in (3.9)

$$|\nabla\theta| = \sqrt{(\frac{\partial\theta}{\partial x})^2 + (\frac{\partial\theta}{\partial y})^2} \tag{3.9}$$

An example of gradient magnitude image has been illustrated in Figure 3.3.a. Therefore $|\nabla\theta|$ was used to differentiate vessels from non-vessel pixels and locating seed points for the tracking process. A grader was required to select the ROI and specify a point close to vessel segment of interest. This point was considered as the starting point and center of a tracking circle. Radius of the tracking circle was selected smaller than the vessel segment diameter in order not to interfere with the adjacent boundary but pass through the edge closer to its center point. The changes in gradient magnitude were examined on its circumference and the first two points with largest intensity values (large gradient magnitude or sudden change in θ direction) were considered as vessel boundaries. The point closer to the start point was ignored and the other was considered as the centre of subsequent circle for the next iterations. This progressive edge pixel candidate detection continued until the end of ROI. Figure 3.2 shows the simulated tracking procedure using a synthetic gradient magnitude image.

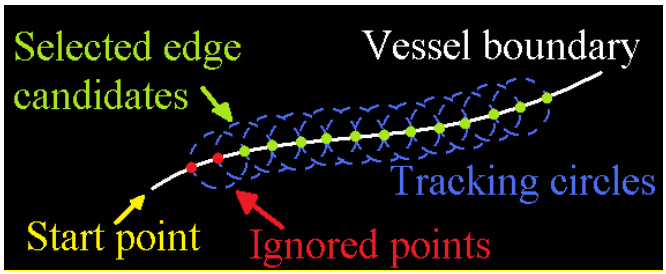

Figure 3.2 Illustration of tracking process on a simulated gradient magnitude image

Due to image artefacts, central light reflex and variation in image contrast in some areas along a vessel boundary (especially for arteries), the maximum intensity change may not be clear. Therefore some conditions and complicated situations were considered in the algorithm to keep track of the vessel boundaries. These condition were based on i) following the location of previous seed points as a guide to find the next one, ii) bilateral filtering (Tomasi and Manduchi 1998; Sable and Jondhale 2010) to smooth the image while preserving the vessel edges for increased contrast at the edges, iii) obtaining overall direction of the vessel as tubular structure using 2D Gabor and Gaussian match filtering when some discontinuities were visible along the tracking path as another guide to find the overall tracking direction. The Gabor filtering was performed over 18 equally spaced angles (10^o) from 0 to 170^o and five different scales (4, 5, 6, 7 and 8) for retinal image enhancement to extract the vascular network, based on the work of (Soares, Leandro et al. 2006). This gave an indication of where the discontinuities existed in order to skip them and not to lose track of the vessel segment. The same approach was taken to detect the second boundary (Figure 3.3.a). Step by step examples of improvements have been shown in Figure 3.4. A linear interpolation was then applied to the detected centre points (edge candidates) to give an initial estimation of vessel boundaries. This estimation was further improved using the ribbon of twins active contour model proposed by Al-Diri et al. (Al-Diri, Hunter et al. 2009). The boundaries were considered as the points where the two ribbons converged (Figure 3.3.b). The vessel centreline was considered as the average between the two tracked edges. Minimum Euclidean distance between the boundaries was picked as the normal line to vessel centreline. Considering the length of this line as an estimation of vessel diameter, the profiles were recorded along the normal line with the length greater than the vessel diameter to include intensities from the background. The tracked boundaries (final interpolation results) and the obtained normal line are depicted in Figure 3.3.b. Block-diagram of the complete vessel tracking process has been shown in Figure 3.5.

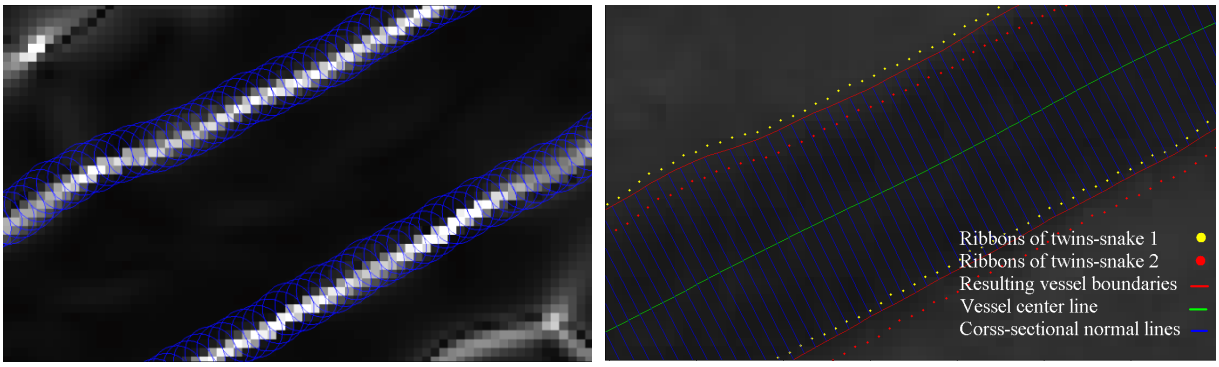

(a) (b)

Figure 3.3 Demonstration of vessel tracking outcome a) Gradient magnitude image and tracking circles b) Implementation of ribbons of twins(Al-Diri, Hunter et al. 2009) (red-yellow dot pairs) and resulting boundary (red), vessel center line (green), cross-sectional normal lines (blue)

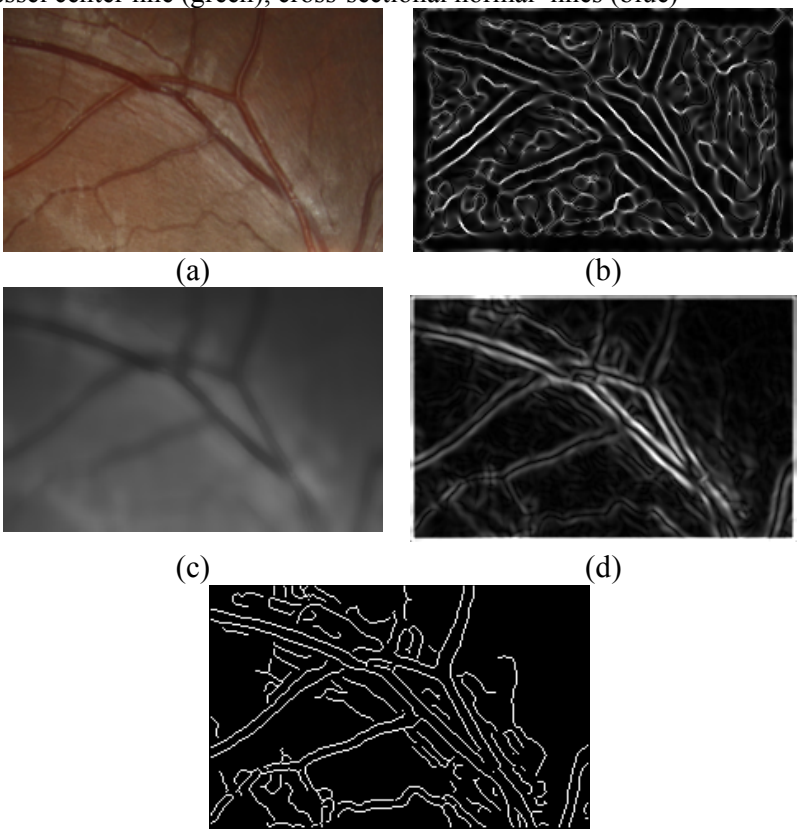

(a) (b)

(c) (d)

(e)

Figure 3.4 Step by Step examples of improvements applied during the tracking process a) RGB image b) Gradient magnitude c) Bilateral + Gaussian filtering d) Gradient magnitude after bilateral and Gaussian filtering e) binarization of the improved gradient magnitude

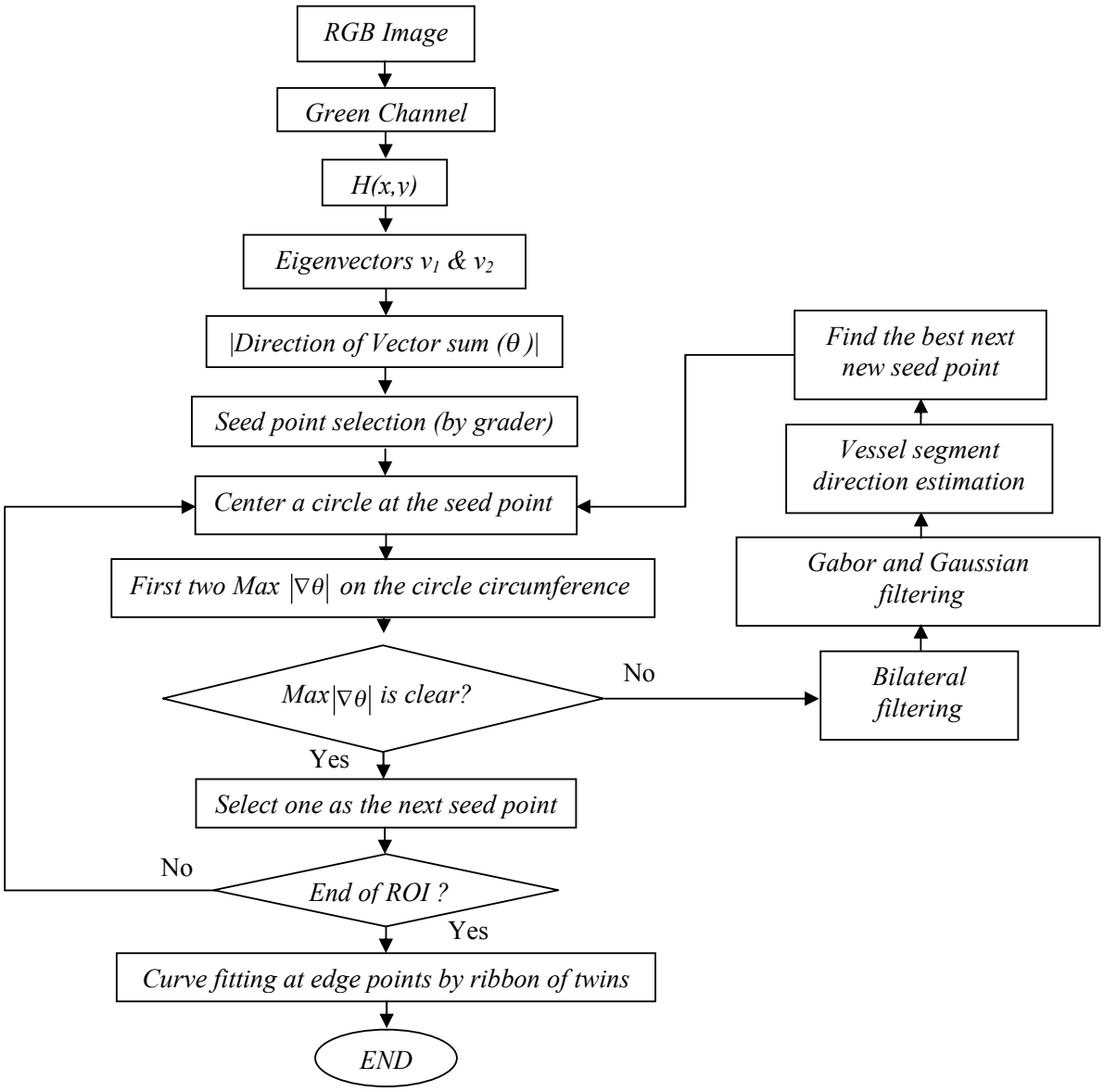

Figure 3.5 Block-diagram of the vessel tracking process

3.3 Vessel profile modeling

Series of second-order Gaussian functions were fitted to each cross-section profile using the non-linear Levenberg-Marquardt method (Levenberg 1944). The proposed model consists of N second-order Gaussian sub-functions plus a DC value, sum of which forms the intensity profile. The optimum value of N was obtained iteratively through minimizing the square fitting error between the modeled and the real profile. However, N was limited to 9 to avoid causing any over fitting problem. This function is expressed as:

$$G(x) = \sum_{i=1}^{N} g_i(x) + p_0 \tag{3.10}$$

where:

$$g_i(x) = p_{(3i-2)} \exp(-0.5(\frac{x - p_{(3i-1)}}{p_{3i}})^2)$$

$p_{(3i-2)}$, $p_{(3i-1)}$ and $p_{(3i)}$ indicate the amplitude, location of the peak and spreading (width distribution) factor of the Gaussian curve respectively. p_0 is a DC value representing the average gray level of the background. All of these parameters were considered as variables and the optimum values were determined by regression analysis. An example of a cross-section profile, its modeled version and a series of fitted Gaussians, have been shown in Figure 3.6. Sum of these curves represent the estimated profile $G(x)$ (dashed line in Figure 3.6.b). In this example the algorithm was converged after N=6 iterations.

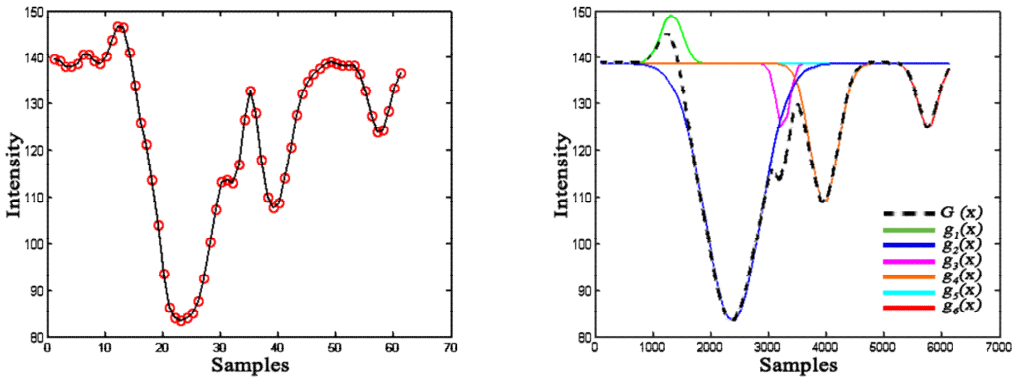

(a) (b)

Figure 3.6: profiling modeling procedure. a) Example of a vessel Cross-section profile with multiple bumps at the centre and periphery fluctuations (red circles). Linearly connected samples for better view and trend estimation (black curve). b) Series of "N" Second-order Gaussians (normal and inverse), sum of which form the complete vessel profile (*G(x)*) (Here *N*=6).

In the next step, vessel boundaries (the area on the modelled profile with sharp intensity transitions) were re-modelled separately by pairs of generalized Gaussian functions. For this purpose and using *G(x)*, a set of critical points were obtained by defining the following classification rules. Local maximum and minimum points on the modeled profile were detected and labeled according to their type (maximum or minimum). Rules were established to group the local extrema and label them as the vessel or background pixels. The maxima were classified into vessel and non-vessel classes based on their location on the profile, local properties of grayscale and gradient magnitude image. On fundus images where the average intensities of the vessels are darker than the background, intensity values of the maxima on the vessel area (corresponding to central light reflex) appear lower than the minima corresponding to the background region. In other words, there exist some maxima with intensity level of less than a number of minimum points. After these maxima were detected, their intensity values were compared to all minimum points. Those with values less than the detected maxima were classified as vessel related minima. Two of these points with largest physical distance on *G(x)* were labeled as critical points B and C. Finally, the first and closest maximum points before and after B and C were named as critical points A and D respectively as shown in Figure 3.7. In case of no central light reflex, the lowest minimum point on the profile was selected as the only required critical point.

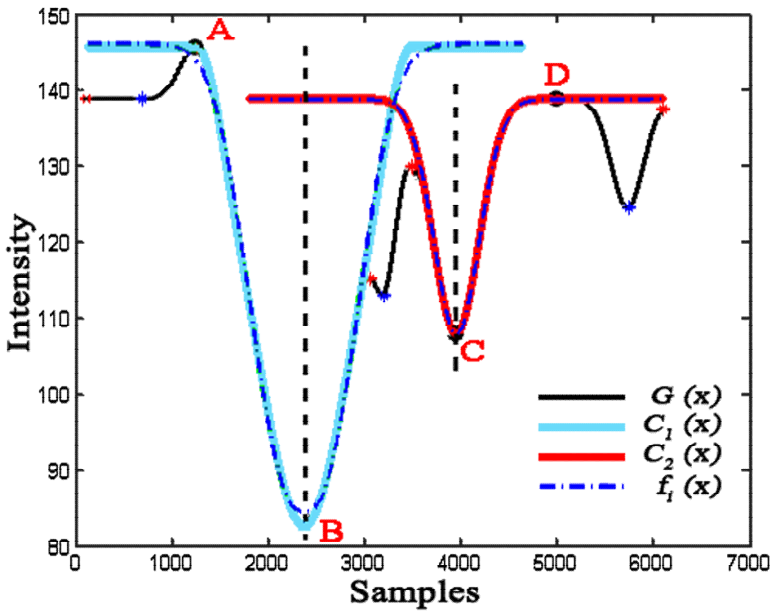

Figure 3.7: Illustration of the critical points, curve cutting (curves C1 and C2) and fitted generalized Gaussians (f_i , i=1,2). The vertical dashed lines are the normal lines against which vessel boundaries were mirrored (Black dashed lines)

After the critical points were detected, a generalized Gaussian function (equation 3.11) was fitted to each segment of *G(x)* corresponding to the vessel edges (intensities between points A to B and C to D) using non-linear Levenberg-Marquardt (Levenberg 1944) method. Prior to the curve fitting process, each segment was mirrored against a normal line passing through its minimum (critical points B or C). This process forms a symmetrical inverse Gaussian-like around point B and C at the vessel boundaries and increases the overall goodness of fit (Figure 3.7). The generalized Gaussians f_1 and f_2 were defines as follow:

$$f_i(x) = -a_i e^{-0.5(\frac{|x-\lambda_i|}{\sigma_i})^{\gamma_i}} + b_i \qquad i = 1,2 \tag{3.11}$$

where a_i, λ_i and σ_i have the same definition as $p_{(3i-2)}$, $p_{(3i-1)}$ and $p_{(3i)}$ as in (3.10). γ_i refers to different symmetric distributions, each having different tail lengths. For the retinal vessel, the

best match usually happens for $2 \le \gamma_i < 3$. b_i is a DC value representing average gray level of the background. As the two generalized Gaussian functions were fitted independently they could have different symmetric distributions with different scaling factors. This provided a generalized representation of edges and allowed accurate representation of the vessel walls with respect to the background for diameter estimation which will be explained in section 3.4. The resulting curves are shown in Figure 3.7.

Using equation 3.10 and 3.11, the complete model *U(x)* was obtained by combining a series of second-order Gaussian functions for the center area (between points B and C) and two generalized Gaussians to represent for the edges. Considering the critical points, B, C, in Figure 3.7, the proposed model was defined as:

$$U(x) = \begin{cases} -a_1 e^{-0.5(\frac{|x-\lambda_1|}{\sigma_1})^{\gamma 1}} + b_1 & x < B \\ \sum_{i=1}^{n} g_i(x) + g_0 & B \le x \le C \\ -a_2 e^{-0.5(\frac{|x-\lambda_2|}{\sigma_2})^{\gamma 2}} + b_2 & x > C \end{cases} \tag{3.12}$$

3.4 Application for diameter measurement

Equation (3.12) provides all the required parameters for estimating the vessel diameter. Therefore the width (*W*) was calculated as:

$$W = \omega_1 + \delta + \omega_2 \tag{3.13}$$

Where based on the definition of vessel diameter by Gang et al. (Gang, Chutatape et al. 2002), ω_1 and ω_2 are half the distance between the points of 50% change on f_1 and f_2 respectively and δ is the horizontal distance between the knee points (minima) of f_1 and f_2 (critical points B and C, $\delta = |B_x - C_x|$) as shown in Figure 3.8. Studies (Gao, Bharath et al. 1997; Gang, Chutatape et al. 2002; Li, Hsu et al. 2003; Huiqi, Hsu et al. 2005) have shown that there is a linear relationship between the speeding factor of a second-order Gaussian and the vessel diameter as discussed in

2.5.1. However, for the generalized Gaussian model in (3.12), the width (ω_1 and ω_2) can be calculated by the following equation:

$$\omega_i = \frac{1}{2}\alpha_i\sigma_i \quad i = 1,2 \tag{3.14}$$

Where:

$$\alpha_i = 2\,|\sqrt[\gamma_i]{2\ln(0.5)}\,| \tag{3.15}$$

α_i is the scaling factor to provide a linear relationship between ω_i and σ_i (spreading factor) of the generalized Gaussians. Using this method, one α was calculated for each σ in order to suit different blurriness levels at vessel boundaries. According to (3.15), setting $\gamma_i = 2$ gives $\alpha_i = 2.33$ as proposed by (Li, Hsu et al. 2003), (Gao, Bharath et al. 2000) and (Lowell, Hunter et al. 2004) for diameter measurement using the basic second order Gaussian model.

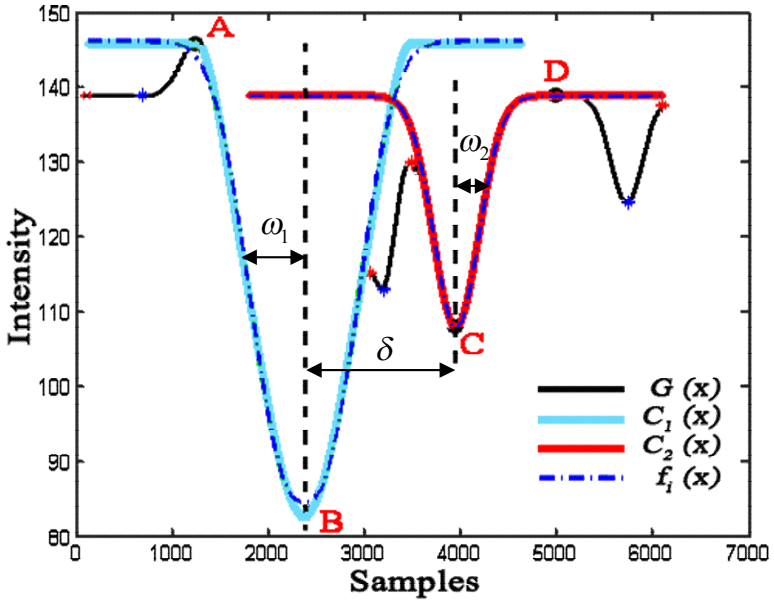

Figure 3.8 Application of the proposed model for diameter measurement

3.5 Validation

Two sets of validations were performed to test the effectiveness of the proposed model, 1) evaluation of the curve fitting performance 2) diameter measurement accuracy and precision test.

3.5.1 Curve fitting performance

The curve fitting evaluation was performed in two steps. At first the average squared fitting error *e* was calculated to measure the agreement between the vessel profile and sum of second-order Gaussians $G(x)$ as follow:

$$e = \frac{1}{n}\sum_{i=1}^{n}(y_i - G(x_i))^2 \tag{3.16}$$

Where n and y_i are the number of samples and the intensity values of the original profile respectively. $G(x_i)$ is the proposed series as described by equation (3.10). The result was compared against the state of the art models based on difference of two second-order Gaussians (Gao, Bharath et al. 2000; Li, Hsu et al. 2003; Lowell, Hunter et al. 2004). Further test was performed to assess the agreement between the generalized Gaussian model (f_1 and f_2) as in (3.11) and the modeled profile ($G(x)$)on the overlapping sections by measuring the mean squared fitting error for each generalized Gaussian model separately (Blue (C_1) and Red (C_2) curves in Figure. 3.8).

3.5.2 Diameter measurement accuracy

Diameter of the cross-sections were measured and compared with manual measurements from three observers and established automatic techniques including the 1D Gaussian (Zhou, Rzeszotarski et al. 1994) 2D Gaussian (Lowell, Hunter et al. 2004) ESP (Al-Diri, Hunter et al. 2009) and Graph based method (Xiayu, Niemeijer et al. 2011). *Precision* and *Accuracy* of the techniques were calculated and compared whose definitions were adopted from (Lowell, Hunter et al. 2004) as in equations (3.17) and (3.18) respectively. *Precision* is defined as the standard

deviation of the difference between a reference diameter and the evaluating methods. Similarly, the *Accuracy* is the average (mean) of the difference between the reference diameter and the method under the test. Therefore, the lower values indicate the more precise and accurate technique. The reference diameter was selected as the average of the values reported by the three observers. Precision and accuracy of the each observer (O_1, O_2 and O_3) was also calculated with respect to the reference value and presented for comparison purpose.

$$precision = SD(x_i - x_{ref}) \tag{3.17}$$

$$accuracy = Mean(x_i - x_{ref}) \tag{3.18}$$

where x_{ref} is the reference diameter and x_i, $i = 1,2,..,5$ is the diameter obtained by method i.

3.5.3 Materials

At first to evaluate the fitting performance, the proposed model (equations 3.10 and 3.11) was tested against 350 different profiles of 175 arteries and 175 veins among 9 fundus images (each 3072×2048 pixels) captured with the Cannon D-60 digital fundus camera. All the cross sections were provided by an approved grader from the center for eye research, Eye and Ear Hospital, Melbourne-Australia (CERA). The profiles were selected among a wide range of properties including large and small vessels, central light reflex, noise, uneven illuminations and asymmetries with respect to the centerline.

The expert annotated publically available REVIEW dataset was used to validate the model for diameter measurement as it is well accepted as ground truth by other literatures (Al-Diri, Hunter et al. 2008; Xiayu, Niemeijer et al. 2011). It contains four sub-sets of mixed quality retina images with total number of 5066 vessel diameters from 193 segments measured manually by three independent observers. The details of these four sub-sets are summarized as follow:

1) The kick-point image set (KPIS) consists of two good quality retina images (288×119 and 170×192 pixels) with 3 segments and 164 measured cross-sections. The edges were determined

based on the kick-points which are normally present in vessel profiles of highly focused retina images.

2) The high resolution image set (HRIS) with different severity of diabetic retinopathies. It contains some abnormalities near the vessel edges which provide a challenge for automatic diameter measurement. It contains four sub-images (3584×2438 pixels each) and 90 segments with 2368 manually annotated cross-sections.

3) The central light reflex image set (CLRIS) represents extensive vascular light reflex which appears as a small Gaussian in the middle of the vessel profile.CLRIS consists of two retinal images (2160×1440 pixels each) with total number of 21 segments and 285 cross-sections.

4) The vascular disease image set (VDIS) includes eight noisy retina images (1360×1024 pixels each), six of which suffer from diabetic retinopathy. It consists of the total number of 79 segments and 2249 measured profiles. The VDIS dataset provides a greater challenge to the diameter measurement due to its inherent variations.

Details of the validation database and disease classification level of each image have been summarized in Table 3.1 according to Al-Diri et.al (Al-Diri, Hunter et al. 2008).

Table 3.1 Summarized details of the validation dataset (REVIEW image set)

Image set	Image Number	Dimension (pixels)	Number of Cross-sections	Disease Level (grading)
KPIS	001	288×119	111	Normal
	002	170×192	53	
HRIS	001	3584×2438	1215	Level 3 , Severe Non-Proliferative Retinopathy
	002		452	Level 2, Moderate Non-Proliferative Retinopathy
	003		596	Level 3, Severe Non-Proliferative Retinopathy
	004		105	Level 1, Minimal Non-Proliferative Retinopathy
CLRIS	001	2160×1440	32	Normal
	002		253	
VDIS	001	1360×1024	291	Arteriosclerotic, Arterio-Vascular Changes
	002		308	Level 5, Proliferative Retinopathy
	003		270	Level 1, Minimal Non-Proliferative Retinopathy
	004		237	Level 1, Minimal Non-Proliferative Retinopathy
	005		202	Level 2, Moderate Non-Proliferative Retinopathy
	006		296	Normal
	007		254	Normal
	008		391	Level 3, Severe Non-Proliferative Retinopathy

3.6 Results

3.6.1 Profile modeling

A comparative evaluation of the proposed model in (3.10) has been provided in Table 3.2. Among total number of 350 profiles, the series of second-order Gaussian model (*G(x)*) resulted in 100% fitting success rate and average squared fitting error of 0.720 with standard deviation of 0.584. However the average fitting error for the piecewise model was 6.367 with standard deviation and success rate of 4.331 and 70% respectively showing that the piecewise model is unable to describe some vessel profiles.

Table 3.2 Comparison between the proposed series of second-order Gaussian and the Piecewise Gaussian model in terms of fitting performance

	Series of 2nd Order Gaussians (*G(x)*)	**2D Model** (Lowell, Hunter et al. 2004)	**Difference of Gaussians** (Gao, Bharath et al. 2000; Li, Hsu et al. 2003)
Total No. of profiles	350	350	350
No. of successful fits	350	320	248
Success rate (%)	100%	91.42%	70.85%
Mean squared fitting error (*e*) ± SD	0.720±0.584	2.247±1.032	5.367±4.331

Table 3.3 demonstrates the average squared fitting error and standard deviation of the 350 generalized Gaussian functions (*f(x)* as in (3.11) fitted to the vessel boundaries. The result show generalized Gaussian model fits perfectly to the sharp-transition areas of the vessel profile corresponding to edge locations with mean squared error and standard deviation of 0.060 and 0.027 respectively.

Table 3.3 Average Squared fitting error and standard deviation as a measure of the agreement between the generalized Gaussian model and the fitted profile at vessel boundaries.

	Generalized Gaussian (*f(x)*)
Total No. of profiles	350
Mean squared fitting error (e)±SD	0.060±0.027

3.6.2 Diameter measurement

Tables 3.4 to 3.7 compare the *accuracy* and *precision* of different techniques based on the definition provided by (3.17) and (3.18). The proposed method had the highest accuracy on HRIS and KPIS and best precision on the vessels with some kick-points present on their cross-section profile (KPIS subset). This model had also the second highest accuracy (lowest value) on the HRIS subset (high resolution images), after the 2D Gaussian with only 0.01 difference in the absolute value. However, the 2D Gaussian showed much lower precision (large value) compared to the proposed model. In terms of both accuracy and precision the proposed model performed the second best after ESP on VDIS. CLRIS was found the most challenging dataset with overall low precision across all measurement method. The result indicates while a technique may perform better on a subset with specific properties and certain image artifacts, it may not be suitable for application on other images with different properties.

Table 3.4 Comparison of vessel diameter measurement accuracy and precision between the proposed Multi-step Gaussian regression method, established techniques and manual measurement for the HRIS database

HRIS Database					
Method name	Success Rate (%)	**Diameter**		**Difference**	
		Average μ_1	SD σ_1	Average (Accuracy) μ_2	SD (Precision) σ_2
Observer 1	100	4.12	1.25	-0.23	0.288
Observer2	100	4.35	1.35	0.002	0.256
Observer3	100	4.58	1.26	0.23	0.285
FWHM	88.3	4.97	-	0.62	0.926
1D Gaussian	99.6	3.81	-	-0.54	4.137
2D Gaussian	98.9	4.18	-	-0.17	6.019
ESP Method	99.7	4.63	-	0.28	0.42
Graph Based Method	100	4.56	1.30	0.21	0.567
Proposed Multi-step Method	**99.1**	**4.42**	**1.37**	**0.18**	**0.6**

Table 3.5 Comparison of vessel diameter measurement accuracy and precision between the proposed Multi-step Gaussian regression method, established techniques and manual measurement for the CLRIS database

CLRIS Database					
Method name	Success Rate (%)	**Diameter**		**Difference**	
		Average μ_1	SD σ_1	Average (Accuracy) μ_2	SD (Precision) σ_2
Observer 1	100	13.19	4.01	-0.61	0.566
Observer2	100	13.69	4.22	-0.11	0.698
Observer3	100	14.52	4.26	0.72	0.566
FWHM	0	-	-	-	-
1D Gaussian	98.6	6.3	-	-7.5	4.137
2D Gaussian	26.27	7.0	-	-6.8	6.019
ESP Method	93.0	15.7	-	-1.90	1.469
Graph Based Method	94.1	14.05	4.47	0.08	1.78
Proposed Multi-step Method	**97.9**	**13.41**	**4.31**	**-0.91**	**1.8**

Table 3.6 Comparison of vessel diameter measurement accuracy and precision between the proposed Multi-step Gaussian regression method, established techniques and manual measurement for the VDIS database

VDIS Database					
Method name	Success Rate (%)	**Diameter**		**Difference**	
		Average μ_1	SD σ_1	Average (Accuracy) μ_2	SD (Precision) σ_2
Observer 1	100	8.50	2.54	-0.35	0.543
Observer2	100	8.91	2.69	0.06	0.621
Observer3	100	9.15	2.67	0.30	0.669
FWHM	78.4	7.94	-	-0.91	0.879
1D Gaussian	99.9	5.78	-	-3.07	2.110
2D Gaussian	77.2	6.59	-	-2.26	1.328
ESP Method	99.6	8.80	-	-0.05	0.766
Graph Based Method	96.0	8.35	3.00	-0.53	1.43
Proposed Multi-step Method	**98.1**	**8.53**	**2.87**	**-0.23**	**1.32**

Table 3.7 Comparison of vessel diameter measurement accuracy and precision between the proposed Multi-step Gaussian regression method, established techniques and manual measurement for the KPIS database

KPIS Database					
Method name	Success Rate (%)	**Diameter**		**Difference**	
		Average μ_1	SD σ_1	Average (Accuracy) μ_2	SD (Precision) σ_2
Observer 1	100	7.97	0.47	0.45	0.234
Observer2	100	7.60	0.42	0.08	0.213
Observer3	100	7.00	0.52	-0.52	0.233
FWHM	96.3	6.47	-	-1.05	0.389
1D Gaussian	100	4.95	-	-2.57	0.399
2D Gaussian	100	5.87	-	-1.65	0.337
ESP Method	100	6.56	-	-0.96	0.328
Graph Based Method	99.4	6.38	0.59	-1.14	0.67
Proposed Multi-step Method	**99.2**	**6.98**	**0.43**	**-0.63**	**0.3**

3.7 Summary

This chapter addressed the problem of retinal vessel cross-section profile modeling and diameter measurement in the presence of image artifacts, including different blurriness levels at vessel boundaries and uneven illuminations. A novel multi-step regression technique was introduced

and validated for retinal vessel profile modeling and diameter measurement based on sum of a series of Gaussian functions. In the first step, a series of second order Gaussians were fitted to the vessel cross-section profiles sum of which formed the profile shape. In the second step, the vessel boundaries were fitted with higher order Gaussians to match different blurriness levels at the boundaries. The optimum number of second-order Gaussians in step 1 and the order of generalized Gaussians (higher order) in the second stage were obtained automatically together with other parameters including amplitude, location of the peak spreading factor (width distribution) and the DC level, using Levenberg-Marquardt (Levenberg 1944) technique.

The advantage of this model is that unlike other profile modeling techniques (ie. 1D , 2D and twin Gaussian models) which use single sigma parameter (spreading factor) of a fitted Gaussian to estimate the diameter, the proposed model provides two different sigma values corresponding to different blurriness levels at different vessel edges. In other words, it does not rely on a fixed value for the scaling factor of the Gaussian function to use it for all databases which may have dissimilar blurriness levels and illuminations. The performance of the proposed model was validated on the RIVEW dataset in a comparative evaluation.

The proposed method showed the highest accuracy on HRIS and KPIS and precision on the vessels with some kick-points artifacts on their profile. The accuracy of the proposed model was the second highest (lowest value) for the high resolution images, after the 2D Gaussian However, the 2D Gaussian showed much lower precision (large value) compared to this model. Overall, this model shows improvements to vessel profile modeling and caliber measurement challenges.

Chapter 4

Automatic vessel edge localization and diameter measurement

4.1 Introduction

This chapter introduces a novel technique for automatic vessel edge localization using vessel cross-section intensity profile based on pixel classification using Linear Discriminant Analysis (LDA). As LDA by default is a supervised classifier, this chapter proposes a technique for unsupervised training of the LDA and introduces an unsupervised LDA method (ULDM) for retinal vessel diameter measurement base on direct used of cross-section profile. This technique does not require profile modeling and addresses the limitations of other techniques in the presence of edges with sharp transitions and kick-points present on the cross-section profile. The outcome of this work validates the hypothesis of diameter measurement accuracy being database dependant and subjective to a specific image artifact.

4.2 Initialization and ROI selection

The algorithm was initiated with the ROI specification, localization of vessel cross sections and recording of the intensity profiles. The vessel boundaries were tracked using the vector sum of the image Hessian eigenvectors on the circles centered at vessel edges as explained in section 3.2. The pixel intensities were recorded on a line normal to the vessel centreline with the length of 10% greater than the shortest Euclidean distance between the edge vessel points marked in the tracking (boundary estimation) process (chapter 3). This was to ensure incorporating of the background intensities corresponding to both sides of the vessel trunk into the vessel profile while not overlapping the pixels corresponding to the adjacent vessels. However, for fine vessels with diameters equal to or less than 1 pixel where the centerline could not be estimated from the edges, the normal line was obtained with respect to the tracking direction as in (Xiaofang,

Wenwen et al. 2010). This initialization step was only used for cross-section profile recording. However, this is not suitable for measuring the diameter as tracking methods are sensitive to image artifacts Only the green channel was used as it provided better contrast between the vessels and the background (Li, Hsu et al. 2003).

4.3 Linear Discriminant Analysis (LDA) classifier

Linear discriminant analysis is a method for data classification and dimensionality reduction (Wijaya, Uchimura et al. 2011). It optimizes class separability by maximizing the ratio of interclass to intra-class variances and is suitable for applications with unequal sample sizes. Assuming a dataset containing total number of L classes and N_C samples in each class, based on the Fisher's equation (4.1), the optimum projection matrix W can be obtained by maximizing equation (4.1):

$$J(W) = \frac{W^T S_b W}{W^T S_w W} \tag{4.1}$$

where S_b and S_w are the inter-class and intra-class scatter matrices respectively. The scatter matrices are defined as:

$$S_b = \sum_{C=1}^{L} N_C (\mu_C - \overline{X})(\mu_C - \overline{X})^T \tag{4.2}$$

$$S_W = \sum_{C=1}^{L} \sum_{i=1}^{N_C} (x_i^C - \mu_C)(x_i^C - \mu_C)^T \tag{4.3}$$

where $\mu_C = \frac{1}{N_C} \sum_{i=1}^{N_C} x_i^C$, $\overline{X} = \frac{1}{N} \sum_{C} N_C \mu_C$ and T stands for the "transpose" matrix.

Equation (4.1) can also be defined by the covariance matrix with no effect on the solution, as the covariance matrix is constantly proportional to the scatter matrix.

The next step is to automatically generate the training data using the Linear Discriminant Analysis (LDA) classifier which is trained to separate the profile into the three clusters; 1st

corresponding to the vessel surface and the 2nd and 3rd corresponding to the background at either side of the vessel trunk.

4.3.1 Automatic training of the LDA classifier

LDA is a supervised technique, and the training process needs to be done automatically so that the system is suitable for unsupervised and automatic vessel edge localization and diameter measurement. This was performed using a novel cluster analysis, based on the sharp transitions on vessel profile corresponding to the edges (Zhou, Rzeszotarski et al. 1994; Gao, Bharath et al. 2000; Lowell, Hunter et al. 2004). However, as discussed earlier, image artifacts distort the axial symmetry, shape and smoothness of the vessel profiles compared to inverse Gaussian curve as the general profile model (Zhou, Rzeszotarski et al. 1994). As shown in chapter 3, deliberate inclusion of some pixel intensities corresponding to the background region into the vessel profile will provide better representation of its actual form for the purpose of curve fitting and edge detection. The distortions appear as a number of extrema points on the profile mainly corresponding to the background region. These points were used as critical points for cluster analysis to obtain the LDA training classes. In order to perform cluster analysis, the differential of the profile was computed. In the differential of the profile plot, the zero-crossing points corresponding to the location of the extrema were obtained to find three critical points as the reference to initiate cluster analysis. According to the Gaussian model of vessel profile (Zhou, Rzeszotarski et al. 1994; Lowell, Hunter et al. 2004), it is confirmed that generally the edge points have high intensity values while the points on the surface of the vessels contain lower intensities except for the central light reflex area. Therefore, location of the lowest minima in intensity which correspond to the vessel region was marked as the first required critical point. The two highest maxima at both side of this point were labeled as the two other points each correspond to one background region at left and right side of the vessel. Given the three points guaranteed the existence of a circle to pass through them by joining the vertices in pairs (creating chords) and forming a triangle; as the perpendicular bisectors of the chords always pass through the centre of a circle which includes those vertices. This automatically obtained bounding circle was used as the basis for cluster analysis and unsupervised classification of the local extermums

to train the LDA. An example of a vessel cross-section profile with central light reflex (CLR) has been shown in Figure 4.1. From the centre of this circle a radial line was connected to each point. Starting from 0 degree and rotating anti-clockwise, all the angles (θ_1, θ_2, ... , θ_n) between the two consecutive radial lines were obtained sequentially and sorted from the largest to the smallest value. The first three largest angles corresponding to the largest arcs on the circle considered as the boundaries separating the three training classes (e.g. θ_4, θ_9 and θ_{12} in Figure 4.1). All the extrema that fell within the same section between the two boundary-arcs were categorized as the same class. Group 1 and 3 were considered as the maxima and minima relating to the background at either side of the vessel and group 2 to the extermums corresponding to the trunk as shown by asterisks in a unique colour (Figure 4.1). In order to increase the number of training samples for more accurate cluster analysis, all the points on the vessel profile within the distance between the two horizontally farthest extermums of each class were considered as the member of that class and used as training samples.

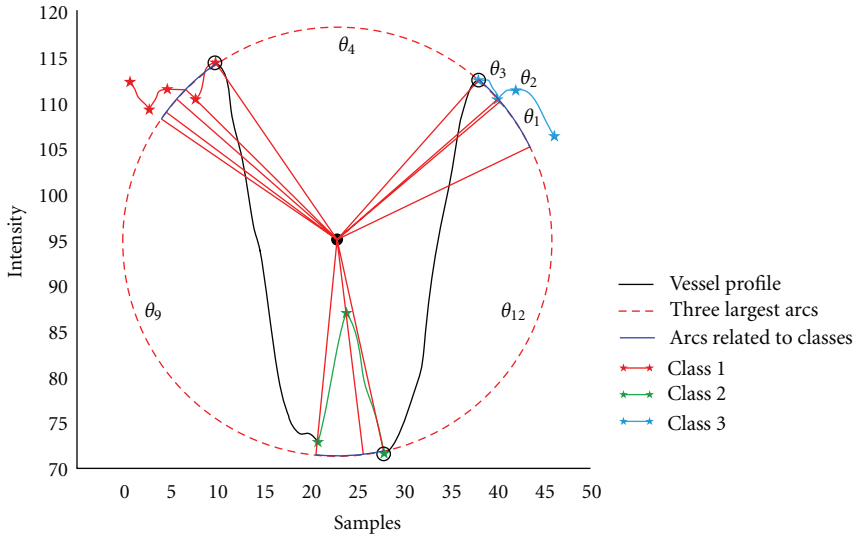

Figure 4.1 Obtaining the training classes for a sample vessel profile (CLRIS, image No. 1, cross-section No. 22). The extermums related to the three classes are shown with asterisks in Red, Green, and Blue. Blue curves are the regions related to the detected classes. θ_4, θ_9, and θ_{12} represent the first three largest angles.

4.3.2 Edge localization and diameter measurement

A generalization of the Fisher's LDA (1936) was applied to the intensities of retinal vessel cross section profiles after the mean value was subtracted, in order to classify them into three major

regions based on their physical location on the intensity profile (vessel or background). The decision boundaries were used to highlight the midpoints between the maximum and minimum intensities corresponding to the vessel edges and measure the diameter based on the definition of 50% intensity change, according to L. Gang et al. (Gang, Chutatape et al. 2002). Let the matrix $X = [X^1, X^2, X^3]$ denote the 2D training data (intensities Vs samples) where X^C, *(C=1, 2, 3)* represent the vector set belonging to the class *C* obtained in section 4.4.1. Considering as the matrices of size *2×1* representing for the class sample means, the pooled estimate of the corresponding *2×2* sample scatter matrices was calculated according to (Seber 1984), as follow:

$$S_{p_{2\times 2}} = \frac{\sum_{C=1}^{3}(N_C - 1)S_C}{\sum_{C=1}^{3}(N_C - 1)} \tag{4.4}$$

where $S_C = \sum_{i=1}^{N_C}(x_i^C - \overline{X}_C)(x_i^C - \overline{X}_C)^T/(N_C - 1), \quad (C = 1,2,3)$, is the sample scatter matrix of size *2×2*. N_C is the number of samples available in each dimension of the class *C*.

Equation (4.4) is valid due to the robustness of linear discriminant function (LDF) to unequal scatter matrices and the assumption of similarity existence between the three sample scatter matrices (Seber 1984). The resulting three discriminant functions were calculated, as in (4.5)

$$L_C(x) = \log\pi_C - \frac{1}{2}X_C^T S_p^{-1} X_C + \overline{X}_C^T S_p^{-1} x, \quad (C = 1,2,3) \tag{4.5}$$

where $\pi_1 = \pi_2 = \pi_3 = \frac{1}{3}$ were defined as the prior probabilities of each training group while ignoring the class proportions.

In order to measure the diameter, the intensity Vs sample plane of the vessel profile was padded with training points and classified according to the largest value of $L_C(x) - \log\pi_C$ as the decision rule The decision boundaries D_{ij}, *(i,j)∈[(1,2),(2,3),(1,3)]* corresponding to three classes were obtained using (4.6).

$$D_{ij}(x) = L_i(x) - L_j(x) \tag{4.6}$$

The horizontal distance between the two points where the decision boundaries crossed the vessel profile was considered as the vessel diameter as shown in Figure 4.2.

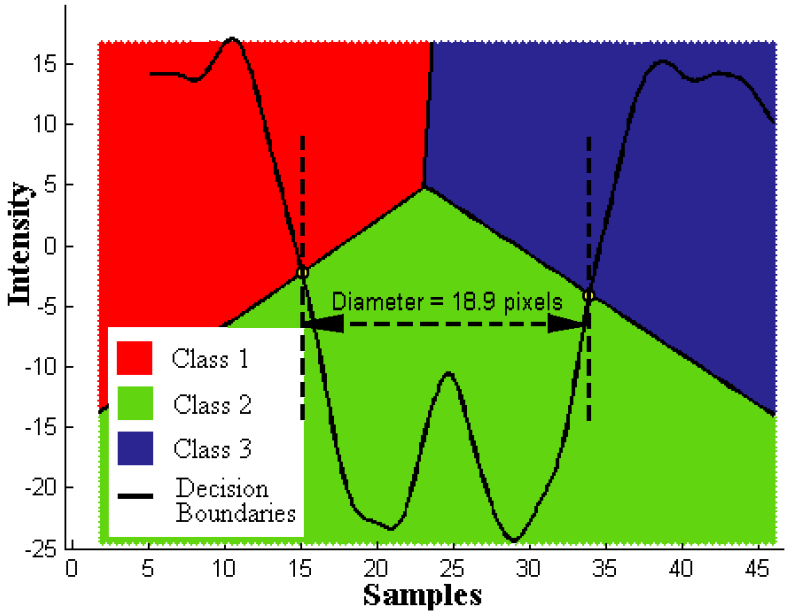

Figure 4.2 Example of ULDM output showing a vessel cross-section profile (CLRIS, image no. 1, cross section no. 22) with classified padded intensity values and the decision boundaries between the classes. The horizontal distance between the two points where the decision boundaries cross the vessel edges (approximately at 50% intensity change) was considered as the diameter (18.9 pixels in this example).

4.4 Validation

The proposed method (ULDM) was compared with the FWHM, 1D and 2D Gaussian models, ESP, and the graph based on comparison method as provided in (Xiayu, Niemeijer et al. 2011). The REVIEW database was used as ground truth to validate the technique. The details of this database were discussed in section 3.5.3. Following the result evaluation and presentation method used in (Xiayu, Niemeijer et al. 2011) the average, μ_1, and standard deviation (SD), σ_1, of the estimated diameters were calculated in pixels for each single database and presented together with the reported values from other methodologies. The signed μ_2 (Accuracy) and corresponding

σ_2 (Precision) were also defined as the average and SD of point by point difference between the measured and the reference diameter as defined by equations 3.17 and 3.18. The reference was considered as the average of the three diameter values measured by the three observers.

For performance and efficiency estimation, the success rate was first calculated as the ratio of the number of measureable cross-sections to the total number of available profiles in the database reported by observers. The higher success rate and lower deviation from the reference diameter (lower μ_2 and σ_2) indicate more precise estimation. Measure of similarity between the ULDM, the three manual and reference diameter (average of three observers) was also obtained by cross-correlation as further analysis.

4.5 Results

Receivers Operating Characteristic (ROC) analysis was used to calculate the area under the curve (AUC), sensitivity, specificity corresponding to the ULDM classifier performance for correct edge localization, as shown in Figure 4.3. The result indicate the best performance with AUC=0.936 (p<0.0001, 95% CI [0.931 to 0.941]) and specificity=86.6, and sensitivity of 82.9.

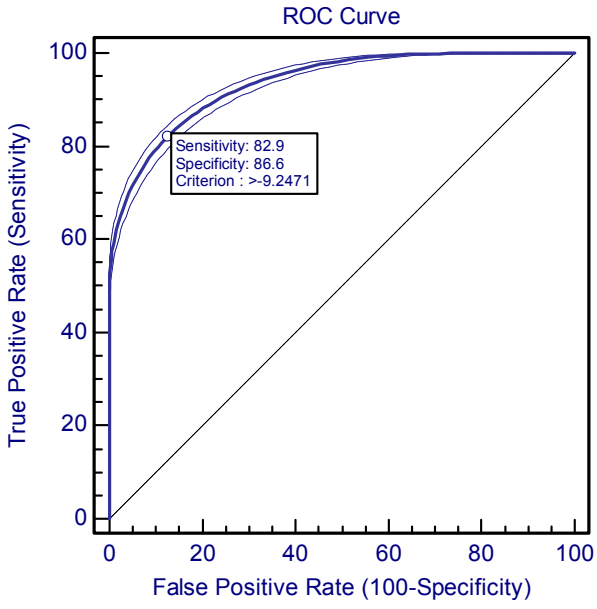

Figure 4.3 ULDM performance evaluation (ROC curve)

Tables 4.1 to 4.4 give the comparison of the accuracy and precision between the three manual measurements (observer 1, 2 and 3), the FWHM (Brinchmann-Hansen and Heier 1986), 1D Gaussian (Zhou, Rzeszotarski et al. 1994), 2D Gaussian (Lowell, Hunter et al. 2004), ESP (Al-Diri, Hunter et al. 2009), graph based (Xiayu, Niemeijer et al. 2011) and the proposed ULDM technique. The four tables compare the four sub-datasets of the REVIEW database. The Tables 4.1 to 4.4 correspond to the HRIS, CLRIS, VDIS and KPIS datasets respectively. The reporting format in these tables is the same as the one used by previous studies (Al-Diri, Hunter et al. 2009; Xiayu, Niemeijer et al. 2011), with the addition of row corresponding to the proposed technique, ULDM.

The second column of these four tables presents the success rate in percent corresponding to each measurement method as defined earlier. It is observed that ULDM has a high success rate similar to other five computerized diameter measurement techniques; FWHM, 1D Gaussian, 2D Gaussian, ESP and Graph based. The Average value of the estimated vessel widths μ_1 together with the standard deviation, σ_1 from the mean is provided in columns three and four respectively.

Columns 5 and 6 are the indicator of the signed average (μ_2) and SD (σ_2) of the difference between the measured diameter and the gold-standard diameter obtained by averaging the three manual measurements respectively. From these columns, it is observed that different techniques have the least difference from the gold standard for the different datasets. While 2D Gaussian has the smallest μ_2 for HRIS dataset, Graph based method has the smallest μ_2 for CLRIS dataset, ESP has the smallest μ_2 for VDIS dataset and ULDM has the smallest μ_2 for KPIS dataset. From these tables, it is observed that while other techniques are more suited for one dataset, ULDM is more consistent, and has the smallest or second smallest error for all the datasets.

Table 4.1 Comparison of vessel diameter measurement accuracy and precision between the proposed ULDM, established techniques and manual measurement for the HRIS database

HRIS Database					
Method name	Success Rate (%)	**Diameter**		**Difference**	
		Average μ_1	SD σ_1	Average (Accuracy) μ_2	SD (Precision) σ_2
Observer 1	100	4.12	1.25	-0.23	0.288
Observer2	100	4.35	1.35	0.002	0.256
Observer3	100	4.58	1.26	0.23	0.285
FWHM	88.3	4.97	-	0.62	0.926
1D Gaussian	99.6	3.81	-	-0.54	4.137
2D Gaussian	98.9	4.18	-	-0.17	6.019
ESP Method	99.7	4.63	-	0.28	0.42
Graph Based Method	100	4.56	1.30	0.21	0.567
Proposed ULDM Method	**99.6**	**4.19**	**1.35**	**0.21**	**0.79**

Table 4.2 Comparison of vessel diameter measurement accuracy and precision between the proposed ULDM, established techniques and manual measurement for the CLRIS database

CLRIS Database					
Method name	Success Rate (%)	**Diameter**		**Difference**	
		Average μ_1	SD σ_1	Average (Accuracy) μ_2	SD (Precision) σ_2
Observer 1	100	13.19	4.01	-0.61	0.566
Observer2	100	13.69	4.22	-0.11	0.698
Observer3	100	14.52	4.26	0.72	0.566
FWHM	0	-	-	-	-
1D Gaussian	98.6	6.3	-	-7.5	4.137
2D Gaussian	26.27	7.0	-	-6.8	6.019
ESP Method	93.0	15.7	-	-1.90	1.469
Graph Based Method	94.1	14.05	4.47	0.08	1.78
Proposed ULDM Method	**98.2**	**13.23**	**3.55**	**-0.55**	**1.79**

Table 4.3 Comparison of vessel diameter measurement accuracy and precision between the proposed ULDM, established techniques and manual measurement for the VDIS database

VDIS Database					
Method name	Success Rate (%)	**Diameter**		**Difference**	
		Average μ_1	SD σ_1	Average (Accuracy) μ_2	SD (Precision) σ_2
Observer 1	100	8.50	2.54	-0.35	0.543
Observer2	100	8.91	2.69	0.06	0.621
Observer3	100	9.15	2.67	0.30	0.669
FWHM	78.4	7.94	-	-0.91	0.879
1D Gaussian	99.9	5.78	-	-3.07	2.110
2D Gaussian	77.2	6.59	-	-2.26	1.328
ESP Method	99.6	8.80	-	-0.05	0.766
Graph Based Method	96.0	8.35	3.00	-0.53	1.43
Proposed ULDM Method	**96.3**	**8.68**	**2.82**	**-0.64**	**1.18**

Table 4.4 Comparison of vessel diameter measurement accuracy and precision between the proposed ULDM, established techniques and manual measurement for the KPIS database

KPIS Database					
Method name	Success Rate (%)	**Diameter**		**Difference**	
		Average μ_1	SD σ_1	Average (Accuracy) μ_2	SD (Precision) σ_2
Observer 1	100	7.97	0.47	0.45	0.234
Observer2	100	7.60	0.42	0.08	0.213
Observer3	100	7.00	0.52	-0.52	0.233
FWHM	96.3	6.47	-	-1.05	0.389
1D Gaussian	100	4.95	-	-2.57	0.399
2D Gaussian	100	5.87	-	-1.65	0.337
ESP Method	100	6.56	-	-0.96	0.328
Graph Based Method	99.4	6.38	0.59	-1.14	0.67
Proposed ULDM Method	**100**	**7.02**	**0.67**	**-0.50**	**0.60**

While the measure of the accuracy has been reported in terms of average diameter difference (Al-Diri, Hunter et al. 2009; Xiayu, Niemeijer et al. 2011), this does not provide a precise measure of agreement with the ground truth. Therefore cross-correlation analysis was performed for further investigation as in Table 4.5. In this table, the columns 2, 3 and 4 correspond to the correlation between the three manual measurements, the fifth is the average of the three manual measurements labeled as Obs_avg and column 6 is that of the ULDM. This was repeated for

each of the four subset images. The correlation matrix being symmetrical, only the lower half is reported. As expected, the diagonal elements are unity. From this table it is observed that for HRIS, VDIS and CLRIS the correlation between ULDM and the Obs_avg (bench mark) is high, close to the correlation between the three manual measurements and Obs_avg (range = [0.87, 0.91]). The KPIS shows the lowest correlation between the three observers and therefore this has negatively affected the correlation of ULDM with the ground truth.

Table 4.5 Cross-correlation comparison between the ULDM, manual measurements and their average value

		Observer 1	Observer 2	Observer 3	Obs_avg [a]	ULDM
HRIS	Observer 1	1				
	Observer 2	0.93 (*p=0<0.001*)	1			
	Observer 3	0.91 (*p=0<0.001*)	0.94 (*p=0<0.001*)	1		
	Obs_avg	0.97 (*p=0<0.001*)	0.98 (*p=0<0.001*)	0.97 (*p=0<0.001*)	1	
	ULDM	0.83 (*p=0<0.001*)	0.86 (*p=0<0.001*)	0.87 (*p=0<0.001*)	0.87 (*p=0<0.001*)	1
CLRIS	Observer 1	1				
	Observer 2	0.96 (*p=0<0.001*)	1			
	Observer 3	0.97 (*p=0<0.001*)	0.96 (*p=0<0.001*)	1		
	Obs_avg	0.99 (*p=0<0.001*)	0.98 (*p=0<0.001*)	0.99 (*p=0<0.001*)	1	
	ULDM	0.89 (*p=0<0.001*)	0.88 (*p=0<0.001*)	0.89 (*p=0<0.001*)	0.90 (*p=0<0.001*)	1
VDIS	Observer 1	1				
	Observer 2	0.93 (*p=0<0.001*)	1			
	Observer 3	0.92 (*p=0<0.001*)	0.90 (*p=0<0.001*)	1		
	Obs_avg	0.97 (*p=0<0.001*)	0.97 (*p=0<0.001*)	0.96 (*p=0<0.001*)	1	
	ULDM	0.88 (*p=0<0.001*)	0.90 (*p=0<0.001*)	0.87 (*p=0<0.001*)	0.91 (*p=0<0.001*)	1
KPIS	Observer 1	1				
	Observer 2	0.69 (*p=0<0.001*)	1			
	Observer 3	0.65 (*p=0<0.001*)	0.64 (*p=0<0.001*)	1		
	Obs_avg	0.90 (*p=0<0.001*)	0.87 (*p=0<0.001*)	0.87 (*p=0<0.001*)	1	
	ULDM	0.50 (*p=0<0.001*)	0.47 (*p=0<0.001*)	0.41 (*p=0<0.001*)	0.52 (*p=0<0.001*)	1

[a] Obs_avgis the data sequence containing average of vessel diameters measured by the three observers for each vessel cross-section.

4.6 Summary

This chapter has discussed a novel vessel edge localization and diameter measurement technique (ULDM) based on the Linear Discriminant Analysis (LDA) suitable for automation purpose. An unsupervised classifier was built to train the LDA classifier and make the entire classification process unsupervised, suitable for automation purpose as it does not require any manual training

or supervision. The LDA was used to categorize the intensity values on a vessel cross-section profile into three clusters. The horizontal distance between the two points as a result of the interaction between class boundaries and the vessel profile was taken as the vessel diameter. A MATLAB based computer program was created to test the robustness of the algorithm on more than 5000 normal and pathological cross-sections from the REVIEW dataset including mixed quality retinal images. The ground truth was based on the average diameter from semi-automated methods measured by three different experts to sub-pixel accuracy and compared with six established automated vessel diameter measurement techniques.

The proposed algorithm is robust against the commonly referred to as image artifacts, associated with fundus images which impair the grading performance. It was found to be suitable measurement method for the databases mostly include vessels with sharp transition edges and kick-points present in cross-sections. The advantage of this technique is that, unlike parametric methods (i.e. 1D, 2D, twin Gaussians), it does not require vessel profiles to be approximated by Gaussian function and therefore vessel diameter estimation depends neither on the performance of curve fitting process (goodness of fit) nor the spreading factor of the Gaussians functions. The technique is suitable for the vessel segments with any type of illumination and central light reflex artifact.

Chapter 5

Edge independent quantification of retinal vessel diameter variation

5.1 Introduction

The change in the width of the retinal arteriole and venules is direct indictor of retinal vasculature abnormality (Wang, Mitchell et al. 2003) and has been found associated with coronary heart disease (Wong, Klein et al. 2002), cardiovascular and cerebro-vascular mortality (Wang, Mitchell et al. 2002) and hypertension (Gao and Wei 2008). Measurement of vessel diameter necessitates accurate detection of retinal vessels and edge localization. Accurate edge perception is prone to some inaccuracies due to image artifacts (Lowell, Hunter et al. 2004) and in some cases requires manual intervention for fine adjustment. This chapter addresses the hypothesis of diameter inaccuracy as a result of subjective edge perception by proposing an edge independent representation of vessel diameter change based on variations in fractal dimension (FD) of vessel cross-section profile as time series signal. However, vessel diameter is a local feature while fractal dimension provides a global property and whether there is any link or correlation between these two features has never been investigated. This work has provided a link between retinal vessel diameter variations and fractal dimension by introduction of Directional Fractal Dimension (DFD) as a new feature and concept for the first time in retinal image analysis. The term directional is given as the FD is estimated in a specific direction. DFD provides a consistent representation of vessel diameter variations without requiring vessel edge identification and has the advantage of providing local feature for retinal vasculature analysis.

5.2 Background

As explained in chapter 2, several approaches exist for calculation of fractal dimension. The techniques which have been mostly used in the literatures for FD estimation of retinal images are based on binary box-counting and have been applied onto the entire image. This work measures the FDs using 1D image intensities along a path normal to vessel centreline (i.e. vessel cross-section profile). Therefore, only the fractal methods that suited for time-series signal analysis were investigated, including 2D Box-counting (BC_{2D}), 1D Box-Counting (BC_{1D}), Differential Box-Counting (BC_{Diff}) and the Higuchi's FD (D_H).

In the first method, the profile was projected onto a 2D plane in white on a black background. The binary box-counting FD was obtained as explained in chapter 2 and labeled as BC_{2D} due to analyzing a 2D entity. In this method a box was counted if it contained at least one sample of the intensity surface. It should be considered that the fractal dimensions measured on a planner will always have a value between 1 and 2 and represent the degree to which a signal fills a space in a 2D plane. In the second method, instead of embedding the profile in higher dimensions for FD quantification, the profiles were characterized in time domain and in form of 1D time-series signal. This included the Differential Box-counting (DBC) based on a concept similar to binary box-counting. In this method the intensity axis was covered with squares of decreasing side length size. The number of squares at each time interval equivalent to the size of square side length is calculated in a differential way by taking the difference between the box numbers containing maximum and minimum intensities. In this chapter this method has been referred to by BC_{diff}. In the final box counting method (BC_{1D}) the profiles were considered as matrices of zeros and ones by treating all non-zero intensity values as one as explained by Sarker *et.al* (Sarkar and Chaudhuri 1994).

5.3 Materials and Method

In order to test the hypothesis, two sets of experiments were conducted. In the first experiment, the relationship between diameter variation and change in different FDs (i.e. BC_{2D}, BC_{1D}, BC_{Diff} and D_H) were determined using synthetically developed images with cross-section profile of

similar to enhanced retinal images (Soares, Leandro et al. 2006) . The second experiment was conducted similarly but on natural retinal images (vessel profiles) taken from expert annotated REVIEW database (Al-Diri, Hunter et al. 2008).

5.3.1 Synthetic images

To study the association of vessel diameter with FD and its correlation with the change in cross-sectional diameter of a typical enhanced retinal vessel; a set of gray scale synthetic images were created. A number of fixed length, straight vessels were modeled with the vessel inside being white (intensity of 255) on a black background (intensity of 0). The resultant rectangular-shape cross-section profile was smoothened using an inverse symmetric Gaussian Blur filter (2 pixels blur radius and standard deviation of 1) to match the profile of natural enhanced retinal vessels. Example of the resultant synthetic image and a comparison between the profile of an enhanced natural retinal vessel and that of a synthetic image has been shown in Figure. 5.1 showing a very high correlation (r = 0.977, p<0.0001). Twenty three different synthetic vessels were created as shown in Figure 5.2 and the cross-sectional profiles were recorded. The synthetic vessel diameter were considered in the range of 1 to 23 pixels with one-pixel intervals, and this was based on the typical vessel diameter range in the REVIEW(Al-Diri, Hunter et al. 2008) database.

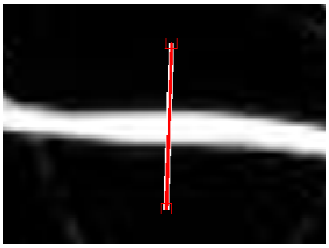

(a)

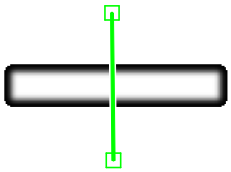

(b)

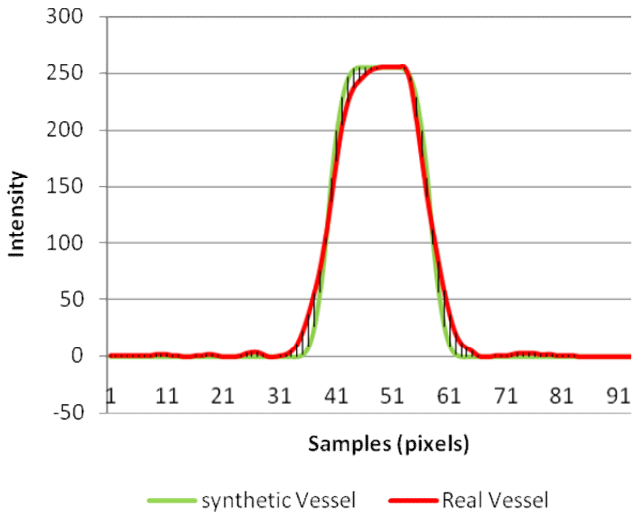

(c)

Figure 5.1 Comparison between real and synthetic retinal vessels cross-section profile. The both vessels have similar diameters (20 pixels) with the intensity levels ranging between 0 to 255 a) Real enhanced retinal vessel and its sample cross-section (red line) b) synthetic vessel and its sample cross-section (Green line) c) Cross section profiles of real (red) and synthetic vessels (green) showing high correlation (r = 0.977, p<0.0001).

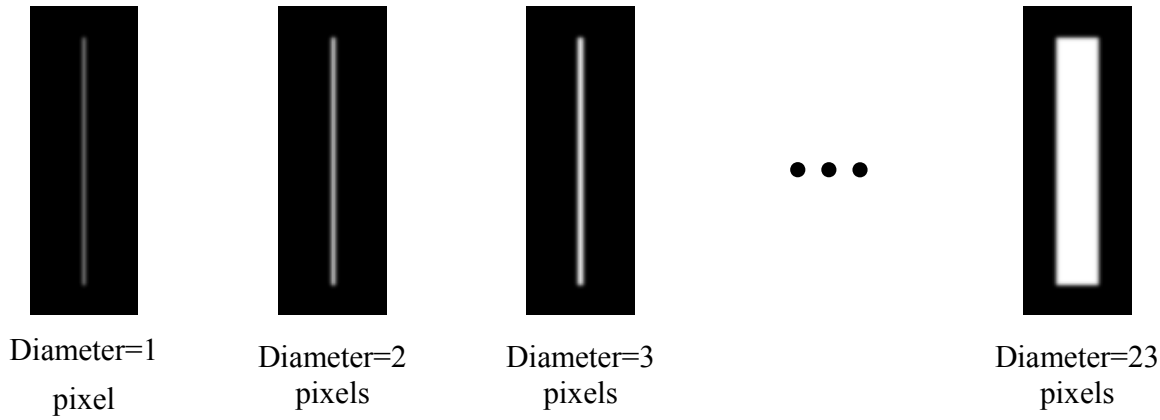

Figure 5.2 Synthetic retinal vessels (in white) with diameter range between 1 to 23 pixels (one pixel interval). The image is filtered with Gaussian blure filter (σ=1, radius=2×σ) to represent realistic Gabor enhanced retinal vessel with inverse Gaussian-like cross-section profile. The intensity levels range between 0 to 255.

5.3.1.1 Effect of Noise on Dimension Estimation

Fundus colour images are either taken digitally by digital retina cameras or have been digitized by scanners for computerized analysis. During the acquisition process, the images may be corrupted by noise due to the reasons such as the camera (CCD sensor) and scanner hardware, examiner error (e.g., focusing) and poor illuminations. Amplifier noise also known as Gaussian noise is of the most common noises inherently present on digital images and is generated as a result of amplification used in the RGB channels of the capturing devices. The standard model of amplifier noise is additive, Gaussian and independent of pixel intensity. In order to study the effect of noise on FD change with respect to diameter variations, Gaussian noise of zero mean and varying standard deviations (σ=0.01 to σ=0.1 with 0.01 intervals) was added to the synthetic images. The noise parameters were specified as the image intensities were in the range of 0 to 1. Therefore the image intensities were first normalized prior to noise-adding to fit in the above range and then converted back to their original unsigned 8 bit integer format within the range of

0 to 255. This will vary the overall image quality and can be useful in testing the performance of each method in the presence of noise variations.

5.3.1.2 Effect of number of samples (cross-section length)

The effect of cross-section length on FD variations with respect to diameter change was investigated on the synthetic images by varying the length of cross-section line along which the image intensities were recorded. The length was varied form the size of maximum vessel diameter to 4 times that value with 0.5×maximum diameter intervals followed by a normalization process to a range between 0 and 1. The normalization of the time (x-axis) guaranteed the increase in the sampling frequency within a similar interval for all recorded cross-sections.

5.3.2 Natural retinal images

After evaluating the relationship between FD and vessel diameter variations using the synthetic images, FDs were computed for the natural retinal images from the REVIEW database (Al-Diri, Hunter et al. 2008). Only CLRIS and HRIS image sets were used as VDIS shows low correlation between three observers and KPIS contains only a vessel segment not showing much diameter variations. Prior to FD measurement, image enhancement was performed on the inverted green channels, using 2D Gabor wavelet based on previously tested methods (Soares, Leandro et al. 2006; Azemin, Kumar et al. 2011). A 2D Gabor wavelet was employed as a directional matched filter on 18 equally spaced angles (10^o) from 0 to 170^o and five different scales (4, 5, 6, 7 and 8) for retinal image enhancement to extract the vascular network. Based on the work of (Soares, Leandro et al. 2006), the wavelet parameters including the elongation factor,ε and the horizontal and vertical frequencies K_0 were set to 4 and [0.. 3] respectively. This process was followed by feature normalization and finding the class-conditional probability density function to obtain a posteriori image according to Bayes's theorem. For detailed information on the technique see Soares *et.al* (Soares, Leandro et al. 2006). The entire image enhancement was performed using the Matlab based software ("*mlvessel*") provided by Soares *et.al* which is available online for free (soares 2008). The final Gabor enhanced (posteriori) image and its histogram is shown in Figure. 5.3.c and Fig. 5.3.d respectively.

Using the REVIEW database, the average location of the edge points marked by the three observers were used as a guide to locate the line normal to the vessel centre line and detect the cross-section profiles. All the profiles were extracted using the enhanced images along fixed-length lines equivalent to three times the maximum vessel diameter (D_{Max}) on the image. This provided 1D data sequences with equal lengths (number of samples) which is required for FD measurement. The length of $3\times D_{Max}$ was found to be the optimum value after comparing it against other possible lengths of the normal lines along which the intensities were recorded and have been shown in Figure. 5.3.c. The reference vessel diameter corresponding to each cross-section was calculated by finding the Euclidean distances between the vessel edge points reported by three graders and taking mean of the three values.

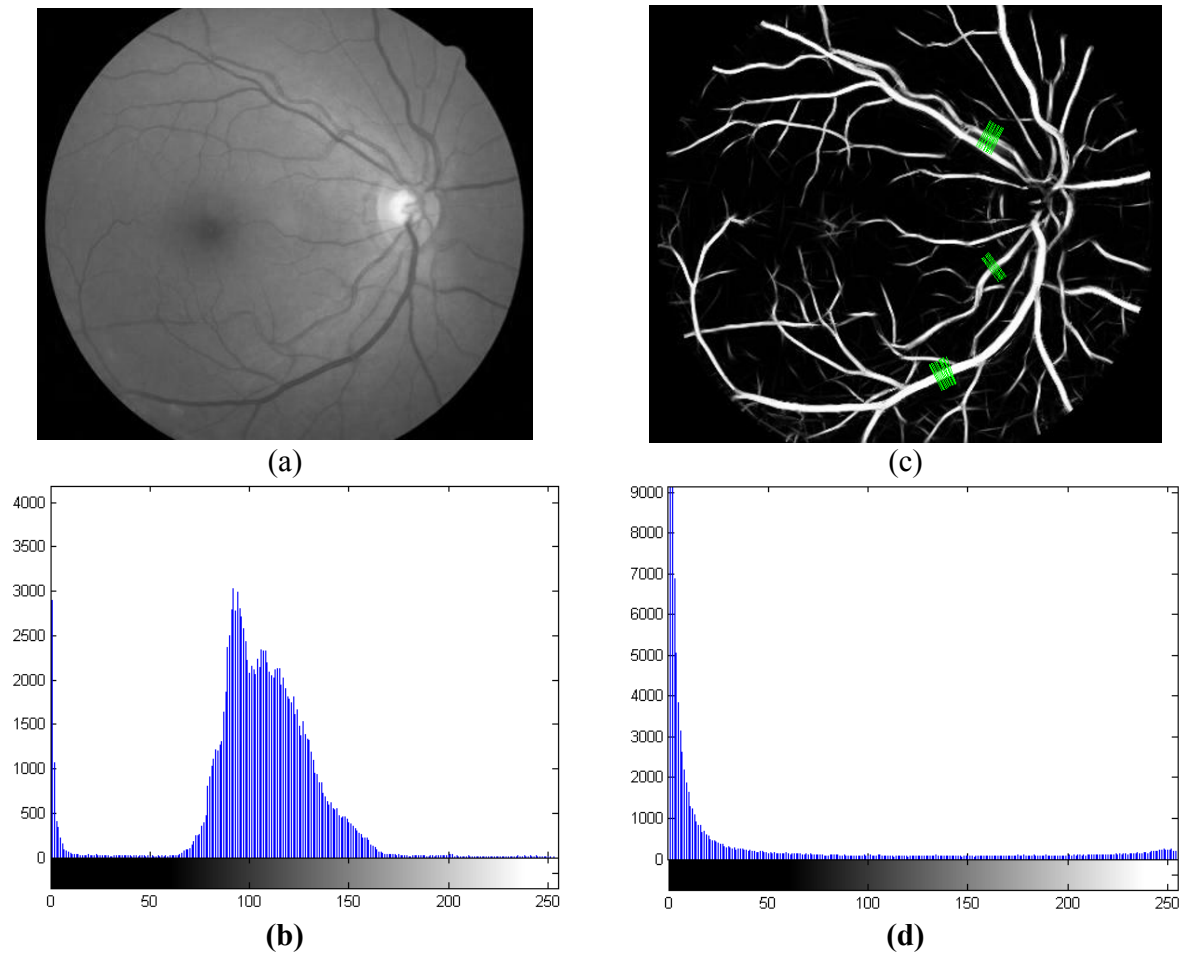

Figure 5.3 Retinal image enhancement a) Retinal image CLRIS001 (Green Channel) b) Histogram of the green channel c) Gabor enhanced image, the green lines are the lines normal to vessel centre line where the intensities were extracted d) histogram of the enhanced image.

5.4 Data analysis

Linear regression analysis was performed on the test results obtained from synthetic and natural images to investigate the relationship between DFD and vessel diameter as the two variables. The values were sorted according to the synthetic vessel diameter from the smallest to the largest one and presented on a 2D plot of dimension versus diameter. A least- square best-fit straight line was found for each measurement technique and the Pearson's correlation coefficient was calculated as measure of the goodness of fit for validation purpose. Separate analyses were performed for two independent variables of "number of samples" and "Noise" while holding one fixed in each analysis. Significance level (*p*-value) of correlation was calculated using the Medcalc® software.

5.5 Results

5.5.1 Validation on synthetic images

5.5.1.1 FD change with respect to diameter variations

Figure 5.4 shows the relationship of FDs computed using the four different algorithms including 1D (BC_Bin), 2D and differential Box_counting and Higuchi's method with the vessel diameter variations using noise free synthetic images. BC_{2D} and BC_{Diff} were found to have no significant relationship with the vessel diameter; both showing linear least square best fits of zero slope and correlation of -0.71 ($p<0.0001$) and -0.79 ($p<0.0001$) respectively. Higuchi's (D_H) was inversely correlated with diameter variations ($r=-0.99$, $p<0.0001$) and BC_{1D} showed direct correlation of $r=0.98$, ($p<0.0001$). Therefore, only the D_H and BC_{1D} were considered and BC_{2D} and BC_{Diff} were excluded in further analyses.

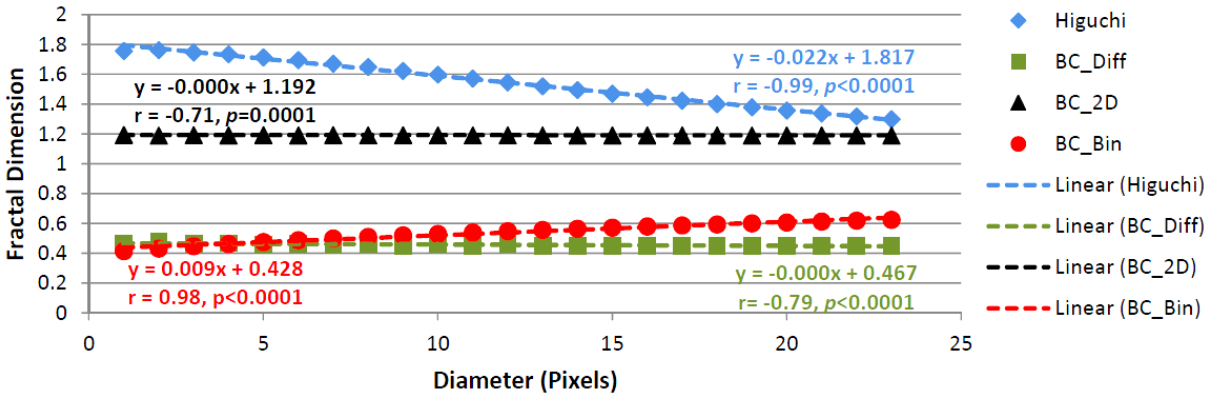

Figure 5.4 FD Vs vessel diameter variations (ranging from 1 to 23 pixels with one pixel interval) using noise free synthetic images. i.e Higuchi's Dimensions (blue trend), differential box-counting (green), 2D box-counting (black) and 1D box-counting (red). The equation of least square best fit straight lines and r (Pearson's correlation coefficient) have been presented next to each trend line.

5.5.1.2 Effect of additive Gaussian noise on FD variations

The effect of additive Gaussian noise to the image on the BC_{1D} is shown in Figure 5.5.a, while that for D_H is shown in Figure 5.5.b. The results show that BC_{1D} performed poorly with noise, and there was no longer any significant linear relationship with vessel diameter, with significantly reduced r of 0.644 (p=0.0009) and 0.599 (p=0.0025) for the Gaussian noise with SD of σ=0.01 and σ=0.1 respectively. In the presence of additive Gaussian noise of zero mean, D_H showed high inverse linear relationship with the diameter increment. (r = 0.995, p<0.0001 and r =-0.958, p<0.0001 for σ=0.01 and σ=0.1 respectively).

This indicates that in the presence of noise, BC_{1D} does not display strong relationship with the diameter of the vessel, but Higuchi FD shows high inverse linear correlation to vessel diameter variation trend. This shows a small increase in the slope (decrease in the absolute slope) of the regression line due to additive noise.

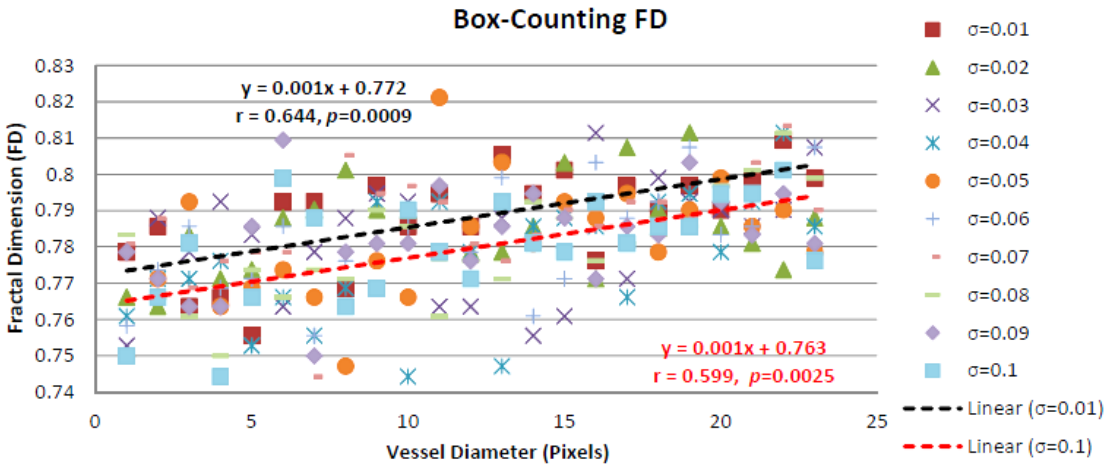

(a)

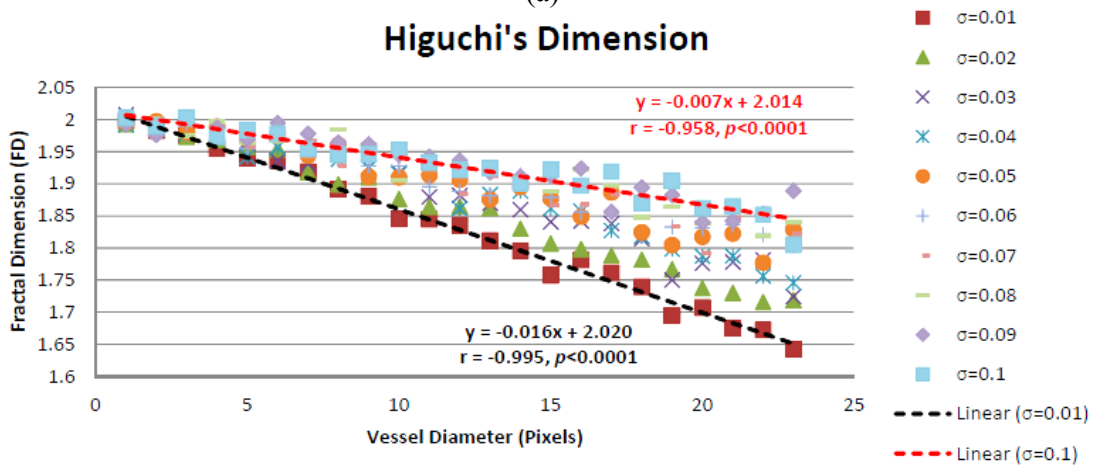

(b)

Figure 5.5 Effect of Additive Gaussian noise with zero mean and different variances (σ=0.01 to σ=0.1 with 0.01 intervals) on the relationship between Fractal dimensions and vessel diameter (from 1 to 23 pixels and one pixel interval) using synthetic images. The equation of least square best fit straight lines and r (Pearson's correlation coefficient) have been demonstrated for two cases of σ=0.01 (Black line) and σ=0.1(Red line).a) Box-Counting Dimension (DBC) b) Higuchi's Dimension (DH).

5.5.1.3 Effect of number of samples on FD variations

Figure 5.6 shows the relationship of BC_{1D} and D_H with respect to cross section length. The length was varied from 1 to 4 times the maximum diameter available in the database. According to this figure, the number of samples or data points seems to have negligible effect on both BC_{1D} and D_H resulting to r>=0.95 (all *P*-values <0.0001) for all cases. Increasing the samples slightly affects the slope of the regression line as well as reducing the curvature of the FD Vs Diameter

trends towards a straight line. This behaviour was more evident in D_H than in BC_{1D} therefore for the purpose of robustness and obtaining the result to some certain linearity; the minimum cross-section length should be set to at least 3 times the maximum vessel diameter.

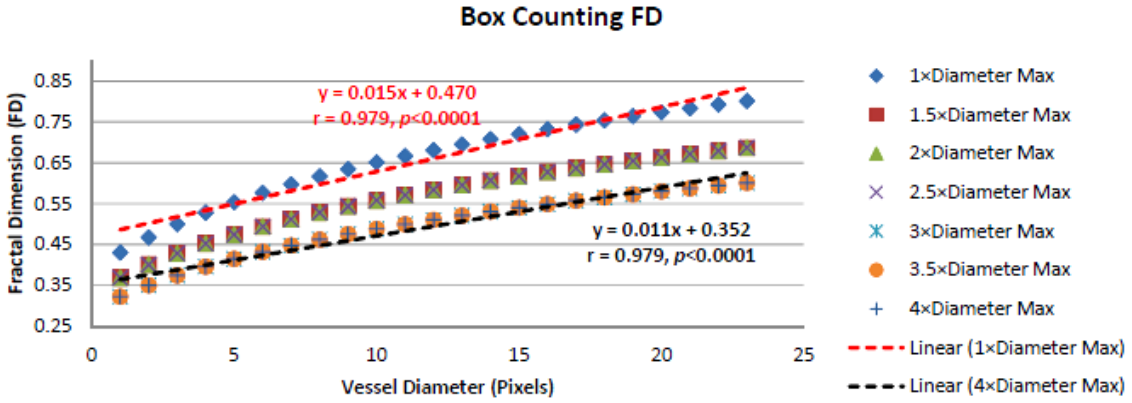

(a)

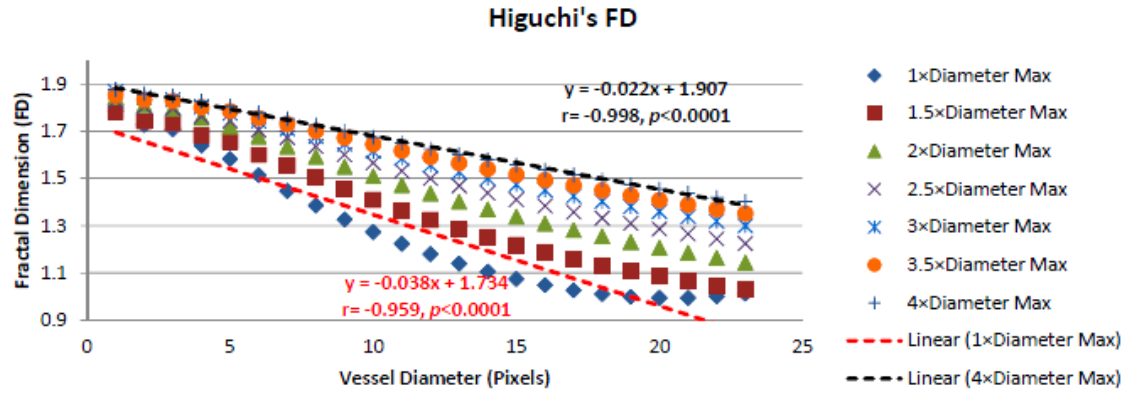

(b)

Figure 5.6 Effect of the number of samples (length of cross-section profile/Curve) on Fractal dimensions change with respect to vessel diameter variations (from 1 to 23 pixels and one pixel interval) using synthetic images. The length of corss-section profile varried from the size of maximum diameter (i.e 23 pixels) to four times that value with 0.5×Maximum Diameter increments. The equasion of least square best fit straight lines and r (Pearson's correlation coefficient) have been demonstrated for two cases of N= 1×Maximum Diameter (Red line) and 4×Maximum Diameter (Black line).a) Box-Counting Dimension (BC_{1D}) b) Higuchi's Dimension (D_H)

5.5.2 Validation on natural retinal images

Table 5.1 reports the validation result using CLRIS and HRIS image sets from the REVIEW database. The number of cross-sections that were available in the database is presented in

column 3. Column 4 shows the average and standard deviation of FD obtained according to each FD algorithm. The correlation coefficients *r* between the FD and the reference diameter has been presented in column 5. Columns 6 and 7 show the 95% CI for the *r* and the significance level respectively. From this table, it is observed that D_H showed higher inverse correlation for each cross-section vessel diameter compared with BC_{1D}. In fact, D_H had the highest correlation coefficient in all cases with maximum of r = -0.96 (95% CI -0.980 to -0.920, p<0.0001) for the CLRIS001 image. The FD computed using box-counting (BC_{1D}) did not show any significant correlation for this image (r = 0.057, 95% CI -0.297 to 0.398, p=0.755) but had a relatively significant correlation with the diameter on other images especially for CLRIS002 (r = 0.748, 95% CI 0.689 to 0.798, p<0.0001) and HRIS004 (r = 0.800, 95% CI 0.719 to 0.860, p<0.0001).

Table 5.1 Correlation of Higuchi's and 1D box-counting dimensions with the ground truth vessel diameters measured using CLRIS and HRIS image set from the REVIEW database.

Image Name	Method	No. of Cross section	Mean FD(SD)	Correlation Coefficient r	95% CI for r	P value	Mean Diameter in pixels (SD)
CLRIS001	**D_H**	32	1.138 (0.078)	-0.960	(-0.980, -0.920)	<0.0001	17.359
	BC_{1D}	32	0.647 (0.030)	0.057	(-0.297 , 0.398)	0.755	(1.403)
CLRIS002	**D_H**	253	1.273 (0.162)	-0.895	(-0.917, -0.867)	<0.0001	13.345
	BC_{1D}	253	0.627 (0.071)	0.748	(0.689, 0.798)	<0.0001	(4.129)
HRIS001	**D_H**	1215	1.577 (0.086)	-0.859	(-0.873, -0.844)	<0.0001	3.975
	BC_{1D}	1215	0.465 (0.038)	0.542	(0.501, 0.580)	<0.0001	(1.287)
HRIS002	**D_H**	452	1.588 (0.087)	-0.876	(-0.895, -0.852)	<0.0001	4.310
	BC_{1D}	452	0.469 (0.039)	0.621	(0.561, 0.675)	<0.0001	(1.190)
HRIS003	**D_H**	596	1.579 (0.055)	-0.641	(-0.686, -0.591)	<0.0001	5.122
	BC_{1D}	596	0.486 (0.038)	0.448	(0.381, 0.510)	<0.0001	(0.850)
HRIS004	**D_H**	105	1.566 (0.041)	-0.817	(-0.872, -0.742)	<0.0001	4.490
	BC_{1D}	105	0.480 (0.057)	0.800	(0.719, 0.860)	<0.0001	(1.073)

5.6 Summary

This work has shown that there is a general relationship between DFD with the variations in diameter of the retinal vessels, validated on both synthetic and expert annotated publicly available retinal images (REVIEW database). The result has shown that while some FDs have a relationship with vessel diameter, D_H has the strongest correlation and has the best immunity

against the background noise. This indicates that Higuchi's FD would be most suitable FD for distinguishing change to the vessel diameter.

The major impact of this work is the introduction of Higuchis' dimension as an alternative feature to vessel diameter measurement for identifying diameter variations when the actual value is not important. In this work D_H has been found to be sensitive to vessel diameter variations to one pixel accuracy and insensitive to other image artifacts. Its relative noise immunity as well as linear behavior makes it a good alternate for quantification of diameter variations in disease investigations.

Accurate vessel diameter measurement and vessel edge localization has always been a challenge for the graders due to low image contrast, uneven illuminations, vessel central light reflex and other artifacts (e.g. background noise), leading to inconsistent vessel edge perception and therefore diameter estimation. Higuchis' FD in vessel cross-sectional direction provides a consistent measure of vessel diameter variations without requiring vessel edge identification and has the advantage of providing local feature of retinal vasculature. It is also suitable for automation purposes as there is no need for image segmentation, manual supervision or any extensive pre-processing to be performed, unlike other methods which rely heavily on image segmentation for vessel boundary delineation (Bhuiyan, Nath et al. 2009; Xiayu, Niemeijer et al. 2011). There has been a claim that vessel segmentation will cause loss of caliber information and therefore is not suitable for diameter measurement(Che Azemin, Kumar et al. 2012).

Chapter 6

Application of calibre specific DFD for stroke detection

6.1 Introduction

This chapter explains the clinical association of the retinal vessel calibre variation and the DFD based on Higuchi's method (chapter 5) with vessel calibre related retinopathies due to coronary heart disease (CHD) and risk of stroke. Unlike other techniques which provide a global measure (Doubal, MacGillivray et al. 2010; Kawasaki, Che Azemin et al. 2011), the proposed feature presents an automatic assessment tool for localized/regional analysis of retinal images and reports the association of each region with the risk of disease incidence. The technique has been validated as a new feature or stroke biomarker for 10-year stroke risk assessment using image sets from the Blue Mountain Eye Study (BMES) database, Sydney, Australia (Mitchell, Smith et al. 1995; Wang, Mitchell et al. 2002; Mitchell, Wang et al. 2005).

6.2 Background

As stated in chapter 2, alteration in Fractal Dimension (FD) (Che Azemin, Kumar et al. 2010; Kawasaki, Che Azemin et al. 2011) and vessel caliber (Wang, Mitchell et al. 2002; McGeechan, Liew et al. 2009) of retinal images have been shown to be associated with stroke event and also as indication of cerebral microvasculature and cardiovascular abnormalities. Therefore, a number of techniques have been reported for fractal characterization of retinal images (Landini, Misson et al. 1993; de Mendonca, de Amorim Garcia et al. 2007; Azemin, Kumar et al. 2011; Kawasaki, Che Azemin et al. 2011). The box-counting method has been employed by Mendonca et al. (de Mendonca, de Amorim Garcia et al. 2007) showing the result to be susceptible to the measurement method and at risk of being degraded by image segmentation as essential preprocessing step. Therefore, in order to overcome the segmentation limitation, Azemin et al.

(Azemin, Kumar et al. 2011) proposed the Fourier fractal dimension and applied the technique to the gray scale (green channel) retinal images after being enhanced by Gabor wavelet transform. Later application of this work was tested by Kawasaki et al. (Kawasaki, Che Azemin et al. 2011) in a cohort study of stroke risk assessment. They found a statistical significance (p=0.044, α=0.05) between the case and control groups with lower spectrum fractal dimension (SFD) of 1.504 (95%CI, 1.499- 1.510) associated with higher risk of stroke compared to the lower SFD 1.511 (95%CI, 1.507- 1.515). Advantages of using FD are that it summarizes the obtained information into a single value which is very convenient in terms of feature reduction concept and for statistical analysis. It is also suitable for automatic assessments without requiring extensive user intervention. However, FD as a global measure has always been applied to the entire image and is unable to provide analytical information corresponding to a local region of retina and its association with disease condition. The need for both summarized and local based assessment has led to application of retinal vessel summary formula, CRAE and CRVE, (Wang, Mitchell et al. 2002; Wang, Liew et al. 2007) which are mostly measured in a circular region equivalent to 0.5–1 disc diameters from the disc margin (Zone B).

In this work, it has been hypothesized that a region based fractal measure would provide more specific information on the association of the significance level of alterations in FD due a stroke. It has also been hypothesized that the image artifacts on the optic disk (OD) region would degrade the variability of fractal values due to disease condition and need to be masked before measuring the fractal properties. The effect of OD on FD analysis has not been shown in other studies (e.g. SFD (Kawasaki, Che Azemin et al. 2011)).

This work has proposed the region based directional fractal estimation based on the Higuchi's method with circular scanning around optic disk (OD) as new measure of FD to summarize the complexity of enhanced retinal microvascular pattern without requiring any segmentation or image binarization. A comparison was made between different scanning directions including horizontal, vertical, circular , radial and the state of the art Spectrum Fractal Dimension (SFD) (Kawasaki, Che Azemin et al. 2011) and box-counting technique in terms of providing the most significance level in a case-control study. The study is to differentiate between control participants and the one who later suffered from an episode of stroke. A zone based analysis was

also conducted to examine the effect of different selection of region of interest (ROI) and OD masking on fractal properties of retinal microvasculature.

6.3 Material

The Retinal images from the BMES, a population-based study conducted in a suburban region west of Sydney, Australia, were analysed (Mitchell, Smith et al. 1995; Mitchell, Wang et al. 2005). The participant's age range was 50-89 years. Images of the retina from both eyes of the study participants were obtained using a Zeiss FF3 fundus camera having 30 degree field. The photographs were taken after pupil dilation. The images were digitized using a Cannon FS2710 scanner with maximum resolution of 2720 dpi in 24-bit colour format. Among the total number of 1532 optic disk (OD) centred images (3888×2592 pixels) in the database, total number of 104 cases were confirmed with CHD or stroke after10-year follow-up. Self-reported stroke events were validated against medical records of physician diagnosis based on the World Health Organization Monitoring Trends and Determinants in Cardiovascular Disease (WHO-MONICA) plus evidence from computed tomography or magnetic resonance imaging (Mitchell, Wang et al. 2005) .Only images from the left eye were analysed. Eight of the images from the whole database were discarded due to quality and contrast problem. Retinal images of stroke and cases were matched based on the age (mean (SD) = 67.76 (5.72)), metric body mass index (BMI) (26.32 (4.35)), blood pressure (mmHg) (systolic: 150.64 (18.94)), diastolic 83.40 (10.35)) and history of smoking. An independent third party ophthalmologist confirmed matching of 46 cases with 39 controls which used in this study. The matching control set was of people who did not have history of stroke, hypertension, and diabetes at the baseline and did not develop any of them during the period of the study.

The inverted green channel was used (Che Azemin, Kumar et al. 2010) as this provided better vessel to background contrast compared to the other two channels (Red and Blue). The images were cropped using a mask of size 1960×1960 pixels to cover a region of interest (ROI) corresponding to a circle of 4 OD diameter (D_{OD}) centered at OD center. The OD center and boundary were identified manually by the grader (Azemin, Kumar et al. 2011). The cropped image was then down-sampled to 400×400 pixels (Figure 1.a) to reduce the computational

complexity similar to other studies (Che Azemin, Kumar et al. 2010; Azemin, Kumar et al. 2011). Image enhancement was also performed to compensate for uneven illuminations and ocular media opacity using 2D Gabor wavelet filter as in chapter 5.3.2 using the online "*mlvessel v1.3*" Matlab based software provided by Soares et al. (soares 2008).

6.4 Methodology

6.4.1 Scanning method and its association with Higuchi's FD for stroke detection

As stated in chapter 5.2.2, Higuchi measures the FD of a set of points in the form of 1D time series (Higuchi 1988). It can address some limitations of other 2D fractal algorithms such as the box-counting through obtaining the FD along a specific direction. In order to find the Fractal value of the images (as 2D entity), the intensity values need to be transformed into several 1D signals. This is possible by a number of scanning methods including horizontal and vertical scanning by decomposing an image of size (M×N) into its M rows and N columns as well as the spiral and radial extraction of the intensity values (Ahammer 2011). In this work several scanning methods have been tested and their association with stroke has been compared. For the horizontal (Figure 6.1.a) and vertical (Figure 6.1.b) scanning, the gray values were scanned along horizontal and vertical lines and a set of FD-$H_{1\text{-}M}$ and FD-$V_{1\text{-}N}$ values corresponding to the number of columns and rows were obtained. The final FD-H and FD-V were obtained by averaging the horizontal (FD-$H_{1\text{-}M}$) and vertical (FD-$V_{1\text{-}N}$) dimensions respectively. Another possible technique for calculating Higuchi's dimension of retinal images was to scan the image along a number of radial lines passing through the OD center and recording 1D intensities along radial lines equally spaced with θ^o angles (here θ was set to 1^o) to cover the ROI (Figure 6.1.c). A set of FD-$R_{1\text{-}k}$ with the *K* being the total number of lines was obtained and the overall FD-R was calculated by averaging the whole values.

Selection of an appropriate scanning method depends on image features of interest. In this study concentric circles around the OD were proposed and tested. Such a scanning path intersects with most major vessels' along their cross-section and provides vessel caliber information as the

major vessels of the retina are in radial direction with respect to the OD. The circles were spaced with one pixel intervals in the ROI with the innermost circle having its radius one pixel greater than that of the OD, and the outermost circle with diameter 4× D_{OD}. Some examples of these scanning circles are shown in Figure 6.1.d. Higuchi's FD was estimated for each of the circular scans and referred to as FD circular, or FD-C. The average of FD-C of all circles was considered as FD-C corresponding to the ROI.

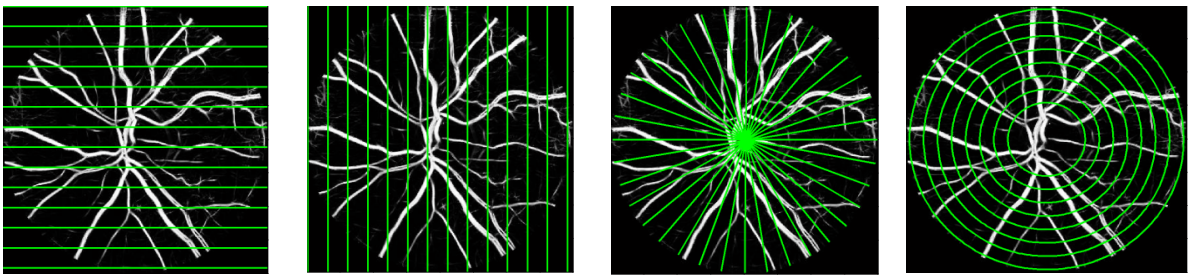

(a) (b) (c) (d)

Figure 6.1 Demonstration of different scanning methods a) Horizontal b) Vertical c) Radial d) Circular on the enhanced retinal image.

In this work, all the four different scanning methods (horizontal, vertical, radial and circular) have been tested on enhanced retinal images with both preserved and masked OD and were compared with Binary Box-Counting (BC) and SFD method (Kawasaki, Che Azemin et al. 2011) to study the effect of OD masking on the extraction of relevant information associated with risk of stroke.

6.4.2 Zone specific analysis of Higuchi's FD (FD-C)

Using FD-C, A Zone based analysis was performed to study the potential impact of zone selection and also to identify the zone, which was most affected by the disease (stroke) factor. A mask of concentric circles (circular scanning paths) centered at OD center was created for each image, with the smallest circle corresponding to the OD boundary with diameter D_{OD}. The ROI was divided into three concentric zones (A, B and C), with A corresponding to a circumferential zone between 0 to 0.5×D_{OD} from the OD margin. Similarly, B and C were defined between 0.5 to 1 and 1 to 1.5×D_{OD} from its margin, respectively (Figure 6.2). The 1D data series were separately

obtained for each zone on the circular paths and the average of all FD values in each zone was calculated. All seven possible zone combinations including A, B, C, AB, BC, AC and ABC were considered and their associations with case/control groups for FD-C_A, FD-C_B, FD-C_C, FD-C_{AB}, FD-C_{BC}, FD-C_{AC}, FD-C_{ABC} were tested.

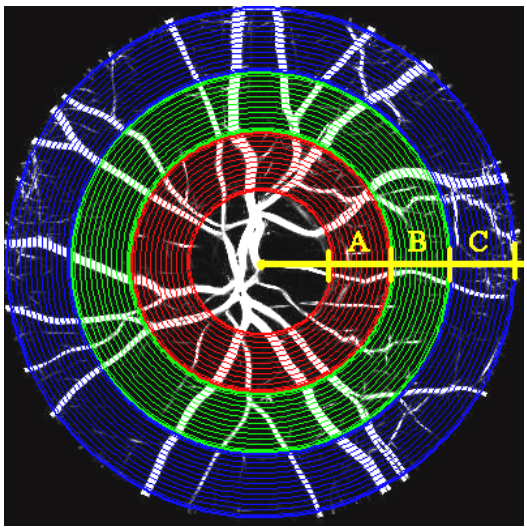

Figure 6.2 Representation of three different zones, A (red), B (green) and C (blue) around the OD with respect to one to three OD radius from OD boundary and circular scanning in the defined regions.

6.5 Data analysis

Statistical analyses were performed using Minitab 16 (Minitab Inc.). For each FD measurement technique, the measured values between the subjects were compared and the significance of association (*p*-values) between case and control groups was tested using the non-parametric Kruskal-Wallis analysis as an alternative method to ANOVA analysis as the normality condition of the data was not satisfied. The Kruskal-Wallis test identifies whether the population medians (η) on response variables are similar across all levels of factors (H_0: $\eta_{Case} = \eta_{Control}$ Vs H_1:$\eta_{Case} \neq \eta_{Control}$) and unlike ANOVA or T-test, the distribution of the response variables do not have to be of any particular form (e.g. normal). This test is suitable for the populations with two levels of independent variables (in our case (case/control)).

Two different sets of tests were performed; one on full images and the other on the OD masked version to study the effect of OD on the outcome. For the Zone based analysis, all the seven FD-Cs corresponding to the regions around OD were compared accordingly using Kruskal-Wallis analysis. The 95% confidence interval (CI) for the difference in population medians (η_{Case}-$\eta_{Control}$) was also obtained by non-parametric pair-wise comparison between the case and control groups using the Mann-Whitney as a follow up measure. The Mann-Whitney test is also known as Wilcoxon rank-sum test and is an alternative to two-sample T-test for measuring the statistical significance between two populations (here: case and control) when the data are not normally distributed.

6.6 Results

6.6.1 Comparison between different FD methods

Tables 6.1 and 6.2 show the difference between FDs of the case and control groups for full and OD masked retinal images. The first column identifies the method by which the FD was calculated. The second and fifth column give the median of FDs for control and case groups. The average rank is presented in the third and sixth columns while Z-values are in columns four and seven. The 95% CI for η_{Case}-$\eta_{Control}$ (from Mann-Whitney test) are in column eight, and the Kruskal-Wallis H parameter are listed in column nine. The last column illustrates the *p*-value obtained by Kruskal-Wallis analysis. The results show that there is a statistically significant difference (H=5.80, p = 0.016, α=0.05) between FDs of the case and control groups obtained when using the FD_C with 95% CI η_{Case}-$\eta_{Control}$ = -0.0087, -0.0007. However, no statistical significance was detected for other FDs (all *p*-values>0.05).

The OD masking was found to have no effect on the statistical significance between the case and control groups for FD_H (H=0.07, p=0.798), FD_V (H=2.46, p=0.116,) FD_R (H=0.0, p=0.958), SFD (H=0.51, p=0.475) and BC (H=0.41, p=0.520) measurement methods. The overall result for the FD-C method, shows lower fractal values for the cases compared to the control groups.

Table 6.1 Non-parametric Kruskal-Wallis and Mann-Whitney significance test between control and case groups on retinal images with OD included.

Method	Full Retinal Images (OD included)						95 % CI for $\eta_{Case}-\eta_{Control}$	H	**P-Value $\eta_{Case} = \eta_{Control}$ Vs ($\eta_{Case} \neq \eta_{Control}$)
	Control (n=39)			Case (n=46)					
	Median (η)	Average Rank	Z	Median (η)	Average Rank	Z			
FD-H	1.851	46.1	1.08	1.845	40.3	-1.08	-0.0093,0.0027	1.16	0.282
FD-V	1.894	45.4	0.81	1.892	41.0	-0.81	-0.0082,0.0034	0.66	0.417
FD-C*	1.987	50.0	2.41	1.981	37.1	-2.41	-0.0087, -0.0007	5.80	0.016
FD-R	1.837	42.9	-0.03	1.843	43.1	0.03	-0.0242,0.0227	0.00	0.979
SFD	1.335	46.1	1.07	1.335	40.4	-1.07	-0.0006,0.0002	1.14	0.286
BC	1.648	41.3	-0.58	1.653	44.4	0.58	-0.0080,0.0140	0.33	0.563

Table 6.2 Non-parametric Kruskal-Wallis and Mann-Whitney significance test between control and case groups on retinal images with masked OD.

Method	OD Masked Retinal Images						95 % CI for $\eta_{Case}-\eta_{Control}$	H	**P-Value $\eta_{Case} = \eta_{Control}$ Vs ($\eta_{Case} \neq \eta_{Control}$
	Control (n=39)			Case (n=46)					
	Median (η)	Average Rank	Z	Median (η)	Average Rank	Z			
FD-H	1.841	42.3	-0.26	1.841	43.6	0.26	-0.0067,0.0087	0.07	0.798
FD-V	1.879	47.6	1.57	1.877	39.1	-1.57	-0.0072,0.0008	2.46	0.116
FD-C*	1.987	50.0	2.41	1.981	37.1	-2.41	-0.0087, -0.0007	5.80	0.016
FD-R	1.869	43.2	0.05	1.868	42.9	-0.05	-0.0156,0.0153	0.00	0.958
SFD	1.336	45.1	0.71	1.336	41.2	-0.71	-0.0005,0.0002	0.51	0.475
BC	1.623	41.1	-0.64	1.623	44.6	0.64	-0.0078,0.0144	0.41	0.520

* Circular scanning method does not cover the OD area therefore there will be no change on the values of FD-C after masking the OD. ** Bonferronni corrected *P*-values (N=6).

6.6.2 Zone based analysis of FD-C

The comparison of the FD-C for different zones of the retinal images is shown in Table 6.2. The first column lists the zones where the FD-C was calculated. The rest of the columns are similar to those of Tables 6.1 and 6.2. From this table, it is observed that the two groups (case and controls) are not statistically significant based upon the FD-C_A alone (H=2.60, p=0.107, α= 0.05, 95% CI (-0.0073, 0.0009)). The results are similar for regions C (FD-C_C) and FD-Cs of regions A and C together (FD-C_{AC}). However, FD-C_B, FD-C_{AB}, FD-C_{BC} and FD-C_{ABC}, are found to be statistically significant with the p-values of 0.016, 0.025, 0.031, 0.016 (α= 0.05) respectively.

Table 6.3 Kruskal-Wallis and Mann-Whitney Zone based FD-C test of significance

Method	Zone based Analysis						95 % CI for $\eta_{Case}-\eta_{Control}$	H	P-Value $\eta_{Case} = \eta_{Control}$ Vs ($\eta_{Case} \neq \eta_{Control}$)	Statistical Significance (α=0.05)
	Control (n=39)			Case (n=46)						
	Median (η)	Average Rank	Z	Median (η)	Average Rank	Z				
FD-C_A	1.976	47.7	1.61	1.973	39.0	-1.61	-0.0073,0.0009	2.60	0.107	Not significant
FD-C_B	1.994	50.0	2.40	1.989	37.1	-2.40	-0.0079,-0.0008	5.75	0.016	**Significant**
FD-C_C	1.994	48.4	1.85	1.988	38.4	-1.85	-0.0118,0.0003	3.43	0.064	Not significant
FD-C_{AB}	1.983	49.5	2.25	1.981	37.5	-2.25	-0.0074,-0.0005	5.06	0.025	**Significant**
FD-C_{AC}	1.984	48.6	1.91	1.981	38.3	-1.91	-0.0090,0.0000	3.66	0.056	Not significant
FD-C_{BC}	1.993	49.3	2.15	1.988	37.7	-2.15	-0.0101,-0.0006	4.63	0.031	**Significant**
FD-C_{ABC}	1.987	50.0	2.41	1.981	37.1	-2.41	-0.0087,-0.0007	5.80	0.016	**Significant**

6.7 Summary

FD measurement techniques are convenient methods for summarizing the retinal vessel complexity and have been found to be useful by case/control studies (Cheung, Donaghue et al. 2009; Kawasaki, Che Azemin et al. 2011; Azemin, Kumar et al. 2012). Unlike vessel caliber measurement techniques, FD measurement does not require extensive manual supervision and is suitable for automatic assessments and feature summarization. However, while the vessel caliber summarizing techniques are specific to zones within the retinal images (Wang, Mitchell et al. 2002), the FD techniques do not allow zone specific or region based analysis of retinal images with respect to a distance from OD margin.

This works has introduced a new method to obtain Higuchi's fractal dimension and perform region/local based analysis of retinal images. In this method, the image is scanned using circles around the optic disc (OD) and is referred to as circular FD (FD-C). This method allows the scanning within a specific zone of OD centric retinal image. The other advantage of this method is that unlike box-counting FD, this does not require image segmentation (de Mendonca, de Amorim Garcia et al. 2007). In order to test its efficacy in distinguishing between case and control, it was compared with BC (Masters 2004) and SFD (Kawasaki, Che Azemin et al. 2011) methods when applied to a clinically adjusted subsample of BMES population database. The results show that FD-C had a significant relationship with the 10-year indicator of CHD and stroke and thus was significantly better predictor of CHD and stroke (p=0.016, α=0.05) while

other fractal measures did not show any significant association for these subsamples (all *p*-values>0.05). The median FDC for the entire image was lower (1.981) for the cases compared to the controls (1.987). This indicates that reduction in the complexity of the retinal vasculature is an indicator of disease, and is comparable with findings of Lipsitz et al.(Lipsitz and Goldberger 1992) which is associated with functional loss (Kyriazis 2003), Such loss of complexity has also been observed associated with ageing and disease in cardiac activity (Pikkujamsa, Makikallio et al. 1999), neural system (Schierwagen), electromyogram (EMG) (Kaplan, Furman et al. 1991; Skinner 1994; Kresh and Izrailtyan 1998) and general physiological measures (Kyriazis 2003), This study indicates that prior to an episode of stroke, the rarefaction of the retinal vasculature which is associated with reduction in the fractal dimension of the eye fundus image (Azemin, Kumar et al. 2012). The major implication of this study is that by using FDC, it is possible to assess the risk of stroke.

The weakness of this study is that only people above the age of 49 have been considered, and BMES represents narrow demographics. Also there is still room for improvement by analyzing the arteries and veins separately in future studies.

Chapter 7

Application of calibre specific DFD for analysis of type 2 diabetes

7.1 Introduction

This chapter studies the association between variations in different retinal fractal dimension (FD) especially the "Vessel Caliber Correlated Directional Fractal Dimension" (chapter 5) and the presence of mild Non-proliferative diabetic retinopathy (NPDR) using multiple FD comparisons among Indian population of healthy and individuals with type 2 diabetes. The association of FDs with gender and diabetes and also the change in prevalence of NPDR with respect to FD variations and age factor has been investigated.

7.2 Background

There is significant increase in the number of diabetic people in the world (CDC 2005), with a very steep rise in diabetes among the younger cohort (Engelgau, Geiss et al. 2004). The prevalence is significantly higher in the ethnic groups, and often in countries with lower availability of quality healthcare facilities. Untreated diabetes can lead to number of complications, such as diabetic retinopathy (DR) (Kempen, O'Colmain et al. 2004), and diabetic neuropathy (Wong, Chung et al. 2007). Diabetes patients are more likely to suffer blindness, neuropathy, ventricular arrhythmia, silent ischaemia, sudden cardiac death and stroke compared with other people.

There have been successes with the population screening to identify diabetes (Klein, Klein et al. 2006; Wong, Mohamed et al. 2006; Nguyen, Wang et al. 2008; Abramoff, Reinhardt et al. 2010). However, opportunistic evaluation accounts for the largest detection of diabetes patients among the low risk population and is largely based on the visit of the person to their primary health provider for other health factors. With the reduction in the age of the diabetes patients (Dabelea,

Hanson et al. 1998; Rosenbloom, Joe et al. 1999) commonly appearing among teenagers, a number of patients go undiagnosed for a significant period (WHO 2003) and are often diagnosed subsequent to the manifestation of the secondary symptoms.

There are number of screening methods for detecting diabetes. While the cost of individual tests has been falling rapidly, the average cost of every new successful identification of a diabetes patient in countries such as USA and Australia is estimated to be $840 (WHO 2003). Large numbers of people around the globe, who are unable to get timely diagnosis of diabetes, often end up developing DR or other complications. In countries such as Australia and Brazil, one out of every two cases of Diabetes are undiagnosed (WHO 2003) until the manifestation of the associated complications. In other parts of the world, the percentage of diabetes patients that do not get timely diagnosis is significantly higher (Lee, Feldman et al. 2003).There is a need for screening techniques outside of the clinic or hospital that can identify the diabetes patient in the early stage.

This work has proposed the use of directional fractal estimation based on the Higuchi's method (FD-C) for automatic assessment of type 2 diabetes. The interrelationship between variations in different retinal FDs was examined using a cohort population of healthy and individuals with mild NPDR. Comparative evaluation was performed between binary box-counting (BC); gray scale (differential) BC and Higuchi's directional FD to assess microvascular complications and its associations with retinopathies using multiple analyses of variance. Analysis of covariance was performed to determine the statistical significance between the case and control for each of the FD measurements and the associations with age, gender and their interaction. The interaction has been defined as study of simultaneous influence of diabetes and gender on FD variations.

7.3 Materials

Experiments were conducted in Department of the retina, Save Sight Centre hospital in Delhi. Approval for the project was granted by the HREC of RMIT University, Melbourne, Australia, and endorsed by Save Sight Centre hospital, in accordance with the declaration of Helsinki

(modified 2002). Informed consent was obtained from all participants who had responded to the request advertised in the 'Save Sight Centre' in Delhi. It was a prospective non-randomized study. The participants were classified in two groups; diabetes (case) type 2 and non-diabetes (control). Total of 232 optic disc centred retinal images were taken using Kowa Vx alpha camera (mydriatic and non-mydriatic retinal camera, Kowa, Japan) from both eyes. All photographs were taken in mydriatic mode, with original image resolution being 300dpi (4288×2848 pixels) and the angle of the photograph was 30^{o}. To save computation time, the images were cropped into Region of Interest (ROI) and resized to 729×485 pixels. Total of 43 images were excluded from the database due to insufficient quality (low vessel to background contrast inside the ROI) for assessment and FD measurement, leaving 189 (81%) for the analysis. Participants were defined to be diabetics (cases, n=23) by their physicians and based on fasting and post-prandial levels. All other matching subjects who were not diabetic were considered to be in the 'control' group (n=166). Participants with history of stroke, hypertension and cardiovascular disorder and other systemic diseases, with or without ocular manifestation, were not included in this study. In our database all 23 diabetic participants had none or very mild non-proliferative retinopathy. Matched participants were selected among a wide age range of 14 to 73 years for examining the association of FD change with age increase in the presence of diabetic retinopathy. Detailed demographic information of the participants has been summarized in Table 7.1.

Table 7.1 Demographic characteristics of patients recruited into the study

Demographic info.	**Mean (SD) or No***
Gender (Male/Female)	106/83
Diabetic/Non-diabetic	23/166
Age (years)	34.95(±14.61)
Weight (kg)	67.36(±16.02)
Height (cm)	164.34(±9.71)
Systolic Blood Pressure (mmHg)	126.87(±17.33)
Diastolic Blood Pressure (mmHg)	77.80(±14.54)

*Data are shown as Mean (±Standard deviation) or Number

7.4 Fractal Analysis

As the first step, the OD of the image is automatically detected using active contour model (Xu, Chutatape et al. 2007) on the RGB image. A circle is fitted to this boundary and the OD diameter

is obtained. A square shaped ROI corresponding to 4 OD diameter is obtained by cropping the image using a binary mask. Image enhancement was performed to compensate for a number of degrading artifacts and the removing the impairing effect which may have on the analysis outcome (Azemin, Kumar et al. 2011). Based on the previously proposed methods (Soares, Leandro et al. 2006; Azemin, Kumar et al. 2011), vascular network was extracted using directional matched filter (2D Gabor wavelet) for retinal image enhancement to extract the vascular network over different scales and equally spaced orientations. The class-conditional probability density function was computed to obtain enhanced gray scale posteriori images for analysis using the online "*mlvessel v1.3*" Matlab based software provided by Soares et al. (soares 2008). The image binarization was obtained by thresholding the gray scale posterior image.

Fractal dimension was obtained using three different estimation methods of, i) binary BC (chapter 2) ii) gray scale (differential) BC (chapter 2) and iii) Directional FD using Higuchi's method (FD-C in chapter 6.4). FD-C was calculated along a set of concentric circles (centred at OD centre) around the OD covering a region between OD boundary and a bounding circle of four OD diameters centered at OD center .

7.5 Statistical analysis

Statistical analyses were performed using Minitab 16 (Minitab Inc.). The data was first tested for normality by comparison between empirical cumulative distribution function of the data with expected normal distribution (Anderson-Darling, $p=0.260$). Multiple ANOVA analyses were performed to test the relationship between retinal vascular fractal dimension as response variable with diabetes and gender factor. The association of FD variations with gender in the presence of diabetic retinopathies and their corresponding interaction effects was studied using analysis of covariance. Participants' characteristic also reported by retinal image FD quartiles for the most two effective FD techniques reflecting significant association with diabetes (Higuchi's and gray scale BC). Independent age-specific analysis was also performed and the association of aging with diabetes factor and average FD variations was examined for each individual measurement. The age was subdivided into groups of 5-years intervals and the mean FD values were obtained for each group. Multivariate logistic regression analysis was performed to model the association

between the independent variables showing significant statistical association with diabetes ($P<0.05$) and diabetes as dependant variable after adjusting for potential confounding factors.

Also Linear regression analysis was performed to find the best fitting line to the data and estimate the rising/falling behavior of the FD trend with respect to age increase based on the slope of the regression line. Prevalence of diabetic cases in each age group was obtained and plotted for visual estimation of the balance of data with respect to age and its relationship to FD variation trend.

7.6 Results

Table 7.2 shows that there is a significant difference in the mean value of Higuchi's FD (P=0.005) and gray scale BC (P<0.001) of retinal vasculature between people with diabetes and without diabetes when not matched for gender and age. The average FD-C for participants with diabetes was found higher than those without diabetes for both Higuchi's (mean (SD) of the cases = 1.9625 (0.0027), control group=1.9541 (0.0010)) and gray scale BC (cases = 2.4403 (0.0034), control group=2.4227 (0.0012)). Binary BC did not show any significant relationship (P=0.082) with the mean value of 1.67 for both groups. Figure 7.1 shows two examples of retinal images with low and high FD-C values, corresponding to normal and diabetic patients with non-proliferative retinopathy, respectively.

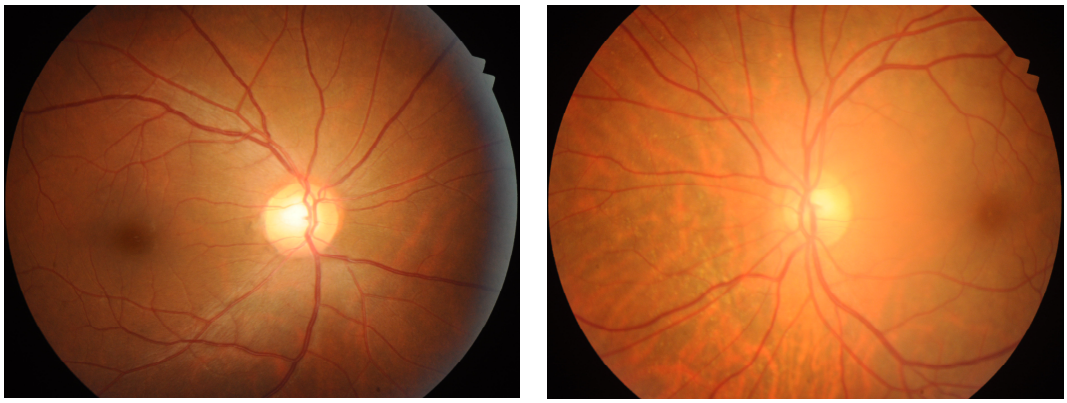

(a) (b)

Figure 7.1 Example of retinal images corresponding to normal and diabetic patients with none-proliferative diabetic retinopathy with low and high FD-C value respectively. (a) normal, FD-C=1.903 (b) Diabetic, FD-C=1.974

Table 7.3 shows the result from gender based analysis to examine whether there is any relationship between this factor and the FD quantification techniques. the result indicate a significant association of binary and gray scale BCs with the gender, irrespective of the subjects being diabetic or healthy (p= 0.023 and 0.001 respectively) while the Higuchi's FD was not significantly affected by gender (p= 0.621).Male had significantly higher FD values in the presence of diabetic retinopathies compared to females for both binary (males = 1.6800 (0.0033), females =1.6694 (0.0032)) and gray scale (males =2.4375 (0.0026), females =2.4255 (0.0025)) BCs. From these results, it is observed that there is no significant change in the values of Higuchi's FD showing no bias against the gender for this FD method, however, an inverse trend was observed for the Higuchi's FD with slightly lower values for the males (males=1.9576 (0.0020), females=1.9591 (0.0020)).

Interaction between diabetic retinopathy and gender has been examined with adjusting the data for gender (Table 7.4). While Higuchi's FD showed a significant interaction (p=0.033); no significant interaction was observed for the binary (P=0.144) and gray scale (P=0.052) BCs considering α=0.05, however, overall result showed greater FD values for diabetic cases compared to controls for both men and women. According to Higuchi's, males without diabetes had in average higher FD value (1.9566(0.0013), 95%CI 1.9539 to 1.9592) compared to females within the same category of no diabetes (1.9517 (0.0015), 95% CI 1.9486 to 1.9548) however, this trend was opposite for the cases showing grater mean value for females (1.9664 (0.0037),

95% CI 1.9589 to 1.9739) than the males (1.9587 (0.0039), 95% CI 1.9509 to 1.9665).The characteristics of our study population by fractal dimension quartiles are shown in Table 7.5. Binary BC was ignored as no significant relationship was found between FD and diabetic retinopathy in earlier analyses. Average BMI was similar across all the quartiles for both measurement techniques however, an increase in systolic and diastolic blood pressure (10 mmHg) was observed in the last two quartiles. The prevalence of diabetes was higher in the last quartiles for both FDs followed by the third and second representing milder ETRDS level (Early Treatment Diabetic Retinopathy Study).

Table 7.2 Relationship between retinal vascular fractal dimension and type 2 diabetes

Diabetes	n	Higuchi's FD P=0.005		Box-counting FD (Binary) P=0.082		Box-counting FD (Gray Scale) P=<0.001	
		Mean (SD)	95% CI	Mean (SD)	95% CI	Mean (SD)	95% CI
No	166	1.9541 (0.0010)	1.9521 to 1.9562	1.6707 (0.0016)	1.6675 to 1.6739	2.4227 (0.0012)	2.4201 to 2.4252
Yes	23	1.9625 (0.0027)	1.9571 to 1.9680	1.6788 (0.0043)	1.6702 to 1.6873	2.4403 (0.0034)	2.4335 to 2.4471

Table 7.3 Relationship between retinal vascular fractal dimension and gender

Gender	n	Higuchi's FD P=0.621		Box-counting FD (Binary) P=0.023		Box-counting FD (Gray Scale) P=0.001	
		Mean (SD)	95% CI	Mean (SD)	95% CI	Mean (SD)	95% CI
Female	83	1.9591 (0.0020)	1.9550 to 1.9631	1.6694 (0.0032)	1.6630 to 1.6758	2.4255 (0.0025)	2.4204 to 2.4306
Male	106	1.9576 (0.0020)	1.9535 to 1.9617	1.6800 (0.0033)	1.6735 to 1.6865	2.4375 (0.0026)	2.4323 to 2.4427

Table 7.4 Interaction between Diabetes and Gender

Diabetes	Gender	n	Higuchi's FD P=0.033		Box-counting FD (Binary) P=0.144		Box-counting FD (Gray Scale) P=0.052	
			Mean (SD)	95% CI	Mean (SD)	95% CI	Mean (SD)	95% CI
No	Female	71	1.9517 (0.0015)	1.9486 to 1.9548	1.6688 (0.0024)	1.6639 to 1.6736	2.4203 (0.0019)	2.4164 to 2.4242
	Male	95	1.9566 (0.0013)	1.9539 to 1.9592	1.6726 (0.0021)	1.6684 to 1.6768	2.4251 (0.0016)	2.4217 to 2.4284
Yes	Female	12	1.9664 (0.0037)	1.9589 to 1.9739	1.6701 (0.0059)	1.6583 to 1.6819	2.4308 (0.0047)	2.4214 to 2.4402
	Male	11	1.9587 (0.0039)	1.9509 to 1.9665	1.6875 (0.0062)	1.6751 to 1.6998	2.4499 (0.0049)	2.4401 to 2.4598

Table 7.5 Participant characteristics by retinal image FD quartiles

Characteristics	Higuchi's FD (FD-C)				Gray scale Box-counting FD			
	1St Quartile ≤1.9459	2nd Quartile 1.9462-1.9562	3rd Quartile 1.9564-1.9651	4th Quartile ≥1.9654	1St Quartile ≤2.4125	2nd Quartile 2.4126-2.4215	3rd Quartile 2.4217-2.4358	4th Quartile ≥2.4364
n	47	47	47	48	47	47	47	48
Male/Female	21/26	25/22	28/19	32/16	24/23	26/21	22/25	34/14
Age (years)	31 (21.5-45)	30 (22.5-47)	30 (22-43.5)	36 (25-53.5)	25 (20.5-31.5)	27 (22-43)	34 (23.5-47.5)	45 (29.5-55)
BMI (Kg/m^2)	23.80 (19.10-28.15)	25.09 (21.79-29.39)	24.16 (20.67-27.96)	24.76 (21.30-28.44)	24.30 (20.83-28.13)	24.76 (20.56-28.56)	23.63 (19.69-28.29)	24.91 (22.03-28.93)
Systolic Blood Pressure (mmHg)	120 (110-125)	120 (117.5-140)	130 (117.5-140)	130 (120-140)	120 (110-140)	120 (110-130)	130 (120-135)	130 (120-140)
Diastolic Blood Pressure	70 (65-80)	80 (70-80)	80 (70-80)	80 (73.75-90)	75 (70-80)	70 (70-80)	80 (70-85)	80 (70-90)
Prevalence (%)	4.34	26.09	26.09	43.48	8.7	8.7	17.38	65.22

Figure 7.2 shows how the age distribution affects the fractal dimension in the presence of diabetic retinopathies. Histogram of diabetes distribution across different age groups has also been demonstrated for comparison. According to this plot, the best linear fit for the Higuchi's has slope of zero with respect to age increase (P=0.681) showing its insensitivity to this factor while the balance of diabetic population is leant towards the older age group. The regression line for the two BC techniques (Gray scale: P=0.072, Binary P=0.028) had a positive slope representing an increase in FD with age increase which is not due to the diabetic signs. As in our database, most of the diabetic cases were among the older population, the statistical significance of gray scale BC in differentiating cases from control is biased towards the confounding age factor. Table 7.5 also verifies that the mean age across all the quartiles were similar for the Higuchi's FD.

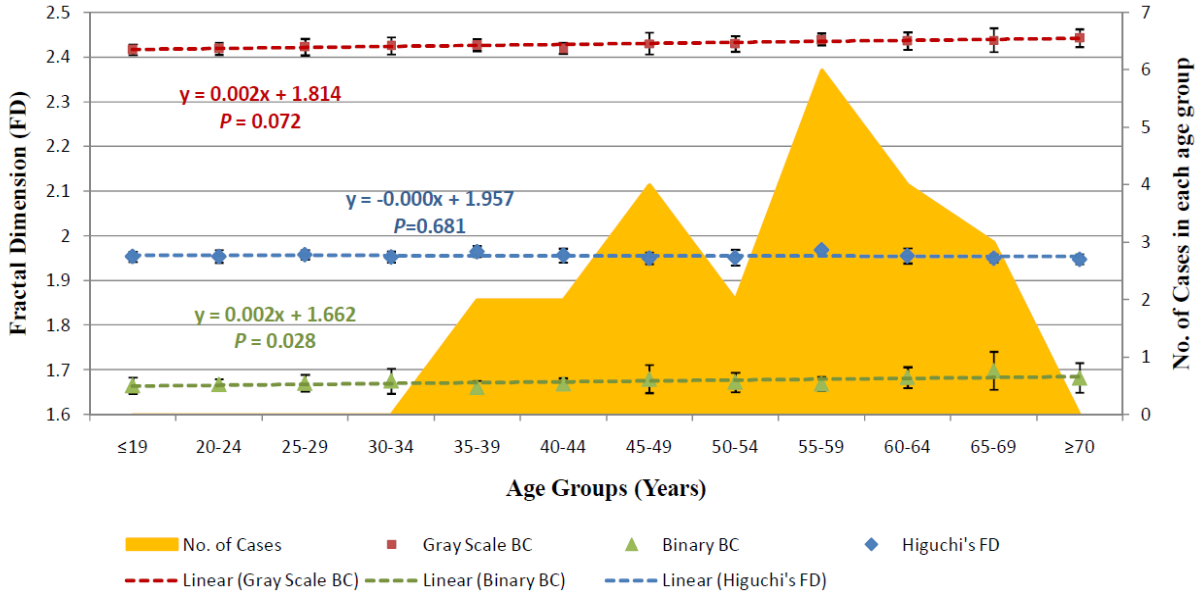

Figure 7.2: Association of FD variations with the age factor in the presence of diabetes incidence. *P*-values relate to trend across age groups. Prevalence of diabetic cases with in each age group (yellow) has been shown for comparison.

Table 7.6 shows the result from multivariate logistic regression analysis including the estimated coefficients and standard error of the model fitted to the independent variables of age ($p=0.003$), Higuchi's FD ($p=0.005$) and Gray scale Box-counting FD ($p<0.001$). *P_values* of <0.001 and 0.010 for age and Higuchi's FD indicate that they can be used as strong predictor of diabetes, however, $p=0.077$ corresponding to Grayscale FD indicate that there is insufficient evidence to conclude that a change in Gray-scale FD can be used as predictor of mild non-proliferative diabetic retinopathy. The classification performance using this model was evaluated by Receivers Operating Characteristic analysis and calculating the area under the curve (AUC) which resulted into AUC of 0.906 with SD and 95% CI of 0.042 and [0.855 to 0.943] respectively.

Table 7.6 Logistic regression analysis

Variable	Coefficient	SD	P	Odds Ratio	95% CI
Age	0.1025	0.02324	<0.001	1.1080	1.0587 to 1.1596
Higuchi's FD	63.2078	24.5861	0.010	2.82E+027	3.33 E+06 to 2.39E+48
Gray-Scale FD	29.0413	16.4687	0.077	4.10E+012	0.0393 to 427E+024
Constant	-200.8555	-	-	-	-

7.7 Discussion

This work demonstrates that gray scale FD of the retinal vasculature can be used to better identify people with type 2 diabetes compared to the binary method. This is in agreement with loss of vessel calibre information in the segmentation and binarization process (Che Azemin, Kumar et al. 2012). This relationship between the changes in the retinal vasculature calibre with diabetes has been recognized by many researchers (Klein, Klein et al. 2004; Kifley, Wang et al. 2007; Nguyen, Wang et al. 2008). Thus, gray scale FD analysis of retinal images can preserve the information associated with additional line of diagnosing diabetic patients and if it is age independent it can be applied to a wider age range. With an increasing number of young people who are suffering from diabetes, such options are opportunistic as often the younger cohort does not get regular medical blood tests, but are more likely to go to get their eyes tested.

Except diameter change, the presence of microaneurysms among the diabetic subjects has also been observed by other researchers. However, these measurement techniques require manual observations or supervision, and are not suitable for automated analysis. Fractal dimension (FD) of the eye fundus images have been studied by researchers and the relationship between FD and hypertension (Klein, Klein et al. 2006), and age (Azemin, Kumar et al. 2011; Azemin, Kumar et al. 2012) has been established. However, this work has shown that the commonly used box-counting FD is unsuitable for differentiating between Mild NPDR and healthy subjects.

This study has demonstrated that increase in FD of retinal vasculature is strongly associated with retinopathy signs in type 2 diabetes, in agreement with other studies (Shu-Chen and Yueh-Min 2003; Yau, Kawasaki et al. 2010) and for Higuchi's FD this trend is independent of the age factor. This study observed increased average FD in older people compared to the younger adults

(Table 7.5) but with no significant association between FD and age factor, however, an inverse association of FD variation with aging has been reported elsewhere in literatures corresponding to healthy subjects (Azemin, Kumar et al. 2012). This indicates greater influence of diabetes on complexity of retinal vascular pattern compared to the age factor. In other words the increase in FD due to diabetes is dominating the reducing effect of aging in FD values for both age dependant techniques (binary and gray scale BC). Similar results have been observed from Table 7.5 for the blood pressure factor which may be incorrectly interpreted as association of elevated blood pressure with increased FD values, however, in this subset, subjects with slightly higher average blood pressure had higher prevalence of diabetic retinopathies without showing any significant association. Therefore, association of increase FD with older age and elevated blood pressure cannot be interpreted form the table.

Also According to Table 7.3, this study has found no significant association between Higuchi's by circular image intensity scanning and gender, this would make it a convenient FD method for retinal image assessment without being concerned about confounding effect of gender and age factor on the analysis outcome.

7.8 Summary

This research reports the success in gray scale fractal measure of diabetic retinal images and application of Higuchi's FD for the first time in automatic retinal image analysis. The work shows that the difference between the diabetic and control subjects was statistically significant for both Higuchi's FD with circular scanning around OD and gray scale BC. The findings suggest increase in FD of retinal vasculature is strongly associated with NPDR signs in type 2 diabetes and for Higuchi's FD this trend is independent of the age factor. The proposed analysis based on the use of Higuchi's FD by circular image intensity scanning has the advantage of obtaining the FD in a specific bounding region around the OD in the eye-fundus image with respect to OD diameter. In future, the technique can find application in more disease analyses including stroke and hypertension.

Chapter 8

Effect of retinal vessel pulsation on diameter and calibre specific FD variations

8.1 Introduction

Studies have revealed the existence of pulsatile motions in retinal vascular geometry, especially vessel diameter variations across the cardiac cycle (Chen, Patel et al. 1994; Levine 1998; Gugleta, Kochkorov et al. 2006; Moret, Poloschek et al. 2011). However, the effect of these pulatile motions on FD estimation and their significance level with respect to a specific region of retina has never been investigated. This chapter studies the significance in variation of region based FD of retinal images due to microvascular pulsations to address the question of whether the pulsation would affect the retinal image analysis when used for risk assessments. Unlike chapter's 6 and 7 in which vessel caliber variation has been referred to as feature due to a disease condition, in this chapter, definition of vessel diameter variations corresponds to geometrical changes as a result of cardiac cyclic pulsations. Therefore, this chapter proceeds by providing a background about retinal vessel pulsation followed by introduction and validation of a new methodology for pulsation visualization using a sequence of ECG synchronized retinal images. The visualization was required to validate the database in terms of the existence of pulsatile features corresponding to cardiac cycle, prior to FD analysis. This is then followed by region based analysis of FD at certain number of cardiac cycle points according to the zone definitions in chapter 6.4.2.

8.2 Background

This pulsatility is expected as a result of change in blood volumetric flow entering the ophthalmic vascular system under certain level of intra-ocular pressure during the peak-systole and diastolic phase of cardiac cycle which can be served as a potential feature to rule out some

clinical signs. An example of pulsative property observable from the retina is the spontaneous venous pulsation (SVP), which is available in approximately 90% of the patients (Levine 1998; Jacks and Miller 2003). It is caused by variation in the pressure gradient between the intraocular retinal veins and the retrolaminar portion of the central retinal vein (CRV)(Lascaratos, Ahmed et al. 2010), visible as rhythmic changes in diameter of one or more veins near or on the optic nerve head. Its clinical relevance is for differentiating early papoilledema from pseudopapoilledema, detection of elevated intracranial pressure (≥14 mmHg) and other pathological conditions (Moret, Poloschek et al. 2011). In addition to SVP, pulsation of veins outside the optic disk (OD), such as the serpentine movement of principal arteries, pulsatile motion of small arterioles and movement of optic nerve head are other existing pulsatile features that can be visualized with the help of dynamic fundoscopy (Moret, Poloschek et al. 2011).

A number of studies have quantified the pulsatile changes and reported their potential influence on the certain parameters frequently measured for clinical applications. Chen et al. (Chen, Patel et al. 1994) studied monochromatic fundus photographs taken in eight arbitrary parts of the cardiac cycle and found a maximum change of 4.82% for the retinal venous diameter between early systole and early diastole (p=0.03) and an increase of 3.46% (p=0.01) in arterial diameter in mid-late systole. Hao et al. (Hao, Sasongko et al. 2012) in a similar study reported a maximum variation of 4.1% in diameter, 1.5% in tortuosity, 3.5% in branching angle, and 2% in Length-Diameter Ratio (LDR). In this study, the variation of individual vessel diameter (excluding vessel summary diameter) was found to be statistically significant (P<0.001), however, the influence of pulsation on other parameters was reported as insignificant (all P-values > 0.1).

While previous studies have investigated the effect of retinal vessel pulsations on the diameter and other geometry variations (e.g. tortuosity, branching angle and …) (Chen, Patel et al. 1994; Moret, Poloschek et al. 2011; Hao, Sasongko et al. 2012), the potential change in fractal dimension (FD), as one the global measure of retinal microvasculature structure, frequently used for diagnostic purpose has never been investigated. This work studies the effect of changes in retinal vascular geometry (vessel pulsation) on the variations of FD (specifically the proposed caliber specific FD) during normal cardiac cycle by application of a novel pulsation visualization technique for database validation.

8.3 Dynamic fundoscopy techniques

8.3.1 Techniques used by literatures

The need for dynamic assessment of the variation in retinal microcirculatory system has led to development of Dynamic Vessel Analyser (DVA) (Vilser, Nagel et al. 2002) which is able to study the blood flow in the retinal vasculture and observe the vessel diameters as a function of time in a live video. It provides high resolution images with sampling rate of greater than 20 frames per second, however only limited segment of individual arteriole and venule can be measured and the methodology is suitable for highly specialised facilities. DVA requires pupil dilation and flickering light stimulation which may influence the eye vasculature resulting in incorrect observations(Garhofer, Bek et al. 2010). The reliability and reproducibility of flicker responses is questionable and there are questions regarding possible increase in the retinal vessel diameter, retinal blood flow and optic nerve head blood flow in response to the flicker stimulation (Garhofer, Bek et al. 2010).

The alternative to the DVA is to modify the static fundus camera such that it can be used for assessment of dynamic changes. Chen et al. (Chen, Patel et al. 1994) used monochromic red-free photographs taken with a fundus camera synchronized with electrocardiogram (ECG) and suffered from random selection of the points showing pulsatile features. Moret et al. (Moret, Poloschek et al. 2011) applied principal component analysis (PCA) to an image sequence acquired by a confocal scanning laser optholmoscope (CSLO) equipped with near infrared CCD camera to capture video. However, as no synchronization was performed with ECG, the movies turned out to start and stop at different phases with respect to cardiac cycle and required manual trimming to avoid discontinuities when looping the image sequence.

8.3.2 Image acquisition technique used in this study

In order to avoid the phase shift with respect to ECG QRS peak and obtain high resolution images, this study has taken advantage of a novel technique based on ECG synchronization of the fundus camera. The acquisition system was built by a colleague (Mr. Hao Hao) and data

collection was performed jointly at RMIT University Biosignal Laboratory. Block diagram of this system has been shown in Figure 8.1. The system was equipped with standard custom made three-lead ECG monitoring system for real-time monitoring of the heart rate. The ECG signal was pre-processed for noise reduction and for real-time detection of the R-R intervals. The ECG monitoring system was electronically connected with the trigger mechanism of a Cannon CR-1 non-mydriatic digital fundus camera equipped with a 15.1 mega pixel Cannon EOS 50D. The system generated an adjustable trigger pulse at a designated point with respect to the R peak. The shutter delays were tested and found to be consistent and thus were ignored, as this was very small compared with the R-R interval. The ECG monitoring system monitored the R-R interval and triggered an alarm for the examiner if the interval changed more than 10% from the start, because this would lead to erroneous trigger points.

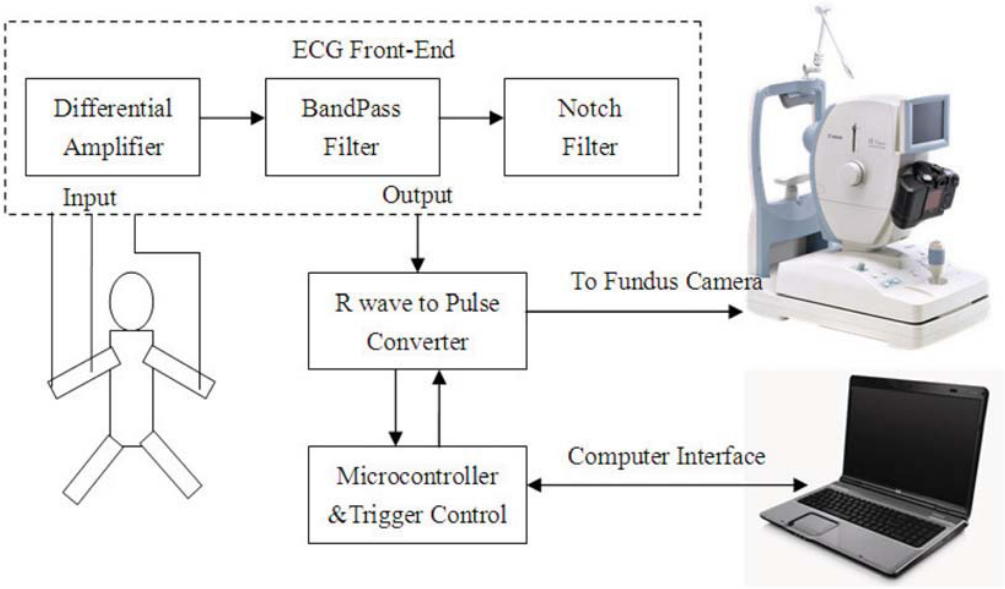

Figure 8.1 Block diagram of the ECG synchronized retinal photography system (Hao, Sasongko et al. 2012)

In this study the R-R interval was divided into eight identical sub-intervals and a time-delay triggering switch trigged the shutter at nine equally spaced points (Figure 8.2). Total number of nine images was taken from the left eye of each person. The cardiac cycle was divided into eight equal length segments based on the works reported by Chen et al. (Chen, Patel et al. 1994), Moret *et al*.(Moret, Poloschek et al. 2011) and Hao et al.(Hao, Sasongko et al. 2012) However,

this technique allows for the sampling rate to be changed to any reasonable value and may be used at a higher rate. The first image was taken at R peak, the 2nd was captured after a delay of 1/8 R-R interval, while the 8th photograph coincided with the 7/8 R-R interval. 9th image corresponded to the subsequent QRS peak and was assumed to be similar to the 1St image, therefore it was analysed in this work. All the images were optic disc cantered, in RGB format and of size 4752×3168 pixels.

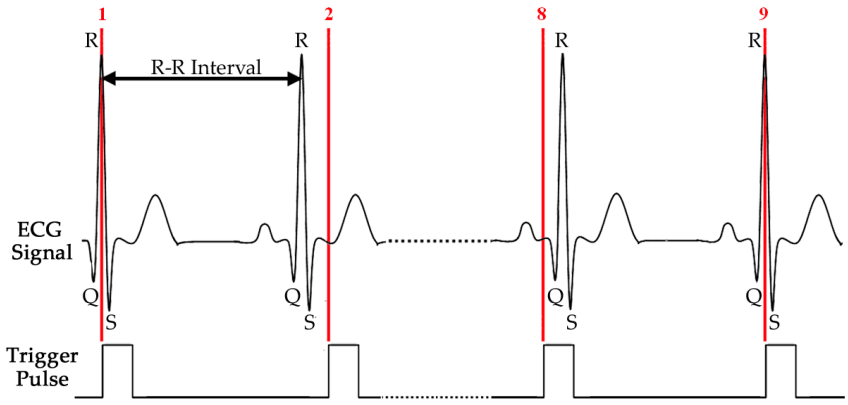

Figure 8.2 Eight distinct points with respect to QRS peak where the images were captured. Illustration of the trigger pulse and ECG signal at points 1, 2 (1/8 R-R interval time delay) and 8 (7/8 R-R interval time delay). 9th image coincides with the next QRS peak.

8.4 Pre-processing

8.4.1 Image alignment

During the experiment, there can be some movement of the eye leading to a relative displacement of the retinal vessels between different images. Preliminary experiments showed that this movement was comparable with the caliber pulsation and this would result in error when determining the movement due to pulsation. To remove this error, the images have to be aligned which will generate retinal image sequence free of eye movement. This will improve the visibility of pulsatile motion in retinal vasculature.

Image alignment was performed using i2k Align Retina software (i2k Retina®, DualAlignTM) based on Dual-Bootstrap algorithm (Stewart, Tsai et al. 2003) to correct for the translational and rotational eye drift and ensure any measurement to be performed at the same spatial location. To save the computation time, the images were down sampled by a factor of two before they were fed into the registration software. Due to providing better contrast visibility (Li, Hsu et al. 2003), only the green channel was used in the alignment process. The aligned images were cropped to 576×1274 pixels, centering around OD which was found to be sufficient to observe all the pulsatile effects in the retinal images of the twelve subjects (Figure 8.3.a).

8.4.2 Filtering and edge enhancement

Images may be corrupted by noise during acquisition due to numerous reasons such as the camera hardware, examiner error (for example focusing), and illuminations issues (Sable and Jondhale 2010). Non-uniform illumination was corrected using a median filtering technique (Chrástek, Wolf et al. 2005). A mask of size 31×31 pixels was created to be greater than the largest vessel diameter. A set of correction coefficients was calculated and multiplied by the green channel of the original image to obtain the corrected version. The coefficients were obtained by dividing the maximum gray-scale values of the filtered image by the intensity of each pixel on the same image (median filtered).

The bilateral filter proposed by Tomasi et al.(Tomasi and Manduchi 1998) was used for vessel edge enhancement and to reduce noise without sacrificing the contrast. It is a non-linear filter that averages the intensity values using a set of weights, which are inversely related to the intensity similarities. For mathematical formulation and details of this filter, please see Tomasi (Tomasi and Manduchi 1998). Traditional filtering and noise reduction methods such as Gaussian low-pass filtering use weighted average of pixel values in the neighborhood and consider the spatial variation to be slow (Tomasi and Manduchi 1998). This is based on the assumption that neighborhood pixels have similar intensity values and therefore it is appropriate to average the pixels within a small neighborhood. However, this assumption is incorrect at the edges and the low-pass filtering results in blurring the edges. This blurring is not acceptable

because this would reduce the contrast at the vessel boundaries and impairs the visualization of pulsation.

8.4.3 Extraction of vesselness map image

Initial segmentation was required to build a vesselness map corresponding to edges. The boundaries were enhanced by the scale-space analysis (Martínez-Pérez, Hughes et al. 1999) using the vector sum of image Hessian matrix eigenvectors and the gradient magnitude of the orientation matrix, as explained in section 3.2 (Figure 8.3.b).

To eliminate the background noise, a binary mask was created to separate retinal vasculature from the background pattern on the vesselness map, using two dimensional Gabor wavelet segmentation with supervised classification method proposed by Soares et al. (Soares, Leandro et al. 2006) as in section 5.3.2 (Figure 8.3.c**)**. Prior to the application of the mask, it was corrected for any discontinuities and noise, generated due to the segmentation process. A set of morphological operations was applied to the segmented image for removing the noise and isolated pixels from the background and vessel enlargement. The first step was to consider isolated 1's as speckle and remove any individual 1's surrounded by 0's because an edge always has adjoining transition points. The next step was the generation of the mask for five consecutive dilations with a 3×3 structuring element matrix to improve the visibility of the vessels (Figure 8.3.d). The details of these morphological operations are available in González (González and Woods 2008). The vesselness maps were multiplied into the mask to generate the final image set (Figure 8.3.e).

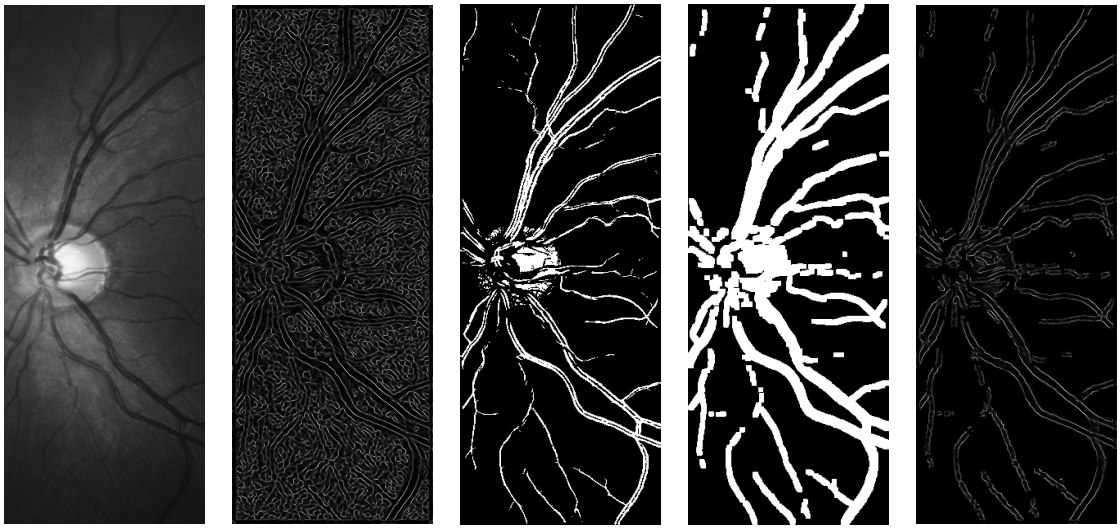

(a) **(b)** **(c)** **(d)** **(e)**

Figure 8.3 presentation of processing outcomes at each step before image sequence generation a) Original image (the green channel) b) vesselness image map obtained by scale space analysis c) result of 2D Gabor filtering and image segmentation d) the mask generated by a set of morphological operations (opening followed by five consecutive dilations) e) the masked vesselness image with highlighted boundaries and the main blood vessels.

8.4.4 Image sequence generation

In order to visualize the pulsatile changes, a video for each subject was generated from the masked images obtained in 8.4.3. The eight images of each subject were placed serially and displayed for 125ms and rendered to match the standard 30 frames per second format for optimal real-time playback. These were looped fifty times to obtain approximately one minute playback video for validating the proposed "Vesselness Mapping of Retinal image Sequence" (VMRS) against the state of the art PCA method (Moret, Poloschek et al. 2011).

8.5 Subjects

39 healthy volunteers (22 men and 17 women) aged 20 – 49 years (mean 36 years) were recruited to participate in the study of caliber specific Higuchi's FD and analysis of its association with cardiac cyclic vessel diameter pulsation. The participants were made to rest for

15 minute prior to the experiment to ensure stable haemodynamic condition. After the participants were rested, their blood pressure and pulse rate were recorded using a digital sphygmomanometer. The mean (SD) systolic and diastolic pressures of all the participants were obtained: 124.73 (16.58) and 75.39 (9.72) mmHg respectively with pulse-per minute rate of 74.84 (11.70). The study was approved by the RMIT Research Ethics Committee and conducted in accordance with Declaration of Helsinki of 1975, as revised in 2004. The exclusion criteria were (i) prescribed or other medication on the day of the experiment, (ii) hypertension, (iii) history of cardiovascular disease, (iv) diabetes, (v) eye disease and (vi) history of eye surgery. The participant were explained the project purpose, procedures, risks, discomforts, and the duration of the test. This was done in writing and orally. The issues regarding confidentiality and privacy of the data, and their rights, especially regarding stopping the experiment without notice or explanations, were also discussed. Each participant signed the informed consent form prior to the experiment where they authorized the investigators to record their retina image and use these images for research and publication purposes without requiring any further permission from the participants.

Out of these 39 healthy volunteers, 12 subjects (9 men and 3 women) with average age of 36 (ranged 21 to 56) were randomly selected for validation of the VMRS and detailed investigation of pulsatile features by two independent ophthalmologists. The mean (SD) systolic and diastolic pressures of the selected subjects were obtained as 124.27 (8.85) and 73.63 (7.31) mmHg respectively with pulse (per minute) rate of 73.36 (11.26).

8.6 Validation of VMRS

8.6.1 Visualization of pulsatile motions

The VMRS technique was validated by comparing it against the current state of the art, PCA method (Moret, Poloschek et al. 2011) in terms of the number of observed pulsatile features in the region of interest (ROI) and qualitative assessment by two independent graders. The ROI was selected by placing a mask of concentric circles on each frame with the smallest one matching the OD boundary. The circles divided the regions around the OD into four different zones; A, B,

C and greater than C with respect to OD diameter according to the definition in chapter 6.4.2 as shown in Figure 8.4.

Two independent grading experts examined all the videos and counted the number of segments in each zone showing pulsatile properties. To compare the VMRS technique with the PCA method, the seven region-based features defined by Moret et al (Moret, Poloschek et al. 2011) were measured by the graders. These features are; Spontaneous Venous Pulsations (SVP) inside the OD and in Zone A, Venous Pulsation in zone B (VP_B), Venous Pulsation in zone C and beyond (VP_C), Arteriolar Pulsation in zone A (AP_A), Arteriolar Pulsation in zone B (AP_B), Arteriolar Pulsation in zone C and beyond (AP_C), Serpentine Movements and mechanical coupling between the vessels (SM). The graders were also asked to mark each video on a scale of ten with '10' corresponding to best quality and '1' to the poorest and their inability to observe any pulsation in the video due to quality.

8.6.2 Measurement of individual vessel diameter change for trend estimation

Trend estimation for diameter variation was performed for comparative purpose and validating the VMRS against other studies (Chen, Patel et al. 1994; Hao, Sasongko et al. 2012) . A program was written in MATLAB (The Matworks, Inc, R2009a) to measure the vessel diameter corresponding to pulsatile changes. In the first frame of the recording, a seed point was identified by the grader for vessel edge tracking purpose, similar to the process used by DVA. The grader specified an ROI on the vesselness image map (Figure 8.3.e) by clicking one point around the approximate location of each vessel boundary and specifying the start and end points of the segment that was to be measured. Subsequently, the software automatically tracked the vessel edges using similar methodology explained in chapter 3.2.2. Once the edges were identified, the points on the tracked boundaries corresponding to the two edges of the vessels were paired based on the shortest Euclidean distance (Figure 8.5). The length of the segment and number of cross-sections were grader selectable, ranging from single cross-section to measuring over the entire observable length. The diameter of the vessel was defined as average length of the cross sectional lines (Al-Diri, Hunter et al. 2009; Bhuiyan, Nath et al. 2009; Bhuiyan, Kawasaki et al.

2010) within the selected segment. The above process was perfumed only on the first frame and automatically replicated for all the other frames while maintaining the same seed points. The above process was repeated for different vessel segments to increase the number of measured segments.

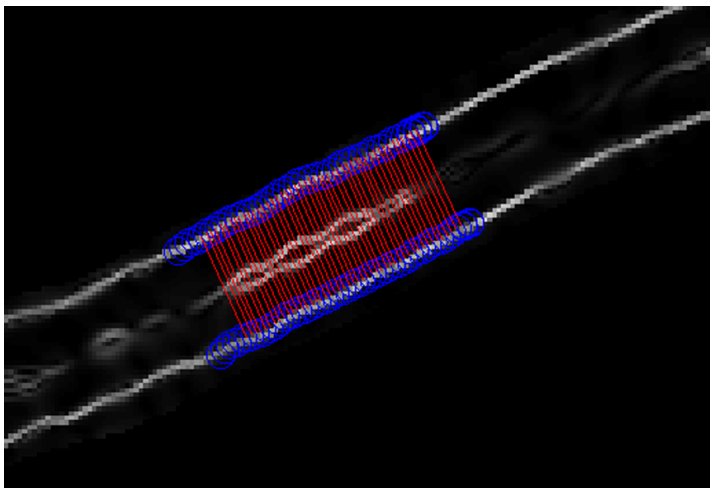

Figure 8.4: Boundary tracking of a sample vessel segment using the masked vesselness image with highlighted boundaries. The blue circles are the tracked boundaries and the red lines are the shortest Euclidean distance between the two boundaries. The average length of these lines are considered as the diameter of the vessel segment on the selected ROI.

To determine the vessel diameters in micrometer (μm) and adjust the measured values for different image resolutions, digital and optical magnifications (Pakter, Fuchs et al. 2011) a calibration factor was computed as "the ratio of micrometers per pixel in a definite length of a digitized image of the eye fundus" (Pakter, Fuchs et al. 2011). The distance between the OD center and macula center was considered as the fixed length and was assumed to be 4500 μm which is equivalent to 2.5 times the average OD diameter (1800 μm) reported by Jonas et al. (Jonas, Gusek et al. 1988) and Pakter et al. (Pakter, Fuchs et al. 2011). The average distance between the OD center and macula center was obtained based on two expert graders and was found to be 569 pixels averaged over the entire database. Therefore, the calibration factor was obtained as the ratio of 4500/569.1= 7.90 μm/pixel.

In the first experiment, only the first frame was demonstrated to the grader and the diameter was measured without seeing the pulsating vessels. In the second experiment, the grader used the video to locate the vessels that were pulsating prior to the caliber measurement. In each experiment the trends for 35 arterioles and 35 venules were obtained among all the 12 subjects and averaged at each cardiac cycle point to gain a single waveform corresponding to the vessel type. However, there is a potential location based phase shift between different measuring sites on retinal vessels with respect to OD(Gugleta, Kochkorov et al. 2006) which would affect the summary diameter estimation. To remove the effect of the difference in the phase delay due to the distance from the OD, the estimated inter-subject and intra-subject trends were aligned together using Dynamic Time Warp (DTW) analysis(Ao 2010), a widely accepted technique for obtaining an optimal alignment between two time dependant sequences. The details of this process is provided in a book by Ao SI (Ao 2010).

8.7 Variations of caliber specific FD across cardiac cycle

Two different FD methods (FDC and FD_{BC}) were compared to study the potential change in fractal properties of retinal vessel due to cardiac cycle variations. Only zones A and B were tested as the major pulsations more often happen in these two regions (Moret, Poloschek et al. 2011). The caliber specific FD (FDC) in each zone was obtained as the average of the individual FD values measured on circular paths centered at OD center using vessel enhanced images as explained in chapter 6.4.1. To calculate the FD_{BC} The vessel enhanced images were first converted into binary format by pixel-classification method using Bayesian classifier (Soares, Leandro et al. 2006). This method was known as the one providing highest classification performance with the area under the receiver operating characteristic curve of 0.9614 (Soares, Leandro et al. 2006) compared to manual segmentation. The choice of using this type of box-counting method (mono-fractal using binary images) was made due to its frequent employment in the literatures for disease analysis as an established method for FD quantification of the self-similar structures like retinal vasculature (Masters 2004; de Mendonca, de Amorim Garcia et al. 2007; Doubal, MacGillivray et al. 2010). In order to perform zone based box-counting the binary images were first masked by appropriate binary masks to keep a specific zone and filter out the

other regions as shown in Figure 8.5. The masks were made specifically for each subject according to the OD diameter measured for FDC calculation and zone selection (chapter 6.4.2). These images were then covered with the square boxes of decreasing side length size of L=1/512, 1/ 256, 1/128, …, 1 of the image side length and the number of boxes N(*L*) containing at least one white pixel were counted. The absolute value of the least squares regression slope of the plot of $\log_2$ N (*L*) versus $\log_2$ (*L)* was considered as FD_{BC}.

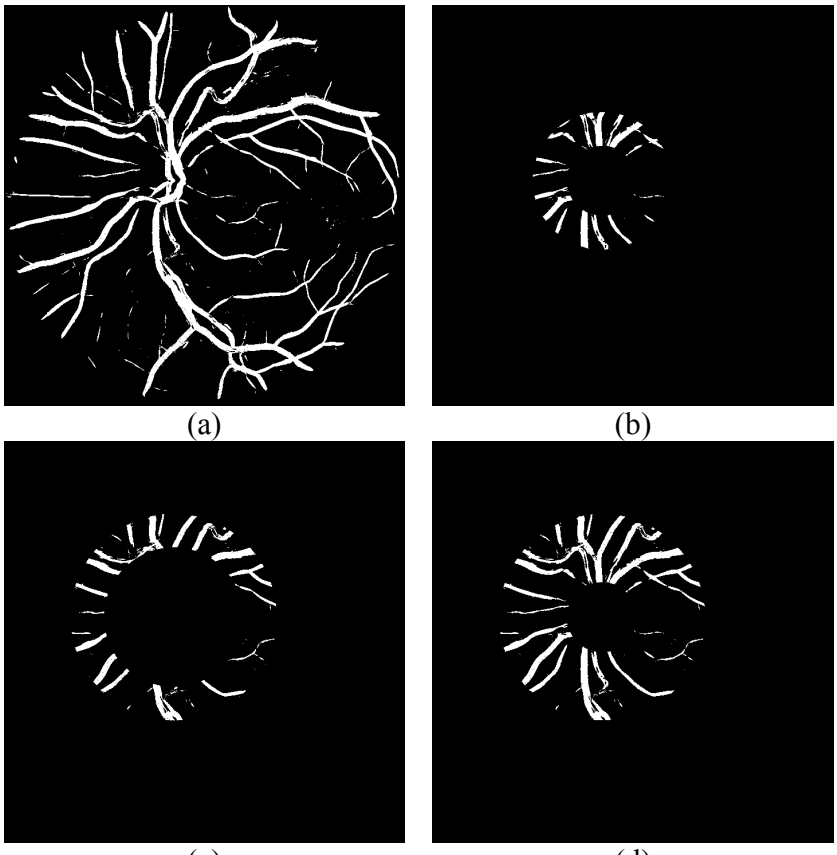

Figure 8.5 Masking of enhanced binerized retinal images for zone based FD_{BC} calculation. a) example of a complete enhanced and binerized retina image b) Zone A c) zone B d) zone A and B (AB)

8.8 Statistical analysis

Statistical analyses were performed using Minitab 16 (Minitab Inc.). The level of agreement between the two grader (inter-grader reliability) was tested using student t-test and correlation (Pearson's Correlation) analysis. For each measurement, the mean diameters across the cardiac

points were compared and overall *p*-value of the variations was obtained using ANOVA analysis with post-hoc multiple comparison tests. Two different sets of variations were calculated. In the first set, the average diameter at the first cardiac point was considered as the reference and the absolute value of the deviations from that point was found at other cardiac point. In the second set, the difference between the maximum and the minimum diameter was calculated to study the maximum change across a cardiac cycle with respect to the vessel type and the measurement method.

8.9 Results

8.9.1 Validation of VRMS technique

Table 8.1 shows a comparative of the visualization using PCA (Moret, Poloschek et al. 2011) and the VRMS technique. Column 1 corresponds to the video numbers (Subjects). The number of pulsating segments observed in each zone by the graders is presented in columns 2 to 31 and columns 32-35 show the scale-ten quality index for the both techniques as reported by two independent graders. The result from inter-grader reliability test for the proposed method suggested high correlation ($r=0.96$) and no statistical significant difference (p=0.972, 95% CI [-0.565, 0.586]). From Table 8.1, it is observed that there is a significant increase in the average number of pulsative segments when the visualization was performed using VMRS compared to PCA. The results also show that there is a significant improvement in the mean quality index, from 3 to 6.9.

Table 8.1 Pulsatile Features a. Spontaneous venous pulsation within one OD diameter from the center; b. venous pulsation in zone B; c. Venous pulsation in zone C and beyond; d. Arterial pulsation in zone A; e. Arterial pulsation in zone B; f. Arterial pulsation in zone C and beyond; g. Serpentine movements and mechanical coupling between arteries and veins; h. Quality of the observed features.

Subject No.	Pulsatile Features																										QOF [h]			
	SVP [a]				VP_B [b]				VP_C [c]				AP_A [d]				AP_B [e]				AP_C [f]				SM [g]							
	PCA		Proposed Method		PCA		Proposed Method		PCA		Proposed Method		PCA		Proposed Method		PCA		Proposed Method		PCA		Proposed Method		PCA		Proposed Method		PCA		Proposed Method	
	G1	G2	G1	G2	G1	G2	G1	G2	G1	G2	G1	G2	G1	G2	G1	G2	G1	G2	G1	G2	G1	G2	G1	G2	G1	G2	G1	G2	G1	G2	G1	G2
1	3	3	4	4	1	2	3	4	1	1	3	3	0	0	4	5	1	0	3	3	0	0	3	2	2	1	3	3	4	3	8	7
2	3	3	3	3	2	1	3	3	0	0	3	3	2	2	3	4	1	0	4	4	0	1	4	4	1	1	3	3	3	4	7	8
3	1	1	3	3	2	0	3	3	1	3	2	3	1	2	3	3	1	2	2	2	0	0	1	1	1	1	1	1	2	4	7	7
4	3	3	4	5	3	2	3	3	1	2	2	2	1	1	2	2	0	0	1	2	0	0	1	1	0	0	1	1	3	2	6	7
5	1	1	1	1	0	1	0	0	3	4	2	2	1	1	0	0	2	3	1	1	0	1	0	0	2	2	1	1	4	1	6	6
6	3	3	2	2	2	2	1	1	2	2	2	2	2	3	3	3	2	2	2	2	1	1	2	2	2	2	2	2	4	4	8	7
7	1	2	1	1	2	3	1	1	1	3	1	2	0	0	1	1	0	1	2	2	0	1	0	0	2	2	2	2	1	3	7	6
8	3	3	3	3	2	2	3	2	1	2	2	2	1	1	1	1	0	1	1	2	0	0	1	1	0	0	0	0	2	3	6	7
9	3	3	4	4	1	1	3	2	1	1	3	2	1	1	1	1	0	0	2	1	0	0	1	0	1	1	2	2	2	2	6	6
10	3	2	3	2	3	2	3	2	2	2	2	2	1	2	1	1	1	2	1	1	0	2	1	1	1	1	1	1	3	2	8	6
11	3	3	2	2	1	1	2	1	2	3	1	2	2	2	1	2	3	4	3	2	2	3	3	3	2	2	2	2	6	5	9	9
12	1	2	1	1	1	2	0	0	0	0	0	0	1	1	1	1	0	0	0	0	0	0	0	0	2	2	1	1	2	2	5	6
Average	2.3	2.4	2.6	2.6	1.7	1.6	2.1	1.8	1.3	1.9	1.9	2.1	1.1	1.3	1.8	2.0	0.9	1.3	1.8	1.8	0.3	0.8	1.4	1.3	1.3	1.3	1.6	1.6	3.0	2.9	6.9	6.8
Average of Two Graders	2.4		2.6		1.6		2.0		1.6		2.0		1.2		1.9		1.1		1.8		0.5		1.3		1.3		1.6		3.0		6.9	

Figure 8.6 shows the location of the different features in the detected pulsations in each zone for subject No 11. The following features at each numbered location have been marked; 1) SVP inside the optic disk, 2) vein diameter variation along the trunk or SVP if defining it within one OD diameter region, 3) arterial pulsation in zone A, 4) arterial pulsation in zone B, 5) vein diameter variation in zone B, 6) fine vessel pulsation, 7 & 8) serpentine movements, mechanical coupling between the vessels and pulsation and 9 to 12) diameter variation outside the zone C.

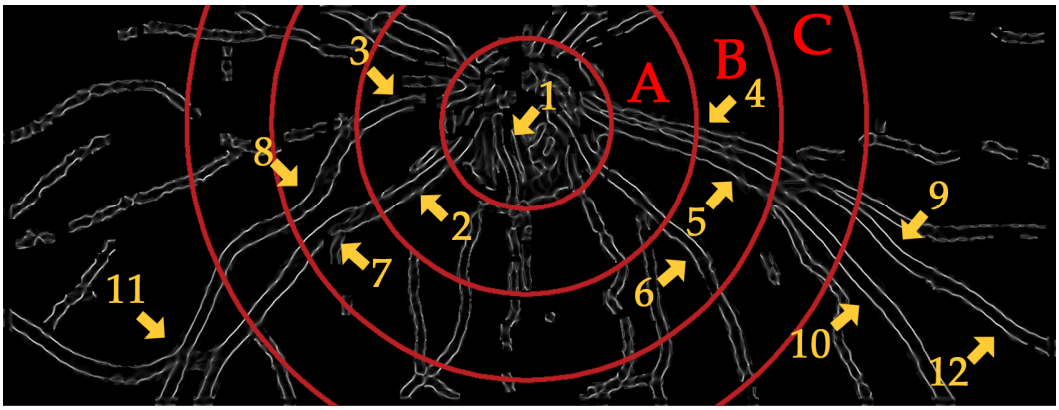

Figure 8.6 A frame from the rendered video for subject No.11 with concentric circles centered at the optic disk. The arrows point to 12 locations where the pulsation was clearly visible.

8.9.2 Vessel Diameter variation across cardiac cycle

The change of individual vessel caliber due to pulsation, measured without VMRS visualization, has been shown in Table 8.2. The results show that the average change in vessel diameter during the cardiac cycle was 1.2 μm for arteries and 1.6 μm for the veins. The statistical analysis showed no significance for the variations across cardiac cycle for both vessel types (all *P*-values for variations > 0.05).

The change of the vessel diameter over the cardiac cycle after visualization, averaged for 12 subjects, has been tabulated in Table 8.3. The results show 3.3 μm change for arterioles and 6.6 μm change for the venules. This is a significant increase from the measurements without visualization (all *P*-values for variations < 0.01).

Table 8.2 Average pulsation of retinal vasculature without visualization at different cardiac cycle points for 12 subjects.

	Cardiac Cycle Point	Mean (SD) (μm)	P-Value†	Variations* (μm)	Max-Min (μm)
Individual Arterioles Caliber	1	90.6 (10.0)	0.699	Ref.	1.2
	2	91.2 (9.8)		0.6	
	3	90.4 (10.3)		0.2	
	4	91.3 (9.4)		0.7	
	5	90.8 (9.1)		0.2	
	6	90.5 (8.7)		0.1	
	7	90.1 (9.7)		0.5	
	8	90.8 (9.9)		0.2	
Individual Venules Caliber	1	111.9 (12.6)	0.211	Ref.	1.9
	2	111.4 (11.7)		0.5	
	3	111.6 (13.1)		0.3	
	4	113.0 (13.2)		1.1	
	5	112.1 (12.9)		0.2	
	6	113.3 (12.5)		1.4	
	7	112.0 (14.3)		0.1	
	8	112.3 (13.6)		0.4	

Table 8.3 Average pulsation of retinal vasculature with visualization at different cardiac cycle points for 12 subjects

	Cardiac Cycle Point	Mean (SD) (μm)	P-Value†	Variations* (μm)	Max-Min† (μm)
Individual Arterioles Caliber	1	99.0 (9.5)	0.001	Ref.	3.3
	2	101.5 (10.0)		2.5	
	3	98.2 (9.6)		0.8	
	4	98.6 (9.7)		0.4	
	5	98.2 (9.8)		0.8	
	6	99.3 (11.1)		0.3	
	7	100.4 (9.7)		1.4	
	8	100.6 (8.4)		1.6	
Individual Venules Caliber	1	109.4 (14.5)	<0.001	Ref.	6.6
	2	108.6 (15.0)		0.8	
	3	113.3 (16.1)		3.9	
	4	114.3 (14.5)		4.9	
	5	113.6 (17.3)		4.2	
	6	115.2 (15.7)		5.8	
	7	110.9 (16.1)		1.5	
	8	112.7 (17.2)		3.3	

Figure 8.7 shows the trend for vessel diameter variation over the cardiac cycle. All the trends for both arterioles and venules followed approximately a similar pattern which was in agreement with the result from previous works (Chen, Patel et al. 1994; Moret, Poloschek et al. 2011).

However, the result from VMRS (after visualization) showed higher variations than the other test especially for the venules. Arteries and vein found to be out of phase with maximum peaks at different cardiac points. Arterioles peaked at $1/8^{th}$ of the R-R interval (point No. 2) but the venules did at its $5/8^{th}$ (point No. 6).

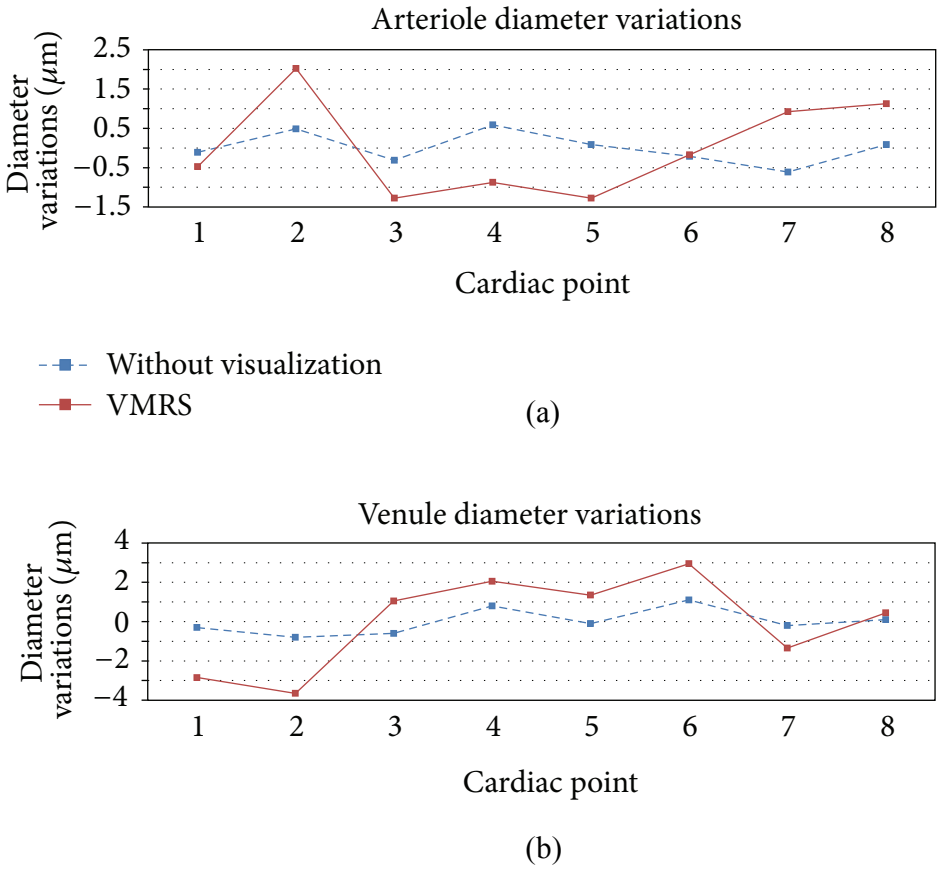

Figure 8.7 Variation of individual vessel diameter at different cardiac points. a) Average arteriole caliber change across one cardiac cycle, and b) Average venule caliber change across one cardiac cycle.

8.9.3 Zone based comparison of FD variations

Tables 8.4 and 8.5 provide the multiple paired t-test analysis and zone based comparison of the FDC (caliber specific FD) and FD_{BC} in terms of statistical significance with respect to each cardiac cycle point, respectively. The first column represent for the cardiac cycle points at which

the images were taken. The rest of the tables are divided into three major columns of Zone A, Zone B and Zone AB denoting the region where the dimensions were measured. The reference factor (point) was set to the mean FD measured in each zone at the first cardiac point. The null hypothesis was defined as H_0: the mean difference between point 1 and the test points (2 to 8) = 0 Vs H_1: the mean difference ≠ 0. According to these table no statistical significant difference was detected between the mean FD of cardiac points in any zone (all *p*-s > α, α=0.05) for both FDC and FD_{BC} except for the FDC of the cardiac point 4 measured in zone B (*p*=0.048, α=0.05).

Table 8.4 Pair wised zone based comparison between Caliber Specific FD (FDC) at different cardiac cycle points (paired t-test)

Cardiac Points	Caliber Specific FD (FDC)					
	Zone A		Zone B		Zone AB	
	Mean (SD)	P* value	Mean (SD)	P* value	Mean (SD)	P* value
1	1.947 (0.008)	Ref	1.961 (0.007)	Ref	1.954 (0.007)	Ref
2	1.947 (0.009)	0.872	1.961 (0.006)	0.867	1.954 (0.007)	0.96
3	1.948 (0.009)	0.722	1.962 (0.007)	0.389	1.955 (0.007)	0.525
4	1.948 (0.010)	0.326	1.963 (0.006)	**0.048**	1.955 (0.008)	0.118
5	1.948 (0.009)	0.626	1.961 (0.006)	0.645	1.955 (0.007)	0.594
6	1.947 (0.009)	0.653	1.961 (0.007)	0.847	1.954 (0.007)	0.913
7	1.948 (0.009)	0.294	1.962 (0.006)	0.208	1.955 (0.007)	0.186
8	1.947 (0.010)	0.882	1.961 (0.006)	0.990	1.954 (0.007)	0.943

* The null hypothesis was set to H_0: mean difference between point 1 and the test point (2 to 9) = 0 Vs H_1: mean difference ≠ 0

Table 8.5 Pair wised zone based comparison of Box-Counting Dimension (FD_{BC}) at different cardiac cycle points (paired t-test)

Cardiac Points	Box-Counting Dimension (FD_{BC})					
	Zone A		Zone B		Zone AB	
	Mean (SD)	P* value	Mean (SD)	P* value	Mean (SD)	P* value
1	1.716 (0.002)	Ref	1.719 (0.053)	Ref	1.811 (0.053)	Ref
2	1.716 (0.002)	0.773	1.719 (0.054)	0.485	1.811 (0.053)	0.395
3	1.716 (0.002)	0.669	1.721 (0.055)	0.275	1.813 (0.054)	0.285
4	1.716 (0.002)	0.876	1.719 (0.054)	0.380	1.810 (0.053)	0.345
5	1.716 (0.002)	0.862	1.719 (0.054)	0.099	1.810 (0.053)	0.113
6	1.715 (0.002)	0.260	1.720 (0.052)	0.506	1.812 (0.052)	0.526
7	1.716 (0.002)	0.513	1.719 (0.054)	0.278	1.810 (0.053)	0.307
8	1.715 (0.002)	0.216	1.719 (0.053)	0.982	1.811 (0.053)	0.904

* The null hypothesis was set to H_0: mean difference between point 1 and the test point (2 to 9) = 0 Vs H_1: mean difference $\neq 0$

Table 8.6 provides the cross-correlation analysis between the zone-based FDC and FD_{BC} variation trends with respect to eight distinct cardiac cycle points. A, B and AB, in this table refer to the zones in which the FDs were measured. AB denotes the measurement was performed on both zones A and B (the whole ROI). The trends for these variations are demonstrated in Figures 8.8 and 8.9 respectively. The test showed that the FDC in all three zones were highly correlated with each other (all $r>0.88$). Relatively high correlations were also detected between the FDC of all zones and FD_{BC} of zone A (all $r>=0.67$). However, the FD_{BC} of zone B was only correlated to the FD_{BC} corresponding to zone AB ($r=0.999$).

Table 8.6 Pearson's correlation coefficients for zone based comparison between FD_{BC} and FDC.

		FD_{BC}			FDC		
	Zones	**A**	**B**	**AB**	**A**	**B**	**AB**
FD_{BC}	**A**	1					
	B	-0.042	1				
	AB	-0.018	0.999	1			
FDC	**A**	0.821	-0.378	-0.366	1		
	B	0.670	-0.074	-0.067	0.885	1	
	AB	0.758	-0.214	-0.204	0.963	0.977	1

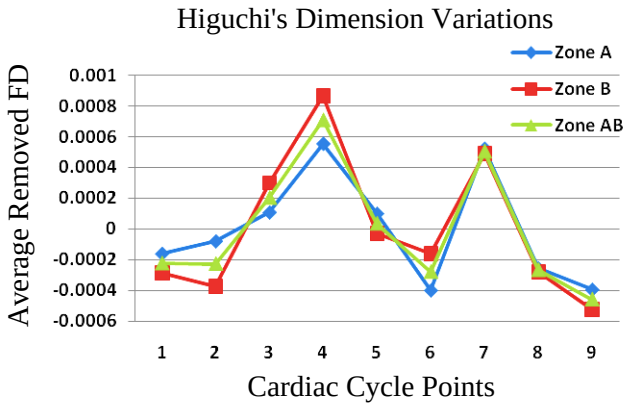

Figure 8.8 Variation of average FDC in different zones with respect to eight distinct cardiac cycle points (Average of each trend is subtracted from the trend for better visualization).

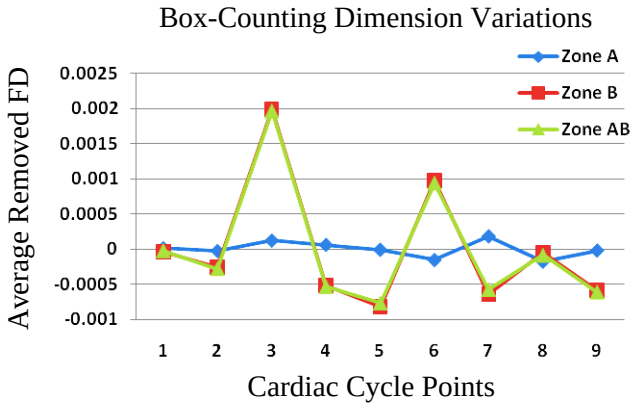

Figure 8.9 Variation of average FD_{BC} in different zones with respect to eight distinct cardiac cycle points (Average of each trend is subtracted from the trend for better visualization).

8.10 Summary

This chapter investigated the variations in vessel diameter and fractal properties of retinal vessel structure caused by pulsation of micro-vasculatures over the cardiac cycle. In the beginning, the novel VMRS technique was introduced and validated for visualization of pulsatile movements of the retinal vasculature using a commercially available standard non-mydriatic fundus camera with slight modification of ECG synchronization. Visualization was required to identify pulsating vessel segments for diameter quantification. A comparative study was performed against the state of the art PCA technique which provided better visualization of the pulsating segments, greater sensitivity and ability to identify more number of pulsatile features in a larger region of interest. Two tests were performed by independent ophthalmologists on arterioles and venules for estimation of diameter variations across cardiac cycle, corresponding to before and after using VMRS. All the trends for both arterioles and venules followed approximately a similar pattern but only when VMRS was used the overall variations were statistically significant and showed higher variations than the other test especially for the venules. Results revealed a phase difference equivalent to half the R-R intervals between arterioles and venules peaks.

Zone based variations of fractal properties were also examined using the state of the art FD_{BC} and the caliber specific FDC based on Higuchi's algorithm. Pair-wise t-test showed no statistical significance (all p-values>0.05) except for the FDC measured in zone B at cardiac point 4 (p=0.048, α=0.05) showing that FDC is sensitive to caliber variations due to cardiac cycle pulsations. Variations of average FDC were found highly correlated in all three zones A, B and AB (all r>0.88) with two peaks at cardiac points 4 and 7. The two peaks with the higher at point 4 and the lower one at point 7 could correspond to the change in volumetric blood flow in systole and diastole phase of cardiac cycle. It was observed that zone A, had the lowest maximum change in FDC compared to reference point 1, followed by Zones AB and B. This also showed that zone B was the most affected zone by the pulsation.

The variations of average FD_{BC} were highly correlated for the two regions B and AB (r=0.99) with the two higher and lower peaks at cardiac points 3 and 6 respectively. The

maximum variations was slightly higher in zone B compared to zone AB. The trend for zone A showed a poor correlation to other zones (all $r<0.05$) using FD_{BC} but relatively high correlation to the FDC trends in all three zones (all $r>=0.67$). The comparison between the trends for the two dimensions showed an overall similar behavior with respect to pulsatile changes but with a one cardiac point shift (delay) in time. In other words, the FDC lagged the FD_{BC} in time by one cardiac cycle pint ($1/8^{th}$ R-R interval). The overall FDC was found to be 1.9 while this value for the box-counting technique was 1.7 which was in agreement with the dimension of normal human retinal circulation previously reported (Masters 2004). The trends for average FD variations were found to be relatively consistent across the entire cardiac points, however, the variations in all three zones (A, B and AB) were not statistically significant with respect to the reference point (1^{st} point) for the both measurements.

Chapter 9

Conclusion

This research has addressed some of the shortcomings regarding the following topics in retinal image analysis and systemic disease assessment.

- Retinal vessel cross-section profile Modeling
- Vessel Diameter measurement
- Diameter change quantification
- Visualization of retinal vessel pulsatile motions and trend analysis
- Localized and region based fractal dimension measurement
- Automatic assessment of retinal images for stroke and mild non-proliferative type 2 diabetes assessment.

This work has demonstrated using currently available retinal vessel diameter quantification techniques can be unreliable due to presence of image artifacts such as background noise, uneven illuminations; poor vessel to background contrast and also vessel center light reflex and therefore may not be suitable for real word clinical application. This work has established a new parametric model for vessel cross-section profile based on sum of a series of second-order and generalized Gaussian functions and has demonstrated that it will provide better fit to the vessel profiles, impaired by image artifacts. The new model provides an excellent fit especially to the vessel boundaries and residual points and unlike other state of the art techniques it can be used for automatic diameter measurement using high resolution images without requiring any profile averaging or smoothing to get better fitting performance. This is evident from the accuracy achieved without the need for manual supervision.

This research has also developed an unsupervised technique based on LDA for pixel classification and vessel edge localization on a cross-section profile. It has been demonstrated that the intersections of LDA class-boundaries with vessel profiles can be used as indicator of vessel edges and therefore diameter measurement. The algorithm has been tested on more than

5000 cross-sections of retinal vessels from the REVIEW dataset through a comparative study with the state-of-the-art techniques. Cross-correlation analyses revealed a high correlation (0.9) with the manual ground truth as the reference diameter.

Although the above works effectively improved the measurement accuracy and reliability, like other techniques, they both relied on edge localization for diameter measurement. This work has associated the source of unreliability and measurement inaccuracy to edge perception as a subjective entity and has hypothesized that any measurement technique which relies on edge localization for diameter quantification would be affected by such image artifacts and is prone to large residual variations. Therefore this work has provided a novel solution based on fractal theory and proposed a feature highly correlated to vessel diameter without requiring vessel edge localization. The 1D fractal properties of vessel cross-section profiles have been analyzed and linked to vessel diameter, which were tested against synthetic images and expert annotated disease and healthy retinal images. The proposed method combines the convenience of diameter measurement as a local feature with Fractal Dimension (FD) as a global measure of complexity and provides a new feature for edge independent diameter quantification and zone based analysis of retinal vasculature. Among state of the art FD methodologies (i.e. 1D box-counting (BC), 2D BC, Differential BC and Higuchi's FD (HFD)), HFD was found to have inverse linear correlation with vessel diameter. The proposed feature was tested on both synthetic (r=-0.985) and natural images (CLRIS, REVIEW dataset, r=-0.91) and was found insensitive to image artifacts.

The clinical application of this feature and the association of specific region of retina with disease condition have also been investigated. A new circular scanning paths as clinical marker for region based FD calculation has been introduced and tested on two datasets of diabetes and 10-year CHD-stroke image sets. The new feature showed significant association with diabetes status (p = 0.006, α=0.05) and stroke (p=0.016, α=0.05). The findings demonstrated a higher value for diabetic cases (Mean ±SD = 1.962 ±0.012) compared to their matching controls (1.954±0.013), however an opposite trend was observed for CHD and stroke event.

This work has investigated the association of gray scale FDs with mild NPDR in patients with type 2 diabetes. The variations in Higuchi's FD with circular scanning around OD and gray scale BC ware found significantly associated with mild NPDR with advantage of Higuchi's being age independent and obtaining the FD in a specific bounding region around the OD.

This research work has also investigated the significance in variation of region based fractal dimension of retinal images due to microvascular pulsatile changes. Therefore a new technique has been developed for visualization and quantification of vessel pulsations and validated on ECG synchronized still fundus images taken at 9 distinct cardiac cycle points. The visualization method was assessed by two experts by observation of cardiac trends in the vessel diameter and other pulsatile features (i.e. Spontaneous Venous Pulsation, serpentine movements, mechanical movements, arteriolar pulsation). The trends for diameter change for both arteriole and venules were statistically significant across the cardiac cycle which was in agreement with similar studies. The zone based analysis of FD variations showed a significant difference between the mean HFD of 1st and 4th cardiac points measured in zone B (p=0.048). No statistical significance was found for other fractal measures (all p-values > 0.05) with respect to any zone and cardiac cycle point. However, although not being significant, the variations observed for box-counting (BC) technique peaked at 3rd and 6th cardiac point. Similar trend was observed for HFD with one point lag and peaks at 4th and 7th points.

9.1 Main contributions of this thesis

The following presents the main contribution of this thesis:

- This thesis has proposed a novel multi-step curve fitting method for retinal vessel profile modeling (Published in the proceedings of IEEE Engineering in Medicine and Biology Society (EMBS) conference, 2011 (Aliahmad, Kumar et al. 2011)) and experimentally validated its application for diameter measurement (Published in the proceedings of Biosignals and Biorobotics Conference (BRC) 2012 (Aliahmad, Kumar et al. 2012))
- This work has also established a new unsupervised automatic technique for vessel profile pixel classification and boundary detection using LDA and validated its application for

vessel diameter measurement on expert annotated healthy and disease images. (Published in the Journal of ISRN ophthalmology, 2012, (Kumar, Aliahmad et al. 2012))

- It has been demonstrated that Higuchi's FD (HFD) of retinal vessel profile is inversely correlated with the diameter and can be used as edge independent feature for quantification of retinal vessel calibre. This association has been validated on both synthetic and natural expert annotated healthy and disease retinal images. The thesis has also demonstrated that this feature can be used in clinical setting for diagnostic purpose. Statistical analyses on both stroke and diabetes datasets have shown that class separation is much better when HDF is used compared to other FDs.
- This research reports a success in application of gray scale fractal measure (Higuchi's and differential BC) for assessment of NPDR in patients with type 2 diabetes (Currently under review by the Investigative Ophthalmology and Visual Science (IOVS) Journal).
- A novel method has also been established for region based visualization of retinal microvasculature pulsation using a set of ECG synchronised still fundus images. The examination of videos in terms of quality and highlighting pulsatile features by two independent ophthalmologists verified the effectiveness of the technique and its visualization clarity extended to zone C (Published in the Journal of ISRN ophthalmology, 2013,(Kumar, Aliahmad et al. 2013)).
- The effect of vessel pulsation on the significance of FD and Diameter variations at several cardiac cycle points has also been investigated. Statistical analysis showed significant variations ($P<0.001$) for individual diameter (Both arteries and veins) and HFD especially for the first and mid cardiac cycle points within an ECG R-R interval however, variations of other FD methods were not significant (all $P > 0.05$) (Published in the proceedings of BRC Conference, 2013, (Aliahmad, Kumar et al. 2013).

9.2 Limitations

There are limitations associated with some of the proposed techniques and studies conducted in this thesis providing rooms for other researchers to address them. These limitations have been listed as follow:

- In chapters 3 and 4 the automation of proposed vessel profile modeling and diameter measurement techniques (including the Multi-step Gaussian method and ULDM) is limited to vessel tracking, edge detection, vessel cross-sectional profile extraction and caliber measurement however, it requires manual ROI and seed point selection by the grader to initiate the tracking process. This can be improved by an intelligent processing algorithm which includes automatic optic disk localization and seed point localization.

- In chapters 6 and 7, the DFD method with circular scanning, provides the convenience of summarizing the entire vascular caliber information into a single number however it includes caliber information independent of vessel types (i.e. arteries-veins). A more comprehensive study on association of caliber variations with risk of disease incidence may require inclusion of vessel type information such as CRVE and CRAE measurements.

- In chapter 8, due to hardware limitation for real-time, high resolution and high sample rate, sequential retinal funduscopy, the study of FD variations across cardiac cycle was limited to 8 distinct cardiac cycle points within an R-R interval which is case for similar studies however, low sampling rate may cause the observed trend lose an extrema or become slightly distorted compared to the real trend. The conclusion of FD and diameter change across cardiac cycle is therefore limited to 8 samples per R-R interval and requires updating with advent of improved funduscopy systems.

9.3 Future studies

While this research has conducted conclusive study regarding association of Higuchi's FD with retinal vessel diameter variation and its ability for being used as a clinical biomarker for stroke and diabetes risk assessment, understanding of its association with other factors including age, gender, blood pressure and their interactions with disease condition is clinically important and requires future investigation and larger datasets. This work suggests the use of newly proposed edge independent caliber measurement technique which can find application in analysis of other biomedical images; where changes in the dimension of an object of interest over a time period is of important. It is also of clinical importance to perform the analyses according to the vessel type (i.e. Arteries and Veins) by classification of the entire vasculature into Arteries and Veins prior to FD measurements. The proposed caliber specific FD has the advantage of summarizing the entire caliber feature into a single value. Therefore, in terms of research application, it might be of interest to include vessel type information into analysis by segmenting the image into arteries and veins and comparing the measurements with vessel summary formulas (CRAVE and CRRVE). However, accurate and automatic vessel classification is still a challenge in retinal image processing which requires further attempts and investigations.

References

Abramoff, M. D., M. K. Garvin, et al. (2010). "Retinal Imaging and Image Analysis." IEEE Trans Med Imaging **3**: 169-208.

Abramoff, M. D., J. M. Reinhardt, et al. (2010). "Automated early detection of diabetic retinopathy." Ophthalmology **117**(6): 1147-1154.

Ahammer, H. (2011). "Higuchi Dimension of Digital Images." PLoS ONE **6**(9): e24796.

Al-Diri, B., A. Hunter, et al. (2009). "An Active Contour Model for Segmenting and Measuring Retinal Vessels." Medical Imaging, IEEE Transactions on **28**(9): 1488-1497.

Al-Diri, B., A. Hunter, et al. (2008). REVIEW - A reference data set for retinal vessel profiles. Engineering in Medicine and Biology Society, 2008. EMBS 2008. 30th Annual International Conference of the IEEE.

Aliahmad, B., D. K. Kumar, et al. (2013). Does fractal properties of retinal vasculature vary with cardiac cycle? Biosignals and Biorobotics Conference (BRC), 2013 ISSNIP.

Aliahmad, B., D. K. Kumar, et al. (2011). "Automatic retinal vessel profiling using multi-step regression method." Conf Proc IEEE Eng Med Biol Soc **2011**: 2606-2609.

Aliahmad, B., D. K. Kumar, et al. (2012). Retinal vessel diameter measurement using multi-step regression method. Biosignals and Biorobotics Conference (BRC), ISSNIP.

Ao, S. I. (2010). Applied Time Series Analysis and Innovative Computing, Springer.

Azemin, M. Z. C., D. K. Kumar, et al. (2011). "Robust Methodology for Fractal Analysis of the Retinal Vasculature." Medical Imaging, IEEE Transactions on **30**(2): 243-250.

Azemin, M. Z. C., D. K. Kumar, et al. (2012). "Age-related rarefaction in the fractal dimension of retinal vessel." Neurobiology of Aging **33**(1): 194.e191-194.e194.

Baker, M. L., P. J. Hand, et al. (2008). "Retinal Signs and Stroke: Revisiting the Link Between the Eye and Brain." Stroke **39**(4): 1371-1379.

Bhuiyan, A., R. Kawasaki, et al. (2010). Vessel Segmentation from Color Retinal Images with Varying Contrast and Central Reflex Properties. Digital Image Computing: Techniques and Applications (DICTA), 2010 International Conference on.

Bhuiyan, A., B. Nath, et al. (2009). Vessel Cross-Sectional Diameter Measurement on Color Retinal Image Biomedical Engineering Systems and Technologies. A. Fred, J. Filipe and H. Gamboa, Springer Berlin Heidelberg. **25:** 214-227.

Brinchmann-Hansen, O. and H. Heier (1986). "Theoretical relations between light streak characteristics and optical properties of retinal vessels." Acta Ophthalmologica **64**(S179): 33-37.

CDC (2005). Centre for disease control, National diabetic fact sheet. USA.

Chandler, C. S., S. Gangaputra, et al. (2011). "Suboptimal Image Focus Broadens Retinal Vessel Caliber Measurement." Investigative Ophthalmology & Visual Science **52**(12): 8558-8561.

Chapman, N., N. Witt, et al. (2001). "Computer algorithms for the automated measurement of retinal arteriolar diameters." British Journal of Ophthalmology **85**(1): 74-79.

Chapman, N., N. Witt, et al. (2001). "Computer algorithms for the automated measurement of retinal arteriolar diameters." British Journal of Ophthalmology **85**(1): 74.

Che Azemin, M. Z., D. K. Kumar, et al. (2012). Loss of Calibre Information During Vessel Segmentation. IEEE International Conference on Biomedical Engineering and Sciences.

Che Azemin, M. Z., D. K. Kumar, et al. (2010). Retinal stroke prediction using logistic-based fusion of multiscale fractal analysis. Imaging Systems and Techniques (IST), 2010 IEEE International Conference on.

Chen, H. C., V. Patel, et al. (1994). "Vessel diameter changes during the cardiac cycle." Eye (Lond) **8 (Pt 1)**: 97-103.

Cheung, C. Y., Y. Zheng, et al. (2011). "Retinal vascular tortuosity, blood pressure, and cardiovascular risk factors." Ophthalmology **118**(5): 812-818.

Cheung, N., K. C. Donaghue, et al. (2009). "Quantitative assessment of early diabetic retinopathy using fractal analysis." Diabetes Care **32**(1): 106-110.

Chrástek, R., M. Wolf, et al. (2005). "Automated segmentation of the optic nerve head for diagnosis of glaucoma." Medical Image Analysis **9**(4): 297-314.

Dabelea, D., R. L. Hanson, et al. (1998). "Increasing prevalence of Type II diabetes in American Indian children." Diabetologia **41**(8): 904-910.

de Mendonca, M. B., C. A. de Amorim Garcia, et al. (2007). "Fractal analysis of retinal vascular tree: segmentation and estimation methods." Arq Bras Oftalmol **70**(3): 413-422.

Doubal, F. N., T. J. MacGillivray, et al. (2010). "Fractal analysis of retinal vessels suggests that a distinct vasculopathy causes lacunar stroke." Neurology **74**(14): 1102-1107.

E. Moghimirad, Seyed Hamid Rezatojighi, et al. (2010). Multi-scale approach for retinal vessel segmentation using medialness function. Proceedings of the 2010 IEEE international conference on Biomedical imaging: from nano to Macro. Rotterdam, Netherlands, IEEE Press**:** 29-32.

Engelgau, M. M., L. S. Geiss, et al. (2004). "The evolving diabetes burden in the United States." Ann Intern Med **140**(11): 945-950.

Family, F., B. R. Masters, et al. (1989). "Fractal pattern formation in human retinal vessels." Physica D: Nonlinear Phenomena **38**(1–3): 98-103.

Gang, L., O. Chutatape, et al. (2002). "Detection and measurement of retinal vessels in fundus images using amplitude modified second-order Gaussian filter." Biomedical Engineering, IEEE Transactions on **49**(2): 168-172.

Gao, X., A. A. Bharath, et al. (1997). Toward retinal vessel parameterization, SPIE.

Gao, X. W., A. Bharath, et al. (2000). "Quantification and characterisation of arteries in retinal images." Computer Methods and Programs in Biomedicine **63**(2): 133-146.

Gao, Y. and Q. P. Wei (2008). "Hypertension related ophthalmocace." International Journal of Ophthalmology **8**(7): 1454-1457.

Garhofer, G., T. Bek, et al. (2010). "Use of the retinal vessel analyzer in ocular blood flow research." Acta Ophthalmologica **88**(7): 717-722.

González, R. C. and R. E. Woods (2008). Digital image processing, Prentice Hall**:** pp 501-510.

Gorelick, P. B. (2002). "New horizons for stroke prevention: PROGRESS and HOPE." The Lancet Neurology **1**(3): 149-156.

Grauslund, J., A. Green, et al. (2010). "Retinal Vascular Fractals and Microvascular and Macrovascular Complications in Type 1 Diabetes." Ophthalmology **117**(7): 1400-1405.

Gregson, P. H., Z. Shen, et al. (1995). "Automated grading of venous beading." Comput Biomed Res **28**(4): 291-304.

Grisan, E., A. Pesce, et al. (2004). A new tracking system for the robust extraction of retinal vessel structure. Engineering in Medicine and Biology Society, 2004. IEMBS '04. 26th Annual International Conference of the IEEE.

Gugleta, K., A. Kochkorov, et al. (2006). "On pulse-wave propagation in the ocular circulation." Invest Ophthalmol Vis Sci **47**(9): 4019-4025.

Hammer, M., S. Leistritz, et al. (2001). "Light paths in retinal vessel oximetry." IEEE Transactions on Biomedical Engineering, **48**(5): 592-598.

Hao, H., M. B. Sasongko, et al. (2012). "Does Retinal Vascular Geometry Vary with Cardiac Cycle?" Investigative Ophthalmology & Visual Science.

Henkind P, Hansen RI, et al. (1979). Ocular circulation. In: Records RE, editor. Physiology of the human eye and visual system. New York, Harper & Row**:** p. 98-155.

Higuchi, T. (1988). "Approach to an irregular time series on the basis of the fractal theory." Physica D: Nonlinear Phenomena **31**(2): 277-283.

Huajun, Y., Z. Ming, et al. (2007). Fractal-based Automatic Localization and Segmentation of Optic Disc in Retinal Images. Engineering in Medicine and Biology Society, 2007. EMBS 2007. 29th Annual International Conference of the IEEE.

Huiqi, L., W. Hsu, et al. (2005). "Automatic grading of retinal vessel caliber." Biomedical Engineering, IEEE Transactions on **52**(7): 1352-1355.

Ikram, M. K., C. Y. Cheung, et al. (2013). "Retinal Vascular Caliber as a Biomarker for Diabetes Microvascular Complications." Diabetes Care **36**(3): 750-759.

Ikram, M. K., F. J. de Jong, et al. (2004). "Are Retinal Arteriolar or Venular Diameters Associated with Markers for Cardiovascular Disorders? The Rotterdam Study." Investigative Ophthalmology & Visual Science **45**(7): 2129-2134.

Jacks, A. S. and N. R. Miller (2003). "Spontaneous retinal venous pulsation: aetiology and significance." J Neurol Neurosurg Psychiatry **74**(1): 7-9.

Jonas, J. B., G. C. Gusek, et al. (1988). "Optic disc, cup and neuroretinal rim size, configuration and correlations in normal eyes." Invest Ophthalmol Vis Sci **29**(7): 1151-1158.

Jürgens, H., D. Saupe, et al. (1992). Fractals for the Classroom: Part One Introduction to Fractals and Chaos, Springer.

Kade Mahesh K and K. N. S (2013). "Review on Fundus Image Acquisition Techniques with Data base Reference to Retinal Abnormalities in Diabetic Retinopathy." International Journal of Computer Applications **68**(8): 17-27.

Kaplan, D. T., M. I. Furman, et al. (1991). "Aging and the complexity of cardiovascular dynamics." Biophysical Journal **59**(4): 945-949.

Kawasaki, R., M. Z. Che Azemin, et al. (2011). "Fractal dimension of the retinal vasculature and risk of stroke: A nested case-control study." Neurology **76**(20): 1766-1767.

Kaye, B. H. (1989). A random walk through fractal dimensions, VCH.

Kempen, J. H., B. J. O'Colmain, et al. (2004). "The prevalence of diabetic retinopathy among adults in the United States." Arch Ophthalmol **122**(4): 552-563.

Kifley, A., J. J. Wang, et al. (2007). "Retinal Vascular Caliber, Diabetes, and Retinopathy." American Journal of Ophthalmology **143**(6): 1024-1026.

Kifley, A., J. J. Wang, et al. (2007). "Retinal vascular caliber, diabetes, and retinopathy." Am J Ophthalmol **143**(6): 1024-1026.

Klein, R., B. E. Klein, et al. (2006). "The relationship of retinopathy in persons without diabetes to the 15-year incidence of diabetes and hypertension: Beaver Dam Eye Study." Trans Am Ophthalmol Soc **104**: 98-107.

Klein, R., B. E. Klein, et al. (2004). "The relation of retinal vessel caliber to the incidence and progression of diabetic retinopathy: XIX: the Wisconsin Epidemiologic Study of Diabetic Retinopathy." Arch Ophthalmol **122**(1): 76-83.

Kolb H, Fernandez E, et al. (1995). "Simple Anatomy of the Retina--Webvision: The Organization of the Retina and Visual System, Salt Lake City (UT): University of Utah Health Sciences Center.

Kresh, J. Y. and I. Izrailtyan (1998). "Evolution in functional complexity of heart rate dynamics: a measure of cardiac allograft adaptability." American Journal of Physiology-Regulatory, Integrative and Comparative Physiology **275**(3): 720.

Kumar, D. K., B. Aliahmad, et al. (2012). "Retinal Vessel Diameter Measurement Using Unsupervised Linear Discriminant Analysis." ISRN Ophthalmology **2012**: 7.

Kumar, D. K., B. Aliahmad, et al. (2013). "A Method for Visualization of Fine Retinal Vascular Pulsation Using Nonmydriatic Fundus Camera Synchronized with Electrocardiogram." ISRN Ophthalmology **2013**: 9.

Kyriazis, M. (2003). "Practical applications of chaos theory to the modulation of human ageing: nature prefers chaos to regularity." Biogerontology **4**(2): 75-90.

Landini, G., G. P. Misson, et al. (1993). "Fractal analysis of the normal human retinal fluorescein angiogram." Curr Eye Res **12**(1): 23-27.

Lascaratos, G., S. Ahmed, et al. (2010). "Pearls & Oy-sters: spontaneous venous pulsation and its role in differentiating papilledema from pseudopapilledema." Neurology **75**(13): e53-54.

Lee, P. P., Z. W. Feldman, et al. (2003). "Longitudinal rates of annual eye examinations of persons with diabetes and chronic eye diseases." Ophthalmology **110**(10): 1952-1959.

Levenberg, K. (1944). "A method for the solution of certain non-linear problems in least squares." Quarterly Journal of Applied Mathmatics **II**(2): 164-168.

Levine, D. N. (1998). "Spontaneous Pulsation of the Retinal Veins." Microvascular Research **56**(3): 154-165.

Li, H., W. Hsu, et al. (2003). A piecewise Gaussian model for profiling and differentiating retinal vessels. Image Processing, 2003. ICIP 2003. Proceedings. 2003 International Conference on.

Liew, G. and J. J. Wang (2011). "Retinal Vascular Signs: A Window to the Heart?" Revista Española de Cardiología (English Version) **64**(06): 515-521.

Liew, G., J. J. Wang, et al. (2008). "Retinal vascular imaging: a new tool in microvascular disease research." Circ Cardiovasc Imaging **1**(2): 156-161.

Lim, L. S., C. Y.-l. Cheung, et al. (2013). "Structural Changes in the Retinal Microvasculature and Renal Function." Investigative Ophthalmology & Visual Science.

Lipsitz, L. A. and A. L. Goldberger (1992). "Loss of complexity and aging: Potential applications of fractals and chaos theory to senescence." JAMA **267**(13): 1806-1809.

Lowell, J., A. Hunter, et al. (2004). "Measurement of retinal vessel widths from fundus images based on 2-D modeling." Medical Imaging, IEEE Transactions on **23**(10): 1196-1204.

Mainster, M. A. (1990). "The fractal properties of retinal vessels: embryological and clinical implications." Eye (Lond) **4 (Pt 1)**: 235-241.

Mandelbrot, B. B. (1983). The Fractal Geometry of Nature, Henry Holt and Company.

Manivannan, A., J. Van der Hoek, et al. (2001). "CLinical investigation of a true color scanning laser ophthalmoscope." Archives of Ophthalmology **119**(6): 819-824.

Martínez-Pérez, M., A. Hughes, et al. (1999). Retinal Blood Vessel Segmentation by Means of Scale-Space Analysis and Region Growing Medical Image Computing and Computer-Assisted Intervention – MICCAI'99. C. Taylor and A. Colchester, Springer Berlin / Heidelberg. **1679:** 90-97.

Masters, B. R. (2004). "Fractal analysis of the vascular tree in the human retina." Annu Rev Biomed Eng **6**: 427-452.

Mayuri Bhargava and T. Y. Wong (2013). "Current Concepts In Hypertensive Retinopathy." Retinal Physician **10**(November 2013): 43 - 54.

McGeechan, K., G. Liew, et al. (2009). "Prediction of Incident Stroke Events Based on Retinal Vessel Caliber: A Systematic Review and Individual-Participant Meta-Analysis." American Journal of Epidemiology **170**(11): 1323-1332.

Mitchell, P., W. Smith, et al. (1995). "Prevalence of agerelated maculopathy in Australia. The Blue Mountains Eye Study." Ophthalmology. **102**: 1450-1460.

Mitchell, P., J. J. Wang, et al. (2005). "Retinal microvascular signs and risk of stroke and stroke mortality." Neurology **65**(7): 1005-1009.

Moret, F., C. M. Poloschek, et al. (2011). "Visualization of fundus vessel pulsation using principal component analysis." Invest Ophthalmol Vis Sci **52**(8): 5457-5464.

Nagaoka, T. and A. Yoshida (2013). "Relationship Between Retinal Fractal Dimensions and Retinal Circulation in Patients with Type 2 Diabetes Mellitus." Current Eye Research **38**(11): 1148-1152.

Nguyen, T. T., J. J. Wang, et al. (2008). "Relationship of Retinal Vascular Caliber With Diabetes and Retinopathy: The Multi-Ethnic Study of Atherosclerosis (MESA)." Diabetes Care **31**(3): 544-549.

Ning Cheung, Kim C. Donaghue, et al. (2009). "Quantitative assessment of early diabetic retinopathy using fractal analysis." Diabetes Care **32**(1): 106.

Nourrit, V., J. Denniss, et al. (2010). "High-resolution hyperspectral imaging of the retina with a modified fundus camera." Journal Français d'Ophtalmologie **33**(10): 686-692.

Ong, Y. T., T. Y. Wong, et al. (2013). "Hypertensive retinopathy and risk of stroke." Hypertension **62**(4): 706-711.

Pakter, H. M., S. C. Fuchs, et al. (2011). "Computer-assisted methods to evaluate retinal vascular caliber: what are they measuring?" Invest Ophthalmol Vis Sci **52**(2): 810-815.

Patton, N., T. Aslam, et al. (2005). "Retinal vascular image analysis as a potential screening tool for cerebrovascular disease: a rationale based on homology between cerebral and retinal microvasculatures." J Anat **206**(4): 319-348.

Pikkujamsa, S. M., T. H. Makikallio, et al. (1999). "Cardiac interbeat interval dynamics from childhood to senescence: comparison of conventional and new measures based on fractals and chaos theory." Circulation **100**(4): 393.

Raghavendra BS and Narayana Dutt D. (2010). "Computing fractal dimension of signals using multiresolution box-counting method." World Acad Sci Eng Technol **6**(1): 1223–1238.

Rosenbloom, A. L., J. R. Joe, et al. (1999). "Emerging epidemic of type 2 diabetes in youth." Diabetes Care **22**(2): 345-354.

Sable, A. H. and K. C. Jondhale (2010). Modified Double Bilateral Filter for Sharpness Enhancement and Noise Removal. Advances in Computer Engineering (ACE), 2010 International Conference on.

Sarkar, N. and B. B. Chaudhuri (1994). "An efficient differential box-counting approach to compute fractal dimension of image." Systems, Man and Cybernetics, IEEE Transactions on **24**(1): 115-120.

Sasongko, M. B., J. J. Wang, et al. (2010). "Alterations in Retinal Microvascular Geometry in Young Type 1 Diabetes." Diabetes Care **33**(6): 1331-1336.

Sasongko, M. B., J. J. Wang, et al. (2010). "Alterations in retinal microvascular geometry in young type 1 diabetes." Diabetes Care **33**(6): 1331-1336.

Schierwagen, A. "Dendritic branching patterns." Chaos in Biological System: 191-193.

Seber, G. A. F. (1984). Discriminant Analysis. Multivariate Observations, John Wiley & Sons, Inc.**:** 279-346.

Shu-Chen, C. and H. Yueh-Min (2003). "A novel approach to diagnose diabetes based on the fractal characteristics of retinal images." Information Technology in Biomedicine, IEEE Transactions on **7**(3): 163-170.

Skinner, J. E. (1994). "Low-dimensional chaos in biological systems." Nature Biotechnology **12**(6): 596-600.

soares, J. V. B. (2008). "HM integration for vessel segmentation ", from http://sourceforge.net/projects/retinal/files/mlvessel/.

Soares, J. V. B., J. J. G. Leandro, et al. (2006). "Retinal vessel segmentation using the 2-D Gabor wavelet and supervised classification." IEEE Transactions on Medical Imaging **25**(9): 1214-1222.

Stewart, C. V., C. L. Tsai, et al. (2003). "The dual-bootstrap iterative closest point algorithm with application to retinal image registration." IEEE Trans Med Imaging **22**(11): 1379-1394.

The University of Iowa. (2006). "Optic disc edema." from http://webeye.ophth.uiowa.edu/dept/coms/grading/optic-disc-edema.htm.

Timothy J. Bennett. (2011). "Fundamentals of Fluorescein Angiography." from http://www.opsweb.org/?page=FA.

Timothy J. Bennett. (2011). "Monochromatic Fundus Photography." from http://www.opsweb.org/?page=Monochromatic.

Tomasi, C. and R. Manduchi (1998). Bilateral filtering for gray and color images. Computer Vision, 1998. Sixth International Conference on.

Toronto, J. W. N. P. N. U. and V. H. P. N. U. W. Ontario (2001). Stroke Prevention, Oxford University Press, USA.

Vilser, W., E. Nagel, et al. (2002). "Retinal Vessel Analysis--new possibilities." Biomed Tech (Berl) **47**: 682-685.

Vlachos, M. and E. Dermatas (2010). "Multi-scale retinal vessel segmentation using line tracking." Computerized Medical Imaging and Graphics **34**(3): 213-227.

Wang, J., P. Mitchell, et al. (2002). "Generalized Retinal Arteriolar Narrowing Predicts 5-year Cardio-vascular and Cerebro-vascular Mortality: Findings from the Blue Mountains Eye Study." Invest. Ophthalmol. Vis. Sci. **43**(12): 4396-.

Wang, J. J., G. Liew, et al. (2007). "Retinal vessel diameter and cardiovascular mortality: pooled data analysis from two older populations." European Heart Journal **28**(16): 1984-1992.

Wang, J. J., P. Mitchell, et al. (2003). "Hypertensive Retinal Vessel Wall Signs in a General Older Population." Hypertension **42**(4): 534-541.

Webb, R. H., G. W. Hughes, et al. (1980). "Flying spot TV ophthalmoscope." Appl Opt **19**(17): 2991-2997.

WebMD (2009). Picture of the eye, WebMD, LLC.

WHO (2003). World Health Organization Screening for Type 2 Diabetes: Report of a World Health Organisation and International Diabetes Federation Meeting.

Wijaya, I. G. P. S., K. Uchimura, et al. (2011). Human face security system using alternative linear discriminant analysis based classifier. Frontiers of Computer Vision (FCV), 2011 17th Korea-Japan Joint Workshop on.

Wong, M.-c., J. W. Y. Chung, et al. (2007). "Effects of treatments for symptoms of painful diabetic neuropathy: systematic review." BMJ **335**(7610): 87.

Wong, T. Y., F. M. A. Islam, et al. (2006). "Retinal Vascular Caliber, Cardiovascular Risk Factors, and Inflammation: The Multi-Ethnic Study of Atherosclerosis (MESA)." Investigative Ophthalmology & Visual Science **47**(6): 2341-2350.

Wong, T. Y., R. Klein, et al. (2004). "Retinal arteriolar diameter and risk for hypertension." Ann Intern Med **140**(4): 248-255.

Wong, T. Y., R. Klein, et al. (2002). "Retinal arteriolar narrowing and risk of coronary heart disease in men and women. The Atherosclerosis Risk in Communities Study." JAMA **287**(9): 1153-1159.

Wong, T. Y., R. Klein, et al. (2002). "Retinal arteriolar narrowing and risk of diabetes mellitus in middle-aged persons." JAMA **287**(19): 2528-2533.

Wong, T. Y., M. D. Knudtson, et al. (2004). "A Prospective Cohort Study of Retinal Arteriolar Narrowing and Mortality." American Journal of Epidemiology **159**(9): 819-825.

Wong, T. Y., Q. Mohamed, et al. (2006). "Do retinopathy signs in non-diabetic individuals predict the subsequent risk of diabetes?" Br J Ophthalmol **90**(3): 301-303.

Wong, T. Y., A. Shankar, et al. (2004). "Retinal Vessel Diameters and the Incidence of Gross Proteinuria and Renal Insufficiency in People With Type 1 Diabetes." Diabetes **53**(1): 179-184.

Xiaofang, Z., D. Wenwen, et al. (2010). A method of retinal vessel width measurement. The 2nd International Conference on Computer and Automation Engineering (ICCAE).

Xiayu, X., M. Niemeijer, et al. (2011). "Vessel Boundary Delineation on Fundus Images Using Graph-Based Approach." Medical Imaging, IEEE Transactions on **30**(6): 1184-1191.

Xu, J., O. Chutatape, et al. (2007). "Automated Optic Disk Boundary Detection by Modified Active Contour Model." Biomedical Engineering, IEEE Transactions on **54**(3): 473-482.

Yang-Williams, K. (2002). "Ophthalmic Photography: Retinal Photography, Angiography, and Electronic Imaging, 2nd ed." Optometry & Vision Science **79**(8): 478.

Yau, J. W., R. Kawasaki, et al. (2010). "Retinal fractal dimension is increased in persons with diabetes but not impaired glucose metabolism: the Australian Diabetes, Obesity and Lifestyle (AusDiab) study." Diabetologia **53**(9): 2042-2045.

Yin Wong, T. (2004). "Is retinal photography useful in the measurement of stroke risk?" The Lancet Neurology **3**(3): 179-183.

Zhou, L., M. S. Rzeszotarski, et al. (1994). "The detection and quantification of retinopathy using digital angiograms." IEEE Trans Med Imaging **13**(4): 619-626.